NASA/CR—2001-210939 ARL–CR–462

Modeling, Modal Properties, and Mesh Stiffness Variation Instabilities of Planetary Gears

Robert G. Parker and Jian Lin
Ohio State University, Columbus, Ohio

DISTRIBUTION STATEMENT A
Approved for Public Release
Distribution Unlimited

20010720 068

May 2001

The NASA STI Program Office . . . in Profile

Since its founding, NASA has been dedicated to the advancement of aeronautics and space science. The NASA Scientific and Technical Information (STI) Program Office plays a key part in helping NASA maintain this important role.

The NASA STI Program Office is operated by Langley Research Center, the Lead Center for NASA's scientific and technical information. The NASA STI Program Office provides access to the NASA STI Database, the largest collection of aeronautical and space science STI in the world. The Program Office is also NASA's institutional mechanism for disseminating the results of its research and development activities. These results are published by NASA in the NASA STI Report Series, which includes the following report types:

- TECHNICAL PUBLICATION. Reports of completed research or a major significant phase of research that present the results of NASA programs and include extensive data or theoretical analysis. Includes compilations of significant scientific and technical data and information deemed to be of continuing reference value. NASA's counterpart of peer-reviewed formal professional papers but has less stringent limitations on manuscript length and extent of graphic presentations.

- TECHNICAL MEMORANDUM. Scientific and technical findings that are preliminary or of specialized interest, e.g., quick release reports, working papers, and bibliographies that contain minimal annotation. Does not contain extensive analysis.

- CONTRACTOR REPORT. Scientific and technical findings by NASA-sponsored contractors and grantees.

- CONFERENCE PUBLICATION. Collected papers from scientific and technical conferences, symposia, seminars, or other meetings sponsored or cosponsored by NASA.

- SPECIAL PUBLICATION. Scientific, technical, or historical information from NASA programs, projects, and missions, often concerned with subjects having substantial public interest.

- TECHNICAL TRANSLATION. English-language translations of foreign scientific and technical material pertinent to NASA's mission.

Specialized services that complement the STI Program Office's diverse offerings include creating custom thesauri, building customized data bases, organizing and publishing research results . . . even providing videos.

For more information about the NASA STI Program Office, see the following:

- Access the NASA STI Program Home Page at ***http://www.sti.nasa.gov***

- E-mail your question via the Internet to help@sti.nasa.gov

- Fax your question to the NASA Access Help Desk at 301–621–0134

- Telephone the NASA Access Help Desk at 301–621–0390

- Write to:
  NASA Access Help Desk
  NASA Center for AeroSpace Information
  7121 Standard Drive
  Hanover, MD 21076

NASA/CR—2001-210939 ARL–CR–462

Modeling, Modal Properties, and Mesh Stiffness Variation Instabilities of Planetary Gears

Robert G. Parker and Jian Lin
Ohio State University, Columbus, Ohio

Prepared under Grant NAG3–1979

National Aeronautics and
Space Administration

Glenn Research Center

May 2001

Acknowledgments

The authors would like to thank Timothy L. Krantz of the Army Research Laboratory at NASA Glenn Research Center for his support and advice on the project.

Available from

NASA Center for Aerospace Information
7121 Standard Drive
Hanover, MD 21076

National Technical Information Service
5285 Port Royal Road
Springfield, VA 22100

Available electronically at http://gltrs.grc.nasa.gov/GLTRS

TABLE OF CONTENTS

1. Introduction 1
1.1 Motivation 1
1.2 Critical Topics 5
1.3 Scope of Investigation 12

2. Planetary Gear Modeling 15
2.1 Modeling Considerations 15
2.2 System Equations 17

3. Natural Frequency and Vibration Mode Properties 19
3.1 Equally Spaced Planets 19
3.2 Arbitrarily Spaced Planets 24
3.3 Modal Strain and Kinetic Energy 25
3.4 Discussion 27

4. Eigensensitivity to Design Parameters 33
4.1 Calculation of Eigensensitivity 34
4.2 Eigensensitivity to Mesh and Support Stiffnesses 37
4.2.1 Tuned System 37
4.2.2 Mistuned System 42
4.3 Eigensensitivity to Gear Mass and Inertia 45
4.4 Eigensensitivity to Operating Speed 47
4.5 Natural Frequency Veering 49
4.5.1 Veering/Crossing Criterion 50
4.5.2 Veering Rules in Planetary Gears 52
4.6 Discussion and Summary 55

5. Parametric Instability from Mesh Stiffness Variation 59
5.1 Two-Stage Gear Systems 60
5.1.1 System Model 60

5.1.2 Conditions of Parametric Instability 64
5.1.3 An Example 76
5.1.4 Discussion 77
5.2 Planetary Gears 79
5.2.1 System Model 82
5.2.2 General Expression for Instability Boundaries 85
5.2.3 Planetary Gear Parametric Instability 88
5.2.4 Tooth Separation Nonlinearity 97

6. Summary and Future Work 101
6.1 Summary and Benefits 101
6.2 Future Work 104

Appendix
A. System Matrices 109
B. Example System 111

Bibliography 113

CHAPTER 1

INTRODUCTION

1.1 Motivation

Planetary gears are widely used in the transmissions of helicopters, automobiles, aircraft engines, heavy machinery and marine vehicles. Figure 1.1 illustrates a single-stage planetary gearset consisting of a sun gear, a ring gear, several planets, and a carrier. Any of the carrier, ring, and sun can be selected as the input or output component, and the power is transmitted through multiple paths of the planet meshes. Planetary gears have substantial advantages over parallel shaft drives, including compactness, large torque-to-weight ratio, diminished loads on shafts bearings, and reduced noise and vibration due to the relatively smaller and stiffer components.

Despite planetary gears' advantages, noise and vibration remain major concerns in their applications. In most helicopters, planetary gears are used in the last stage of gear reduction. This planetary gear is mounted directly to the helicopter cabin, so its vibration is the main source of structure-borne cabin noise, which can exceed 100 dB (Krantz, 1993). Measurement of the cabin noise shows that gear mesh frequency and its harmonics are the dominant acoustic frequencies (Figure 1.2). Extensive cabin noise results in

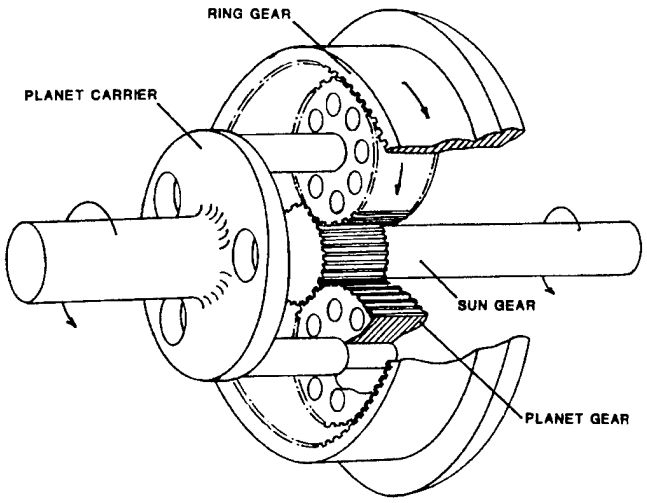

Figure 1.1 Planetary gear diagram (Lynwander, 1983)

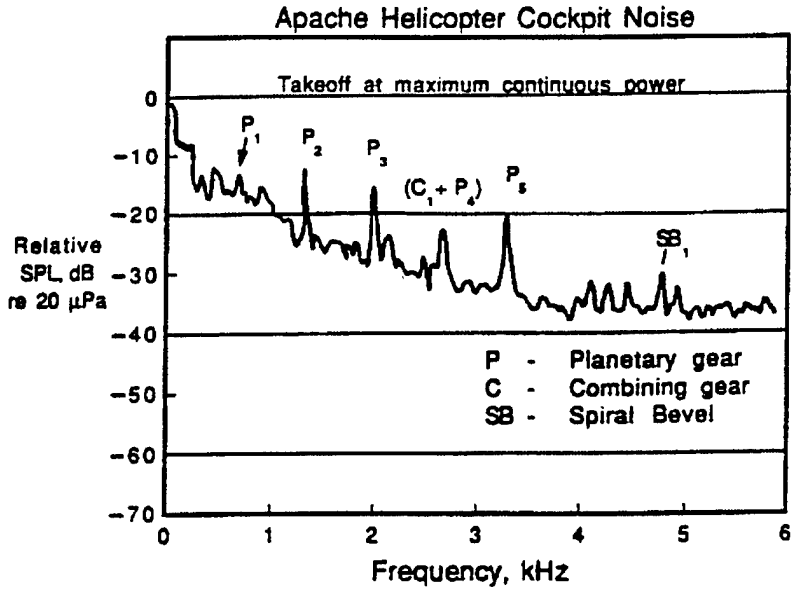

Figure 1.2 Helicopter cabin noise spectra (Heath and Bossler, 1993)

operator fatigue, communication difficulty and health risk from extended exposure. Mitigating the cabin noise becomes a crucial requirement for effective operation of military and civilian helicopters. In vehicle automatic transmissions, planetary gear vibration can be transferred through bearings and mounts to the passenger compartment and results in discrete high frequency pitches in automotive interior noise. Consumers often perceive the gear noise as poor quality and mechanical problems. Vibration reduction in planetary gears provides substantial benefits: reduced noise, improved reliability, more efficient power transfer, and reduced maintenance costs. However, the noise and vibration issues in current planetary gear design rely mostly on empirical experience and cut-and-try methods, rather than engineering understanding. General design guidelines are needed to minimize planetary gear vibration.

Vibration reduction of planetary gears requires thorough examination of the structural dynamics. A detailed review of planetary gear dynamic analyses before 1980s is found in August (1983). These analyses on planetary gear dynamics include modeling and free vibration investigations (Cunliffe et al., 1974; Botman, 1976; Frater et al., 1983; Velex and Flamand, 1996), neutralization of transmission error excitation (Seager, 1975), dynamic tooth load due to run-out errors (Hidaka, 1979e; 1980), mesh stiffness variation (Kasuba and August, 1984), load sharing among planets (Ma and Botman, 1984), and torsional vibration and dynamic loads (August and Kasuba, 1986). More analytical studies were performed after 1990s. Kahraman derived a nonlinear, time-varying planar model (1994a) and subsequently extended it to three-dimensions and examined the influence of planet phasing on dynamic response (1994b). Using a three-dimensional

model for helical gears, Kahraman and Blankenship (1994) investigated the load sharing and mesh phasing among planets. Kahraman (1994c) also reduced his model to a purely torsional one to predict natural frequencies and vibration modes. More recently, Agashe (1998) and Parker et al. (2000a) used a finite element tool to investigate the dynamic response and planet phasing issues in planetary gears. This special computational tool naturally includes the time-varying mesh stiffness and transmission error without *ad hoc* specification of these factors. Parker (2000) also rigorously proved the effectiveness of using planet phasing schemes to suppress planetary gear vibration.

The experimental studies on practical planetary gear vibrations are scarce due to the difficult access to the internal gears. Chiang and Badgley (1973) investigated the noise spectra generated from ring gear vibrations in the planetary reduction gearbox of two helicopters (Boeing-Vertol CH-47 and Bell UH-1D). Toda and Botman (1979) experimentally showed that planetary gear vibration resulting from spacing errors can be minimized by proper indexing of the planets. Botman (1980) presented some typical measurement results on the planetary gear of a PT6 aircraft engine. His experiments showed some peculiar behavior of planetary gear vibration regarding load sharing, response due to gear errors, and dynamic instability. Hidaka and his colleagues experimentally studied the dynamic behavior of a Stoeckicht planetary gear and published a series of reports (Hidaka et al, 1976a,b; 1977; 1979a~d). Their reports studied some important issues such as load distribution, effect of different meshing-phase among sun/ring-planet meshes, *etc.* Velex et al. (1994) matched the natural frequency measurement of a Stoeckicht epicyclic train with their finite element calculations. Rakhit

(1997) measured the subsynchronous vibrations at the turbine bearings in a gas turbogenerator and proposed a design of the epicyclic gearbox to reduce the vibration. Kahraman (1999) developed a generalized model to predict load sharing of planets under quasi-static conditions and validated the model with experiments.

According to a comprehensive literature research, less analytical investigations have been done on planetary gear dynamics than those for parallel shaft gears. This is largely due to the modeling complexity of planetary gears. Important complications include multiple mesh contacts, detailed kinematics, mesh stiffness variation, transmission error excitation, contact loss nonlinearity, elastic ring gear vibration and geometric imperfections. Most previous research uses numerical or experimental methods to examine specific planetary gear systems. Some critical issues remain unsolved and require systematic analytical study.

1.2 Critical Topics

The fundamental task of analytical planetary gear research is to build a dynamic model. For different analysis purposes, there are several modeling choices such as a simple dynamic factor model, compliance tooth model, torsional model, and geared rotor dynamic model (Ozguven and Houser, 1988). According to the source-path-receiver relationship between the planetary gear, bearing/mounting, and the cabin, different boundaries can be selected for building the model. This study focuses on the understanding of planetary gear dynamic behavior, so a single stage gearset with discrete

elements is the basic model for investigation. In previous lumped-parameter models (Cunliffe et al., 1974; Botman 1976; Kahraman, 1994a, b, c), the gyroscopic effects caused by carrier rotation have not been considered. Because planetary gears have planets mounted on the rotating carrier, the Coriolis and centripetal accelerations caused by the carrier rotation introduce gyroscopic terms into the system model. For high-speed applications such as aircraft engines (30,000 rpm), gyroscopic effects may heavily impact the system stability and behavior. This project will develop a planetary gear model including the gyroscopic effects, contact loss nonlinearity, mesh stiffness variation, and static transmission error excitation. Despite the use of the term planetary gear, this model is applicable for epicyclic gears with any configuration (fixed/floating sun, ring, and carrier, and non-equally spaced planets). The model is the fundamental tool for the analytical research.

The free vibration analysis calculates critical parameters such as natural frequencies and vibration modes that are essential for almost all dynamic investigations. Cunliffe et al. (1974) numerically identified the planetary gear natural frequencies and vibration modes for a specific thirteen degree-of-freedom system. Similar work has been done by Botman (1976), Frater et al. (1983), and Kahraman (1994c) for other example planetary gears, but no systematic characterization has been obtained. This project reveals the unique structure of natural frequency spectra and vibration modes due to the cyclic symmetry of planetary gears (Lin and Parker, 1999a). All the vibration modes are classified into rotational, translational and planet modes with distinctive properties. The structured vibration modes are rigorously characterized for general epicyclic gears and

validated by the computational results from a finite element model. These well-defined properties are not valid when planets are arbitrarily spaced, but still apply to practically important case of diametrically opposed planets (Lin and Parker, 2000a). The free vibration properties are very useful for further analyses of planetary gear dynamics, including eigensensitivity to design parameters, natural frequency veering, planet mesh phasing, and parametric instabilities from mesh stiffness variations.

Another key issue is how design parameters affect the natural frequencies and vibration modes. During the design process, model parameters are often altered to evaluate alternative design choices, reduce weight, and tune the system frequencies to avoid resonance. The influence of design parameters on planetary gear natural frequencies was touched on in a few papers, but general conclusions were not presented. In the plots of natural frequencies versus design parameters, veering phenomena (Leissa, 1974; Perkins and Mote, 1986) often occur and obstruct the tracing of eigenvalue loci under parameter changes. In the veering neighborhood, where two eigenvalue loci approach each other and then abruptly veer away, the veering vibration modes are strongly coupled and change dramatically (Figure 1.3). It is necessary to systematically study natural frequency and vibration mode sensitivities and their veering characters to identify the parameters critical to planetary gear vibration. In addition, practical planetary gears may be mistuned by mesh stiffness variation, manufacturing imperfections and assembling errors. For some symmetric structures, such as turbine blades, space antennae, and multi-span beams, small disorders may dramatically change the vibration

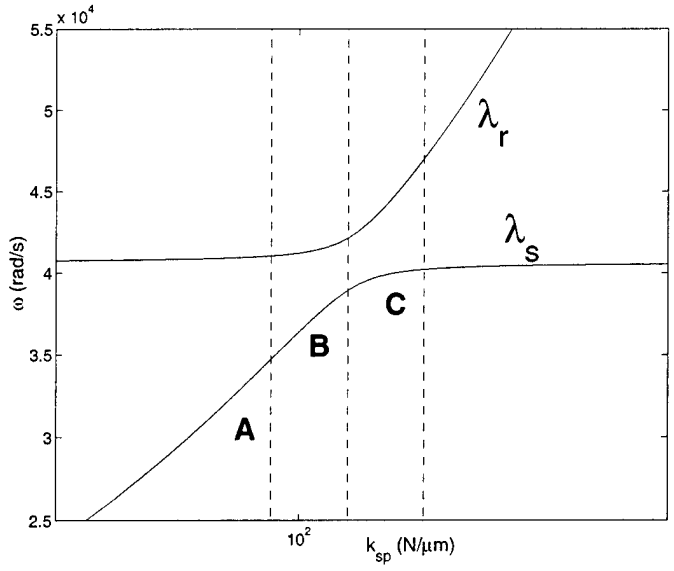

(a)

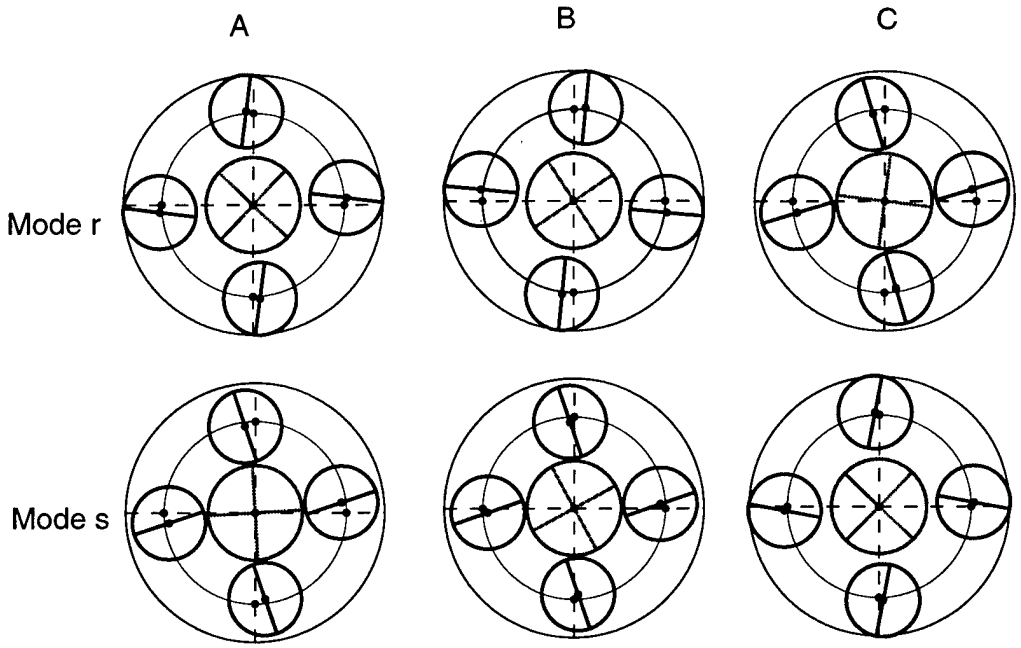

(b)

Figure 1.3 (a) Two eigenvalue loci veer. (b) The associated vibration modes change dramatically through points A, B, and C. The two modes are strongly coupled at point B.

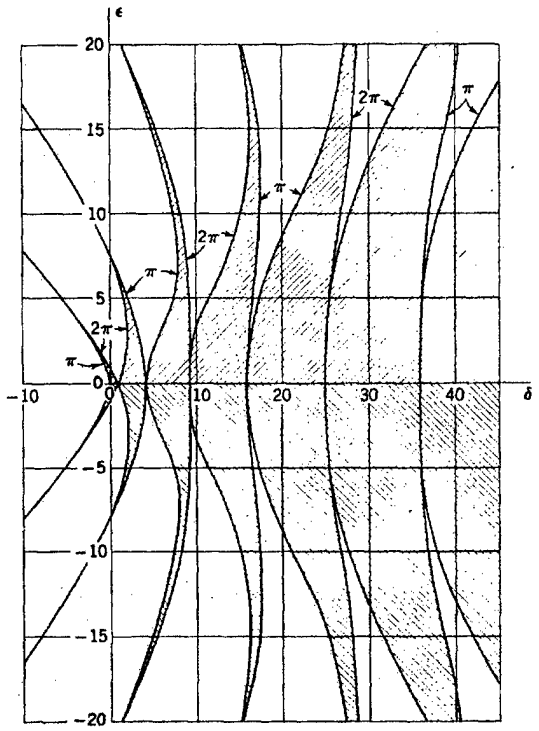

Figure 1.4 Stability chart of Mathieu equation $\ddot{x} + (\delta - 2\varepsilon \cos 2t)x = 0$ (Meirovitch, 1970). The hatched areas are instability regions.

modes and result in mode localization (Pierre, 1988; Cornwell and Bendiksen, 1992; Happawana et al., 1998). Vibration modes with dominant motion localized in one planet lead to load sharing unbalance, which can severely undermine the power transfer efficiency and damage the gear teeth and bearings. This work presents a thorough eigensensitivity analysis of the natural frequencies and vibration modes to key model parameters for both tuned (cyclically symmetric) and mistuned planetary gears. The parameters considered include mesh/support stiffnesses, component masses, moments of inertia, and operating speed. Taking advantage of the structured vibration mode

properties, natural frequency sensitivities are expressed in simple, closed-form formulae which relate the sensitivities to modal strain and kinetic energy (Lin and Parker, 1999b). Well-defined veering rules are derived from these formulae and vibration mode properties to predict veering and its strength. The influence of design parameters is examined through a benchmark example. The knowledge of natural frequency spectra, vibration mode properties, eigensensitivity formulae, and special veering rules are combined to provide considerable insight into planetary gear free vibration.

It is well known that mesh stiffness variation is a major excitation source of gear vibration. For spur gears, the time-varying stiffness is caused by the alternating number of teeth in contact. It is a periodic function at mesh frequency, which is the number of tooth mesh cycles per second. The mesh stiffness variation serves as a parametric excitation and results in instability under certain conditions. Parametric instabilities are particularly dangerous because they can occur at excitation frequencies well below the system natural frequencies. The mesh stiffness variation can be further complicated by the interaction of transmission error excitation (Smith, 1983) and contact loss nonlinearity (Blankenship and Kahraman, 1995; Kahraman and Blankenship, 1996, 1997). Literature reviews of parametrically excited systems can be found in the work of Ibrahim and Barr (1978). For a single pair of gears excited by harmonically varying stiffness, Bollinger and Harker (1967) used the one degree-of-freedom Mathieu equation to determine the instability regions. The instability conditions are often illustrated in the plots of the exciting frequency versus the amplitude of varying stiffness, as shown in Figure 1.4. Benton and Seireg (1978, 1980a) obtained the response to mesh stiffness

variation and external excitations at integer multiples of the rotation speed. They experimentally verify the resonance region obtained from simulation and demonstrated the damage of parametric instability on gear teeth. Amabili and Rivola (1997) studied the steady state response and stability of the single degree of freedom system with time-varying stiffness and damping. Other researchers (Benton and Seireg, 1981; Kahraman and Blankenship, 1996; Nataraj and Whitman, 1997; Nataraj and Arakere, 1999) also investigated gear parametric instabilities using single degree-of-freedom models. For multi-mesh gear systems, it is surprising to find little investigation on parametric instability in the published literature. Although Benton and Seireg (1980b, 1981) studied a gear system with two meshes, they uncoupled the model into two single degree-of-freedom equations with some simplifications. Their conclusions on the mesh stiffness phasing effect contradict another investigation (Tordion and Gauvin, 1977) using an infinite determinant analysis (Bolotin, 1964). This conflict will be clarified using perturbation analysis (Hsu, 1963, 1965; Nayfeh and Mook, 1979) and numerical integration methods. In addition, this work extends parametric analysis in two-stage gear systems to planetary gears where parametric excitations are more complicated as different contact ratios and phasing conditions exist between the sun-planet and ring-planet meshes. August and Kasuba (1986) and Velex and Flamand (1996) numerically computed dynamic responses to mesh stiffness variations for planetary gears with three sequential phased planets. Their results showed the dramatic impacts of mesh stiffness variation on dynamic response, tooth loading, and load sharing among planets. The operating conditions leading to planetary gear parametric instability have not been

analytically investigated. The well-defined vibration mode properties will be used to derive the operating conditions leading to planetary gear instability. The boundaries are expressed in simple forms and the effects of contact ratios and mesh phasing are analytically investigated. In practical design, planet mesh-phasing schemes are often applied to cancel or neutralize the excitations from transmission errors (Seager, 1975; Kahraman, 1994a; Kahraman and Blankenship, 1994; Parker, 2000). This study shows that particular instabilities are eliminated under certain phasing conditions, which can be achieved by selection of design parameters according to the analytical results. Dynamic response and tooth separations induced by parametric instability are numerically examined.

1.3 Scope of Investigation

The scope of this project is to advance the modeling and understanding of planetary gear dynamics and analytically examine certain critical factors affecting planetary gear noise and vibration. This research focuses on the analytical investigation of the following specific tasks.

- Derive a lumped-parameter model for spur planetary gears, including different planet phasing, gyroscopic effects, mesh stiffness variation, and transmission error excitation. The model is valid for general epicyclic gears with any number of planets and will be the fundamental tool for further research.

- Analytically characterize the unique structure of the natural frequency spectra and vibration modes of general planetary gears. The cases with equally and arbitrarily spaced planets (including diametrically opposed planets) are considered.
- Use the vibration mode properties to obtain simple, closed-form formulae for the eigensensitivities to important design parameters. According to these formulae and characterized natural frequency veering rules, the effects of design parameter changes on planetary gear free vibration are investigated.
- Investigate the parametric instabilities caused by multiple time-varying mesh stiffnesses. Two-stage gear systems are examined first to clarify pervious conflicts and derive simple expressions of instability boundaries. Then, the analytical method is extended to planetary gear systems. The well-defined modal properties are used to identify the effects of contact ratios and mesh phasing on planetary gear parametric instability.

CHAPTER 2

PLANETARY GEAR MODELING

2.1 Modeling Considerations

Lumped-parameter modeling is used in this project for dynamic analysis. All gears are considered as rigid bodies and component supports are modeled by springs. A single-mesh model is shown in Figure 2.1 for a pair of spur gears. All bearings/supports are modeled as two perpendicular springs. The gear tooth meshes are represented by springs acting on the line of action with parallel viscous dampers. The transmission error $e(t)$, a prescribed displacement input, is included as indicated. The tooth separation nonlinearity acts as a step function $h(t)$ where $h=1$ when the teeth are in contact and $h=0$ when the teeth lose contact. This model can be extended to planetary gears with multiple meshes.

In planetary gear modeling, the following factors must be considered.

1. *Assumptions.* The analysis deals with planar vibration of single stage planetary gears. Helical gears require three-dimensional modeling and are not considered here. Excellent lubrication is assumed and tooth friction forces are neglected. No damping is included, although a viscous damper could easily be added in parallel with the mesh and bearing springs.

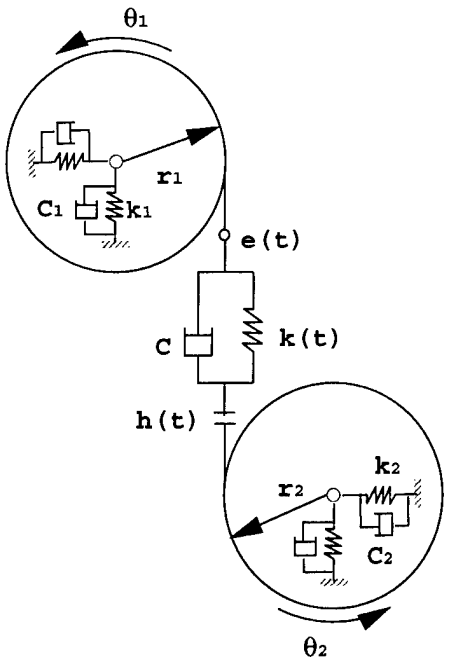

Figure 2.1 A single mesh model

2. *Versatile configurations*. There are many configurations for general epicyclic gears. By fixing one or more of the coaxial components (carrier, ring, and sun), various configurations such as planetary, star, and differential gears can be obtained. In typical designs, one of the coaxial members is free to translate to enhance the load sharing among planets. The number of planets and their positions also vary in practical applications. The proposed model should accommodate these configurations and be flexible for general applications.
3. *System coordinates*. Several choices of coordinates may be used in the modeling. The frame can be fixed or rotating; the planet coordinates can be parallel to each other or use local radial and tangential directions. The coordinate selection does not change the physical properties of the system, but may greatly affect the analysis difficulty.

2.2 System Equations

The planetary gear model used in our analysis is shown in Figure 2.2. Each component has three degrees of freedom: two translations and one rotation. The model is similar to that used by Kahraman (1994a) with two distinctions: (1) the planet deflections are described by radial and tangential coordinates, and (2) gyroscopic effects induced by carrier rotation are modeled. The radial and tangential coordinates more naturally describe the vibration modes. Gyroscopic effects in high-speed applications such as aircraft engines may dramatically alter the dynamic behavior from that at lower speeds. The coordinates illustrated in Figure 2.2 are used. The carrier, ring and sun translations x_h, y_h, $h=c,r,s$ and planet translations $\zeta_n, \eta_n, n = 1,\cdots N$ are measured with respect to a rotating frame of **r** reference **i, j, k** fixed to the carrier with origin **o**. The x_h, $h=c,r,s$ are directed towards the equilibrium position of planet 1, and ζ_n, η_n are the radial and tangential deflections of the n-th planet. The basis **i, j, k** rotates with the constant carrier angular speed Ω_c. The rotational coordinates are $u_h = r_h\theta_h, h = c,r,s,1,\cdots N$, where θ_h is the component rotation; r_h is the base circle radius for the sun, ring and planet, and the radius of the circle passing through the planet centers for the carrier. Circumferential planet locations are specified by the fixed angles ψ_n, where ψ_n is measured relative to the rotating basis vector **i** so that $\psi_1 = 0$. The details of the model derivative are given in Lin and Parker (1999a). The equations of motion are

$$\mathbf{M}\ddot{\mathbf{q}} + \Omega_c\mathbf{G}\dot{\mathbf{q}} + [\mathbf{K}_b + \mathbf{K}_m - \Omega_c^2\mathbf{K}_\Omega]\mathbf{q} = \mathbf{T}(t) + \mathbf{F}(t) \tag{2.1}$$

$$\mathbf{q} = (\underbrace{x_c, y_c, u_c}_{carrier}, \underbrace{x_r, y_r, u_r}_{ring}, \underbrace{x_s, y_s, u_s}_{sun}, \underbrace{\zeta_1, \eta_1, u_1}_{planet\ 1}, \cdots, \underbrace{\zeta_N, \eta_N, u_N}_{planet\ N})$$

where the matrix components are given in the Appendix A. **M** is the inertia matrix and $\mathbf{K}_b$ is the bearing stiffness matrix. **G** and $\mathbf{K}_\Omega$ result from high-speed carrier rotation and have not been included in published models. To model the time-varying stiffness associated with changing numbers of teeth in contact at each mesh, $\mathbf{K}_m$ can be decomposed into mean and time-varying components. Tooth separation nonlinearity is implicitly included in $\mathbf{K}_m(t)$. $\mathbf{T}(t)$ is the applied external torque and $\mathbf{F}(t)$ represents the static transmission error excitation.

This comprehensive model is the fundamental tool for further research of planetary gear dynamics. It is readily applicable for specific configurations of epicyclic gears. Assigning a large value to a transverse or torsional stiffness restrains the translation or rotation of a component; assigning a very compliant stiffness in a component support floats the component.

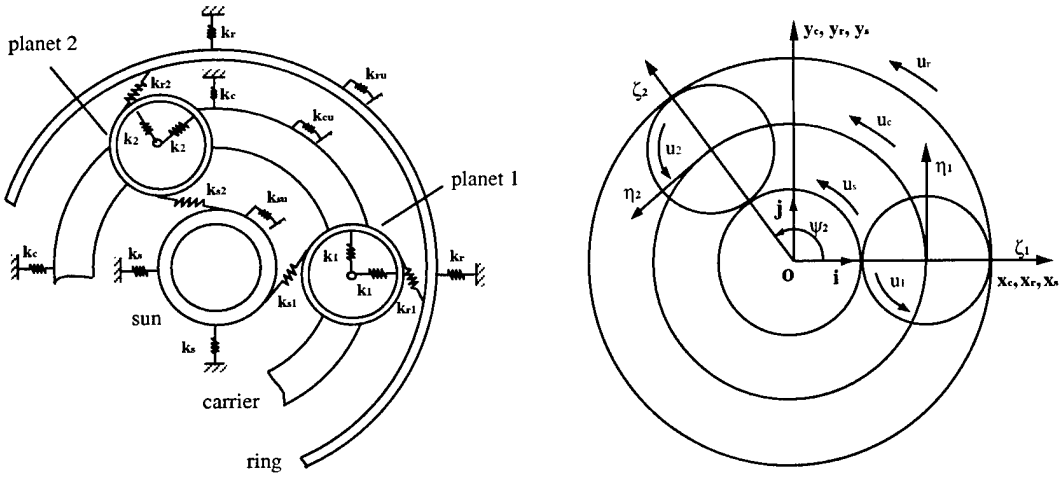

Figure 2.2 Planetary gear model

CHAPTER 3

NATURAL FREQUENCY AND VIBRATION MODE PROPERTIES

This chapter analytically investigates the natural frequency spectra and vibration modes of general planetary gears. The cyclic symmetry of planetary gears leads to highly-structured free vibration characteristics that are identified herein. Unique properties of the eigensolutions for the linear time-invariant case are presented for an example system. The identified properties are then mathematically shown to be characteristics of general planetary gears.

3.1 Equally Spaced Planets

The free vibration of the linear, time-invariant representation is

$$\mathbf{M}\ddot{\mathbf{q}} + \Omega_c \mathbf{G}\dot{\mathbf{q}} + (\mathbf{K} - \Omega_c^2 \mathbf{K}_\Omega)\mathbf{q} = \mathbf{0} \tag{3.1}$$

where $\mathbf{K}=\mathbf{K}_b+\mathbf{K}_m$. The carrier speed is assumed to be small and the gyroscopic terms $\mathbf{G}$ and $\mathbf{K}_\Omega$ are neglected. The associated eigenvalue problem of (3.1) is

$$\omega_i^2 \mathbf{M}\phi_i = \mathbf{K}\phi_i \tag{3.2}$$

where ω_i are natural frequencies and $\phi_i = [\mathbf{p}_c, \mathbf{p}_r, \mathbf{p}_s, \mathbf{p}_1, \cdots \mathbf{p}_N]^T$ are vibration modes with $\mathbf{p}_h = [x_h, y_h, u_h]^T, h = c, r, s$ for the carrier, ring and sun, and $\mathbf{p}_n = [\zeta_n, \eta_n, u_n]^T$ for the planets. At this stage, the planets are assumed identical and equally spaced; all planet

bearing stiffnesses are equal $k_{pn}=k_p$, all sun-planet mesh stiffnesses are equal ($k_{sn}=k_{sp}$); and all ring-planet mesh stiffnesses are equal $k_{rn}=k_{rp}$. With these specifications, planetary gears are cyclically symmetric structures that can be divided into N identical sectors. The cyclic symmetry of planetary gears leads to distinctive natural frequency and vibration mode properties that will be demonstrated analytically.

We first illustrate the eigensolution properties through a numerical example with the parameters in Appendix B case I. Typical vibration modes for $N=4$ are shown in Figure 3.1, where the movements of the carrier and ring are not shown in order to clarify the figures. Some interesting conclusions are obtained from Figure 3.1:

1. Six natural frequencies always have multiplicity $m=1$ for different N. Except for the zero natural frequency, their values increase as additional planets are introduced. Their associated vibration modes have pure rotation of the carrier, ring and sun (Figure 3.1a), so these modes are named *rotational modes*.
2. Six natural frequencies always have multiplicity $m=2$ for various N. Some natural frequencies increase monotonically while others decrease monotonically as N increases. The carrier, ring and sun have pure translation in the corresponding vibration modes (Figure 3.1b), so these modes are defined as *translational modes*.
3. Three natural frequencies have multiplicity $m=N-3$ and exist only if $N>3$. Their associated vibration modes are termed *planet modes* because the carrier, ring and sun do not move; only planet motion occurs in these modes (Figure 3.1c, d, e). For each of these three natural frequencies, the corresponding vibration modes span an $N-3$ dimensional eigenspace.

This example shows there are at most fifteen different natural frequencies for $N \geq 3$; additional planets only change the multiplicity of the planet mode natural frequencies. When $N<3$, all natural frequencies are distinct and the vibration modes do not have special structure because of the loss of cyclic symmetry. In nearly all planetary gear designs, three or more planets are used to take advantage of the load sharing among planets and subsequent discussion is restricted to this case. The eigensolution properties identified in the example are analytically shown to be true for general planetary gears (Lin and Parker, 1999a) and summarized below.

Planet Mode. A planet mode has the form

$$\phi_i = [\mathbf{0},\mathbf{0},\mathbf{0}, w_1\mathbf{p}_1, \cdots w_N\mathbf{p}_1]^T \tag{3.3}$$

where w_n are scalars ($w_1=1$) satisfying

$$\sum w_n \sin\psi_n = 0 \qquad \sum w_n \cos\psi_n = 0 \qquad \sum w_n = 0 \tag{3.4}$$

Planet modes have the following characteristics:

(i) The associated natural frequency has multiplicity $N-3$,

(ii) The translation and rotation of the carrier, ring and sun are zero.

(iii) The planet deflections are scalar multiples of the first (or any other arbitrary) planet's deflection components.

Rotational Mode. A rotational mode has the form

$$\phi_i = [\mathbf{p}_c, \mathbf{p}_r, \mathbf{p}_s, \mathbf{p}_1, \cdots, \mathbf{p}_1]^T \tag{3.5}$$

Rotational modes have the following characteristics:

(i) The associated natural frequency is distinct,

(ii) The translation of the carrier, ring and sun are zero, *i.e.*, $\mathbf{p}_h = [0,0,u_h]^T$, where $j=c,r,s,$

(iii) All planets have identical deflections, *i.e.*, $\mathbf{p}_1 = \mathbf{p}_2 = \cdots = \mathbf{p}_N = [\zeta_1, \eta_1, u_1]^T$.

Translational Mode. A pair of translational modes has the form

$$\phi_i = \begin{bmatrix} \mathbf{p}_c \\ \mathbf{p}_r \\ \mathbf{p}_s \\ (\cos\psi_1 \mathbf{p}_1 + \sin\psi_1 \overline{\mathbf{p}}_1) \\ \vdots \\ (\cos\psi_N \mathbf{p}_1 + \sin\psi_N \overline{\mathbf{p}}_1) \end{bmatrix} \qquad \overline{\phi}_i = \begin{bmatrix} \overline{\mathbf{p}}_c \\ \overline{\mathbf{p}}_r \\ \overline{\mathbf{p}}_s \\ (-\sin\psi_1 \mathbf{p}_1 + \cos\psi_1 \overline{\mathbf{p}}_1) \\ \vdots \\ (-\sin\psi_N \mathbf{p}_1 + \cos\psi_N \overline{\mathbf{p}}_1) \end{bmatrix} \tag{3.6}$$

Translational modes have the following characteristics:

(i) The associated natural frequency has multiplicity two.

(ii) The rotation of the carrier, ring and sun are zero. Furthermore, the carrier, ring, and sun translations in the degenerate modes ϕ_i and $\overline{\phi}_i$ are related by $\mathbf{p}_h = [x_h, y_h, 0]^T$ and $\overline{\mathbf{p}}_h = [-y_h, x_h, 0]^T$, $h=c,r,s,$

(iii) The planet deflections for a pair of vibration modes are related by

$$\begin{bmatrix} \mathbf{p}_n \\ \overline{\mathbf{p}}_n \end{bmatrix} = \begin{bmatrix} \cos\psi_n \mathbf{I} & \sin\psi_n \mathbf{I} \\ -\sin\psi_n \mathbf{I} & \cos\psi_n \mathbf{I} \end{bmatrix} \begin{bmatrix} \mathbf{p}_1 \\ \overline{\mathbf{p}}_1 \end{bmatrix} \tag{3.7}$$

where $\mathbf{p}_n$ and $\overline{\mathbf{p}}_n = [\overline{\zeta}_n, \overline{\eta}_n, \overline{u}_n]^T$ are the deflections of the n-th planet in ϕ_i and $\overline{\phi}_i$. $\mathbf{I}$ is a 3×3 identity matrix and $\psi_n = 2\pi(n-1)/N$.

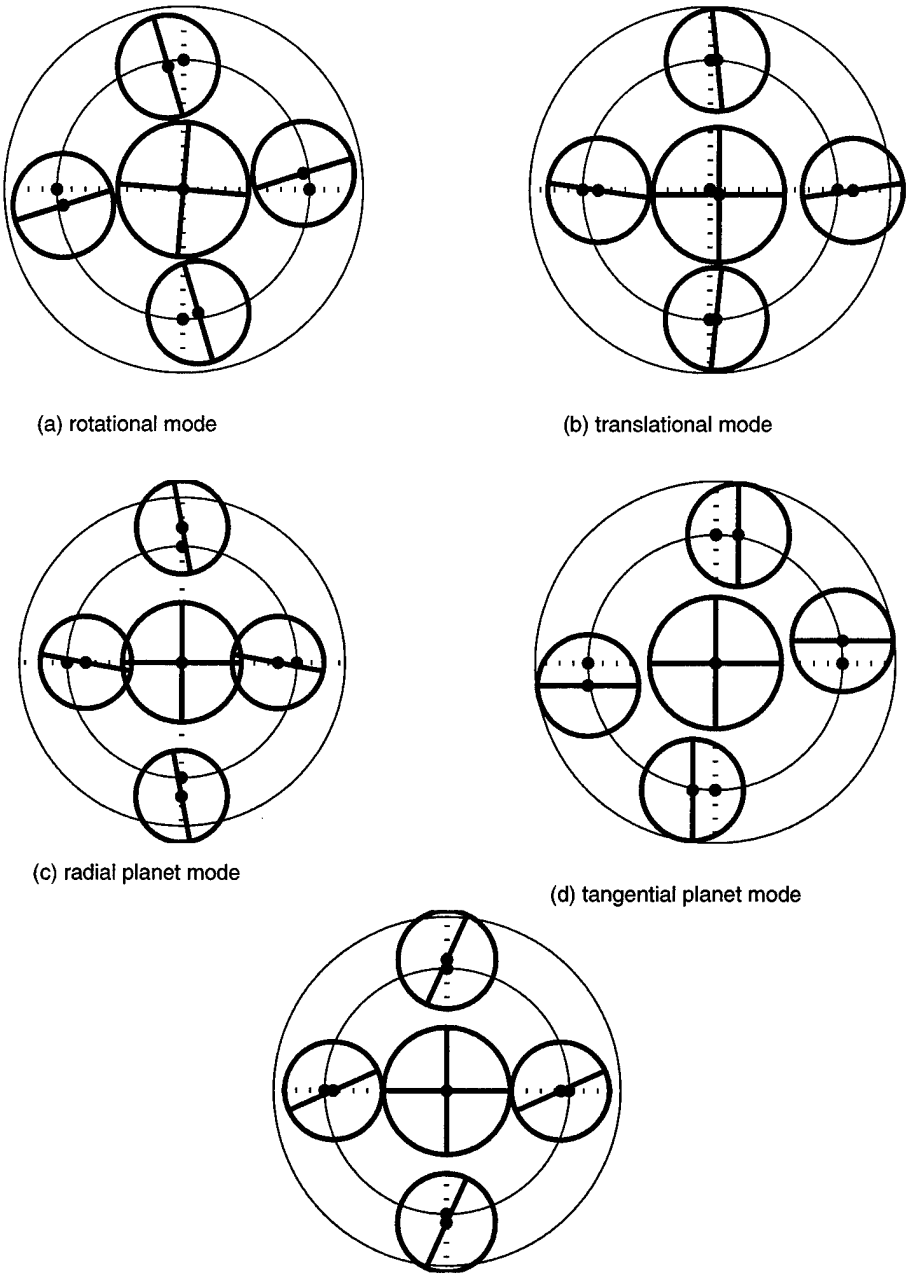

Figure 3.1 Typical vibration modes. Dashed lines are the equilibrium positions and solid lines are the deflected positions. Dots represent the component centers.

3.2 Arbitrarily Spaced Planets

In general, much of the above well-defined structure of the natural frequency spectra and vibration modes is lost when the planets are arbitrarily spaced. A notable exception is the planet modes. Additionally, for the practically important case of diametrically opposed planets, the free vibration retains its unique properties.

Planet Mode: As for planetary gears with equally spaced planets, systems with arbitrary planet spacing always have three sets of planet modes of the form (3.3) with multiplicity *N-3*. Only the coefficients w_n obtained from (3.4) are affected by ψ_n.

Rotational Mode: In general, the rotational and translational modes couple together for arbitrary planet spacing and no special modal structure can be identified. For certain planet spacing, however, they still have distinguishing properties. A case of particular interest is that of diametrically opposed planets, which is common in industrial applications. Consider a system with each of *N/2* pairs of planets located along arbitrarily oriented diameters. A pair of opposing planets have the position relation $\psi_{n+N/2}=\psi_n+\pi$. In this case,

$$\sum w_n \sin\psi_n = 0 \qquad \sum w_n \cos\psi_n = 0 \qquad \sum w_n = 0 \tag{3.8}$$

Accordingly, systems satisfying (3.8) have six rotational modes with property (3.5). For arbitrarily distributed planets not satisfying (3.8), rotational modes do not exist.

Translational Mode: While the translational modes couple with the rotational modes for truly arbitrary planet spacing, they retain their structure for systems satisfying (3.8). The notable difference with equally spaced planet systems is that the natural frequencies are no longer degenerate because the cyclic symmetry is disturbed. To start

with, the planet deflection relations in a translational mode are derived from (3.7) for any three planets *i, j, k*,

$$\sin(\psi_i - \psi_j)\mathbf{p}_k + \sin(\psi_j - \psi_k)\mathbf{p}_i + \sin(\psi_k - \psi_i)\mathbf{p}_j = \mathbf{0} \tag{3.9}$$

Thus, the *n*-th planet deflection can be expressed as a linear combination of $\mathbf{p}_1$ and $\mathbf{p}_2$. The component modal deflections for a translational mode become

$$\mathbf{p}_h = [x_h, y_h, u_h], \quad h = c,r,s, \quad \mathbf{p}_n = [\sin(\psi_2 - \psi_n)\mathbf{p}_1 + \sin\psi_n \mathbf{p}_2]/\sin\psi_2 \tag{3.10}$$

Therefore, planetary gears with planet positions satisfying (3.8) (for example, diametrically opposed planets) have twelve distinct vibration modes that have the special structure (3.10) of a translational mode.

3.3 Modal Strain and Kinetic Energy

The vibration modes can be further characterized by modal strain and kinetic energy. The total modal strain energy U and kinetic energy T are related to the natural frequencies and vibration modes by

$$U = \frac{1}{2}\phi_i^T \mathbf{K} \phi_i = U_c + U_{cu} + U_r + U_{ru} + U_s + U_{su} + \sum_{n=1}^{N}(U_n + U_{rn} + U_{sn}) \tag{3.11}$$

$$T = \frac{1}{2}\omega_i^2 \phi_i^T \mathbf{M} \phi_i = T_c + T_{cu} + T_r + T_{ru} + T_s + T_{su} + \sum_{n=1}^{N}(T_n + T_{nu}) \tag{3.12}$$

where (i) U_h, U_{hu}, $h= c,r,s$ are the strain energies in the translational and rotational support springs, respectively, of the carrier, ring and sun; (ii) U_n, U_{rn}, U_{sn}, $n=1, \ldots, N$ are the strain energies in the *n*-th planet bearing, ring-planet mesh and sun-planet mesh; and

(iii) T_h, T_{hu}, h=c, r, s and T_n, T_{nu} are the modal translational and rotational kinetic energies, respectively, of the carrier, ring, sun, and planets. The detail of these individual energies are

$$
\begin{aligned}
&U_h = \frac{1}{2}k_h(x_h^2 + y_h^2), \quad U_{hu} = \frac{1}{2}k_{hu}u_h^2, \qquad h = c,r,s \\
&U_n = \frac{1}{2}k_n[(\delta_{nr})^2 + (\delta_{nt})^2], \quad U_{sn} = \frac{1}{2}k_{sn}(\delta_{sn})^2, \quad U_{rn} = \frac{1}{2}k_{rn}(\delta_{rn})^2 \\
&T_h = \frac{m_h}{2}\omega_i^2(x_h^2 + y_h^2), \qquad T_h = \frac{I_h}{2r_h^2}\omega_i^2 u_h^2, \qquad h = c,r,s \\
&T_n = \frac{m_p}{2}\omega_i^2(\zeta_n^2 + \eta_n^2), \qquad T_{nu} = \frac{I_p}{2r_p^2}\omega_i^2 u_n^2
\end{aligned}
\tag{3.13}
$$

where the mesh and bearing deflections δ are defined below.

sun-planet mesh: $\delta_{sn} = y_s\cos\psi_{sn} - x_s\sin\psi_{sn} - \zeta_n\sin\alpha_s - \eta_n\cos\alpha_s + u_s + u_n + e_{sn}$ (3.14)

ring-planet mesh: $\delta_{rn} = y_r\cos\psi_{rn} - x_r\sin\psi_{rn} - \zeta_n\sin\alpha_r + \eta_n\cos\alpha_r + u_r - u_n + e_{rn}$ (3.15)

planet bearing radial: $\delta_{nr} = y_c\sin\psi_n + x_c\cos\psi_n - \zeta_n$ (3.16)

planet bearing tangential: $\delta_{nt} = y_c\cos\psi_n - x_c\sin\psi_n - \eta_n + u_c$ (3.17)

For the example planetary gear (Appendix B, case II), the modal strain and kinetic energy distributions are shown in Figure 3.2, and the dominant motion and strain energy are listed in Table 3.1. According to (3.13), the dominant kinetic energy occurs in the component with dominant motion. Modal strain energy indicates those vibration modes most susceptible to parameter variation and identifies the most heavily loaded component for response. In the next chapter, the modal energy distribution will be used in the derivation of simple formulae to calculate eigensensitivity to key design parameters.

3.4 Discussions

Planet modes of multiplicity *N-3* are remarkably insensitive to planet location and retain their special properties for arbitrary planet spacing. Coupling between rotational and translational modes occurs for arbitrary planet spacing, and distinct properties can not be identified. For systems satisfying (3.8), however, rotational and translational modes have structured properties. This includes the common case of equally spaced and diametrically opposed planet pairs. The foregoing development applies to general epicyclic gear configurations. Configurations having fixed or floating components are obtained by letting the associated bearing stiffness approach zero or infinity to obtain the eigensolution properties. For example, for the cases of a fixed ring, fixed sun or fixed carrier, a *3(N+2)* degree of freedom system is obtained. The vibration modes in such systems consist of five rotational, five pairs of translational and three groups of planet modes.

The free vibration properties have been validated through a finite element computation. A finite element model (Figure 3.3) for this system was built by Agashe (1998) and Parker, *et al.* (2000) and analyzed with CALYX (Vijayakar, 1991). Computational modal analyses were performed by applying impulse inputs and obtaining the frequency response functions. The identified natural frequencies match the analytical results (Table 3.2) within 3.3 percent difference.

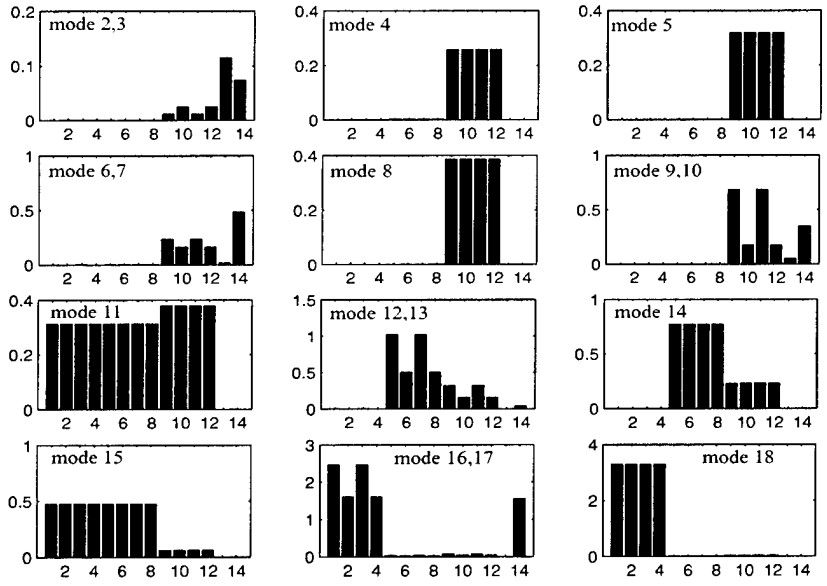

(a) Normalized modal strain energy at the sun/planet meshes (1-4), ring/planet meshes (5-8), planet bearings (9-12), carrier and sun bearings (13, 14).

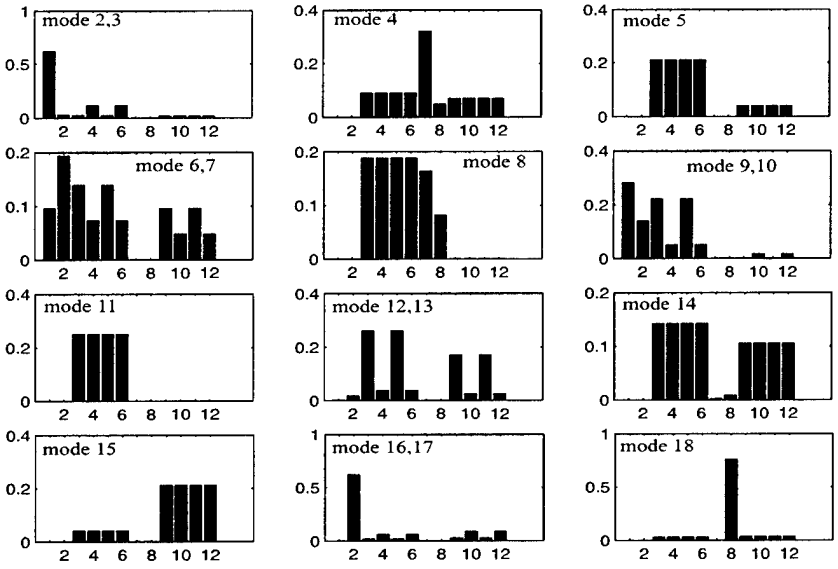

(b) Normalized modal kinetic energy at the carrier, sun, planet translations (1,2,3-6), and carrier, sun, planet rotations (7,8,9-12).

Figure 3.2 Modal energy distributions of the system in Appendix B, case II.

No.	f(Hz)	Type	Dominant motion	Dominant strain energy
1	0	R	Rigid body mode	
2,3	825	T	All components	Carrier, sun bearings
4	1661	R	All components	Planet bearings
5	1808	P	Planet radial translation	Planet bearings
6,7	1834	T	Sun, planet translation	Sun, planet bearings
8	1985	R	Sun rotation, planet translation	Planet bearings
9,10	2326	T	Sun, planet translation	Sun, planet bearings
11	5964	P	Planet tangential translation	All meshes
12,13	6429	T	Planets	Ring-planet meshes
14	6451	R	Planets	Ring-planet meshes
15	6982	P	Planet rotation	All meshes
16,17	10430	T	Sun translation	Sun-planet meshes
18	13068	R	Sun rotation	Sun-planet meshes

Table 3.1 Dominant motion and modal strain energy in the vibration modes of the system in Appendix B. R: rotational mode, T: translational mode, P: planet mode.

Mode Type	Trans	Rot	Plan	Trans	Rot	Trans
FEM (Hz)	778	1144	1729	1676	1723	2110
Analytical (Hz)	769	1156	1609	1710	1781	2175
Difference (%)	1.2	-1.0	2.3	-2.0	-3.3	-3.0

Table 3.2 Comparison of analytical and FEM natural frequency analyses.

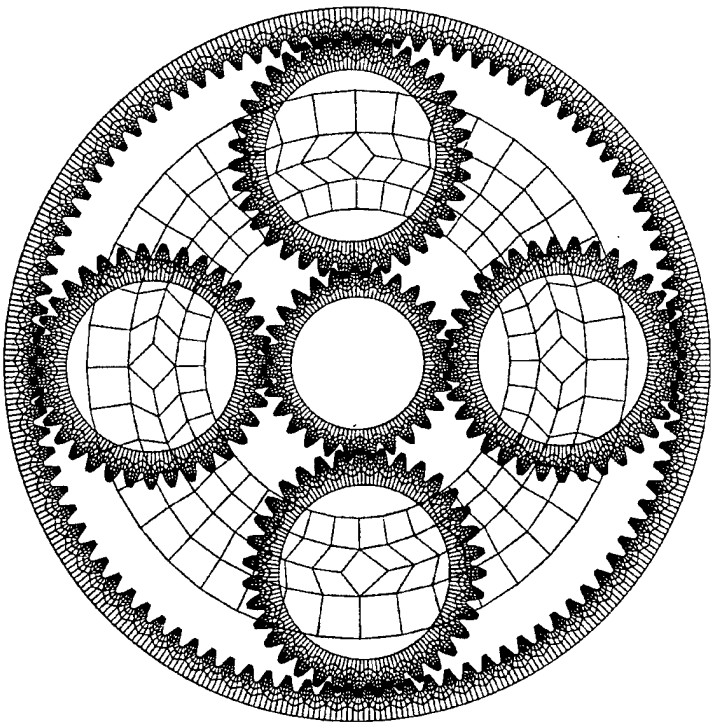

Figure 3.3 Finite element model of the planetary gear

The well-defined eigensolution properties are useful for subsequent research because almost all analytical investigation of planetary gear vibration phenomena ultimately require the natural frequencies and vibration modes. This includes, for example, critical dynamic behaviors such as forced response to static transmission error, use of planet phasing to eliminate excitation of particular modes, parametric instability from time-varying mesh stiffness, contact loss nonlinearities, natural frequency and vibration mode sensitivity to key design parameters and gyroscopic effects. The specific properties characterized in this paper theoretically explain the selective participation of

the different classes of vibration modes in planetary gear dynamic response (Parker et al., 2000a; Parker, 2000). Additionally, the structured vibration mode properties lead to simple, exact formulae to calculate natural frequency and vibration mode sensitivity to parameter changes (Lin and Parker, 1999b). Using these properties, well-defined veering rules of natural frequency loci are analytically derived (Lin and Parker, 2000b). These special veering rules help to trace the evolution of the loci for changes in the design parameters and identify the veering zones where vibration modes undergo dramatic changes. Apart from analytical applications, the identified natural frequency structure provides important information for tuning the system frequencies to avoid resonance. There are at most 15 different natural frequencies in general planetary gears with N planets, so there are only 15 potential resonant frequencies.

CHAPTER 4

EIGENSENSITIVITY TO DESIGN PARAMETERS

During the design process, system parameters are varied to evaluate alternative design choices, avoid resonances, optimize load distribution, and reduce weight. It is important to characterize the effects of parameter variations on the natural frequencies and vibration modes for effective vibration tuning. In planetary gear dynamic models (Figure 2.2), the key design parameters include the mesh stiffnesses, support/bearing stiffnesses, component masses, and moments of inertia. The influence of some design parameters on planetary gear natural frequencies was touched on in a few papers. Botman (1976) and Cunliffe et al. (1974) both presented plots of natural frequencies versus planet bearing stiffness. Kahraman (1994c) showed the effects of mesh/bearing stiffnesses on the natural frequencies in his torsional model of planetary gears. Saada and Velex (1995) discussed the influence of ring support stiffness on free vibration. These analyses were based on parametric studies of example planetary gears and assume the planetary gears to be cyclically symmetric (tuned) systems. Eigensensitivity analysis for mistuned systems is necessary to identify the critical modes that are susceptible to irregularity. Frater et al. (1983) studied the vibration modes with one unbalanced mesh stiffness, but general

conclusions were not obtained. This project analytically investigates the natural frequency and vibration mode sensitivity to most system parameters such as mesh/bearing stiffnesses, component masses and moments of inertia. Simple, closed-form expressions are obtained to calculate eigensensitivities for both tuned and mistuned system. In addition, eigenvalue veering phenomena are investigated to identify dramatic changes of natural frequencies and strong coupling of vibration modes. Design guidelines are summarized from eigensensitivity and veering analyses to predict influences of system parameters on planetary gear free vibration.

4.1 Calculation of Eigensensitivity

The eigensensitivity analysis calculates natural frequency and vibration mode derivatives with respect to stiffnesses, masses, moments of inertia and the carrier rotation speed Ω_c. Eigensensitivity to stiffness and inertia design parameters are examined in the absence of gyroscopic effects Ω_c. Gyroscopic effects are important in high-speed applications such as aircraft engines, and eigensensitivity with respect to Ω_c is studied separately in section 4.4. The eigenvalue problem for the study is in form (3.2), *i.e.,*

$$(\mathbf{K} - \lambda_i \mathbf{M})\phi_i = \mathbf{0} \tag{4.1}$$

where $\lambda_i=\omega_i^2$. The eigensensitivity for problems in the form (4.1) has been thoroughly investigated (Courant and Hilbert, 1953; Adelman and Haftka, 1986; Friswell, 1996) and the necessary results are introduced below. The unique modal properties of planetary

gears are then invoked to reduce these general results to simple expressions specific to planetary gears.

Let $(\,)'$ and $(\,)''$ denote the first and second derivatives with respect to a model parameter (*i.e.* mesh/bearing stiffness, component mass or moment of inertia). For simplicity, the eigenvalue derivatives λ_i' and λ_i'' are calculated; the relations $\omega_i'=\lambda_i'/(2\omega_i)$ and $\omega_i''=(2\lambda_i\lambda_i''-\lambda_i'^2)/(4\omega_i^3)$ yield the natural frequency sensitivities. For a distinct eigenvalue, the eigensensitivities are (Fox and Kapoor, 1968; Rogers, 1970)

$$\lambda_i' = \phi_i^T(\mathbf{K}' - \lambda_i\mathbf{M}')\phi_i \tag{4.2}$$

$$\phi_i' = -\frac{1}{2}(\phi_i^T\mathbf{M}'\phi_i)\phi_i + \sum_{k=1}^{L}\frac{\phi_k^T(\mathbf{K}' - \lambda_i\mathbf{M}')\phi_i}{\lambda_i - \lambda_k}\phi_k \tag{4.3}$$

$$\lambda_i'' = 2\phi_i^T(\mathbf{K}' - \lambda_i\mathbf{M}')\phi_i + \phi_i^T(\mathbf{K}'' - \lambda_i\mathbf{M}'' - 2\lambda_i'\mathbf{M}')\phi_i \tag{4.4}$$

For the case of degenerate eigenvalues, consider a system having a group of eigenvalues $\lambda_1=\ldots=\lambda_m$ with multiplicity m. The first-order eigenvalue derivatives λ_i' are the eigenvalues of

$$\mathbf{D}\mathbf{a}_i = \lambda_i'\mathbf{a}_i, \quad \mathbf{D} = \Gamma^T(\mathbf{K}' - \lambda_i\mathbf{M}')\Gamma \tag{4.5}$$

where $\Gamma=[\gamma_1,\ldots,\gamma_m]$ is an arbitrary set of independent eigenvectors associated with this degenerate eigenvalue and is normalized such that $\Gamma^T\mathbf{M}\Gamma = \mathbf{I}_{m\times m}$. For the case when all λ_i' obtained from (4.5) are distinct, the $\mathbf{a}_i$ are uniquely obtained with the normalization $\mathbf{a}_i^T\mathbf{a}_i=1$. This procedure determines the set of independent eigenvectors $\phi_i=\Gamma\mathbf{a}_i$ that admit continuous change of the eigenvectors as the degenerate eigenvalues split into distinct ones when a parameter is varied.

The eigenvector derivatives for distinct λ_i' are expressed as (Friswell, 1996)

$$\phi_i' = \mathbf{v}_i + \Phi \mathbf{c}_i, \qquad i = 1,\cdots,m \tag{4.6}$$

where

$$v_i = \sum_{k=m+1}^{L} \frac{\phi_k^T (\lambda_i \mathbf{M}' - \mathbf{K}')\phi_i}{\lambda_k - \lambda_i} \phi_k \tag{4.7}$$

$$c_{ji} = \frac{2\phi_j^T (\mathbf{K}' - \lambda_i \mathbf{M}')\mathbf{v}_i + \phi_j^T (\mathbf{K}'' - \lambda_i \mathbf{M}'' - 2\lambda_i' \mathbf{M}')\phi_i}{\lambda_i' - \lambda_j'}, \qquad j \neq i \tag{4.8}$$

$$c_{ii} = -\frac{1}{2}\Phi^T \mathbf{M}' \Phi \tag{4.9}$$

The second derivatives are

$$\lambda_i'' = 2\phi_i^T (\mathbf{K}' - \lambda_i \mathbf{M}')\mathbf{v}_i + \phi_i^T (\mathbf{K}'' - \lambda_i \mathbf{M}'' - 2\lambda_i' \mathbf{M}')\phi_i, \qquad i=1,\cdots,m \tag{4.10}$$

For the case when all λ_i' obtained from (4.5) are degenerate, the $\mathbf{a}_i$ are not unique and hence ϕ_i, $i=1,\ldots, m$ are arbitrary in the eigenspace. The eigenvector derivatives can not be determined when these degenerate modes do not separate. However, λ_i'' can be obtained from the eigenvalues of (Friswell, 1996)

$$\mathbf{E} = 2\Phi^T (\mathbf{K}' - \lambda_i \mathbf{M}')\mathbf{V} + \Phi^T (\mathbf{K}'' - \lambda_i \mathbf{M}'' - 2\lambda_i' \mathbf{M}')\Phi \tag{4.11}$$

where $\mathbf{V}=[\mathbf{v}_1,\ldots,\mathbf{v}_m]$ is determined by (4.7). λ_i'' are not affected by the selection of Φ.

The foregoing development is used subsequently to derive general, closed-form eigensensitivity relations for λ_i', ϕ' and λ_i'' for planetary gears. These expressions yield eigensolution approximations according to

$$\tilde{\lambda} = \lambda + \sum_{\rho} \frac{\partial \lambda}{\partial \rho}\Big|_{\rho=\rho_0} (\rho - \rho_0), \qquad \tilde{\phi} = \phi + \sum_{\rho} \frac{\partial \phi}{\partial \rho}\Big|_{\rho=\rho_0} (\rho - \rho_0) \tag{4.12}$$

where ρ represents any system parameter with nominal value ρ_0 and multiple parameter perturbations are permitted. Eigensolutions λ, ϕ are for a nominal set of model

parameters referred to as the *unperturbed* system, and the derivatives are evaluated for this unperturbed system. Eigensolutions $\tilde{\lambda}$, $\tilde{\phi}$ are for the *perturbed* system with varied parameters. The unperturbed system is taken to be tuned in this study. Note that this does not meaningfully restrict the results because parameter variations leading to both tuned and mistuned perturbed systems are examined.

4.2 Eigensensitivity to Mesh and Support Stiffnesses

The stiffnesses under consideration (Figure 2.2) include mesh stiffnesses k_{rn}, k_{sn}, transverse support stiffnesses k_c, k_r, k_s, k_n, and rotational support stiffnesses k_{cu}, k_{ru}, k_{su}. The natural frequency sensitivity to a certain stiffness is found to be uniquely associated with the modal strain energy occurring in that spring. To demonstrate the procedure, let the sun-planet mesh stiffness k_{sn} be the varied parameter.

4.2.1 Tuned System

Considered the case where all sun-planet mesh stiffnesses k_{sn}=k_{sp} are altered equally so the perturbed system remains tuned. For rotational modes, the eigensensitivities are obtained from (4.2)-(4.4)

$$\frac{\partial \lambda_i}{\partial k_{sp}} = \sum_{n=1}^{N} (\delta_{sn}^i)^2 \tag{4.13}$$

$$\frac{\partial \phi_i}{\partial k_{sp}} = \sum_{\substack{k=1 \\ k \neq i}}^{L} \sum_{n=1}^{N} \frac{\delta_{sn}^k \delta_{sn}^i}{\lambda_i - \lambda_k} \phi_k \tag{4.14}$$

$$\frac{\partial^2 \lambda_i}{\partial k_{sp}^2} = \sum_{\substack{k=1 \\ k \neq i}}^{L} \frac{2}{\lambda_i - \lambda_k} \left(\sum_{n=1}^{N} \delta_{sn}^k \delta_{sn}^i \right)^2 \tag{4.15}$$

where δ_{sn}^i is the spring deformation of the sun-planet n mesh in mode ϕ_i given (3.14). The rotational mode property (3.5) dictates that all sun-planet mesh deformations are equal, *i.e.*, $\delta_{sn}^i = \delta_{s1}^i$, so (4.13) becomes

$$\frac{\partial \lambda_i}{\partial k_{sp}} = N(\delta_{s1}^i)^2 \tag{4.16}$$

In (4.14), ϕ_i' is expressed as a modal expansion of eigenvectors, and the contribution of each eigenvector is readily obtained from the coefficients of ϕ_k. When two eigenvalues λ_i and λ_k are nearly equal, the influence of ϕ_k on ϕ_i' is dominant because the denominator in its coefficient is small. In such cases, the second derivative ϕ_i'' is also large, and the natural frequency changes rapidly with k_{sp}.

The translational mode eigenvalues $\lambda_{1,2}$ do not separate because the perturbed system remains tuned. Thus, the matrix **D** in (4.5) has degenerate eigenvalues λ_1', λ_2'. Accordingly, the unperturbed eigenvectors $\phi_{1,2}$ can not be uniquely determined from the procedure associated with (4.5), and $\Phi=[\phi_1, \phi_2]$ are an arbitrary pair of translational modes of the unperturbed system. From (4.5), λ_1', λ_2' are the eigenvalues of

$$\mathbf{D} = \Phi^T \mathbf{K}' \Phi = \sum_{n=1}^{N} \begin{bmatrix} (\delta_{sn}^1)^2 & \delta_{sn}^1 \delta_{sn}^2 \\ \delta_{sn}^1 \delta_{sn}^2 & (\delta_{sn}^2)^2 \end{bmatrix} \tag{4.17}$$

Use of the translational mode property (3.6) yields $\sum_{n=1}^{N}(\delta_{sn}^{1})^2 = \sum_{n=1}^{N}(\delta_{sn}^{2})^2$, $\sum_{n=1}^{N}\delta_{sn}^{1}\delta_{sn}^{2} = 0$. Thus, the eigenvalues of **D** (*i.e.*, λ_1', λ_2') are degenerate and have the form (4.13) for *i=1,2*. From (4.11) and the translational mode properties, λ_1'', λ_2'' are

$$\frac{\partial^2 \lambda_i}{\partial k_{sp}^2} = \sum_{k=3}^{L}\sum_{n=1}^{N}\frac{2(\delta_{sn}^{k}\delta_{sn}^{i})^2}{\lambda_j - \lambda_k}, \qquad i,j = 1,2 \tag{4.18}$$

Planet modes are also degenerate and the procedure is similar to that for translational modes. For planet modes $\Phi=[\phi_1,...,\phi_2]$, the elements of the matrix **D** are $D_{ij} = \sum \delta_{sn}^{1}\delta_{sn}^{2}$ for *i,j=1,...,m*. Applying planet mode property (3.3) to calculate δ_{sn}^{i} results in $D_{11}=...= D_{mm}$ and $D_{ij}=0$, $i\neq j$. It follows that all λ_i' of a group of planet modes are equal and can also be expressed as (4.13) for *i,j=1,...,m*. In the same way, all λ_i'', *i,j=1,...,m* are equal and of the form (4.18).

Equation (4.13), which is valid for all three types of vibration modes, can be related to the modal strain energy U in ϕ_i. With the definition of strain energy U_{sn} in (3.13), (4.13) becomes

$$\frac{\partial \lambda_i}{\partial k_{sp}} = \frac{2}{k_{sp}}\sum_{n=1}^{N}U_{sn}, \qquad \frac{\partial \omega_i}{\partial k_{sp}} = \frac{1}{\omega_i k_{sp}}\sum_{n=1}^{N}U_{sn} \tag{4.19}$$

Equation (4.19) allows one to obtain the natural frequency sensitivity to sun-planet mesh stiffness by inspection of the modal strain energy distribution.

As an example, consider a planetary gear used in the transmission of a U.S. Army OH-58 helicopter. The nominal model parameters are listed in Appendix B, case II. The natural frequencies from (4.1) are shown in Figure 4.1a for a range k_{sp}. The strain

energies of each spring are calculated according to (3.11) and their distribution in mode 16 (a translational mode) is shown in Figure 4.1b,c for two cases: k_{sp}=*70 N/μm* and k_{sp}=*500 N/μm*. The associated vibration mode ϕ_{16} is also shown for these two cases. Little strain energy is stored in the sun-planet meshes U_{sn} for case I, while substantial strain energy results in case II. Consequently, ω_{16} is more sensitive to k_{sp} in case II than in case I. This conclusion is consistent with the larger slope of the ω_{16} locus for case II in Figure 4.1a. In fact, natural frequency sensitivities to *all* stiffnesses can be obtained quantitatively directly from the strain energy distribution using (4.19) and analogous relations (4.20) and (4.21) below.

$$\frac{\partial \lambda_i}{\partial k_h} = x_h^2 + y_h^2 = \frac{2}{k_h} U_h, \qquad \frac{\partial \lambda_i}{\partial k_{hu}} = u_h^2 = \frac{2}{k_h} U_{hu}, \qquad h = c, r, s \tag{4.20}$$

$$\frac{\partial \lambda_i}{\partial k_h} = \sum_{n=1}^{N} (\delta_{nr}^i)^2 + (\delta_{nt}^i)^2 = \frac{2}{k_p} \sum_{n=1}^{N} U_n, \qquad \frac{\partial \lambda_i}{\partial k_{rp}} = \sum_{n=1}^{N} (\delta_m^i)^2 = \frac{2}{k_{rp}} \sum_{n=1}^{N} U_m \tag{4.21}$$

These relations apply for all three types of vibration modes. Expressions for ϕ_i' and λ_i'' for all of the stiffness parameters are collected in Lin and Parker (1999b). Recalling the special properties of vibration modes, (4.19)-(4.21) imply that

1. Rotational modes are independent of the transverse support stiffnesses of the carrier, ring, and sun because these components have no deformation of, and hence no modal strain energy in, their transverse support springs. Thus, use of a "floating" sun, ring, or carrier *i.e.*, low stiffness support) has no impact on rotational modes.
2. Translational modes are similarly independent of the rotational support stiffnesses of the carrier, ring, and sun.
3. Planet modes are insensitive to all carrier, ring, and sun support stiffnesses.

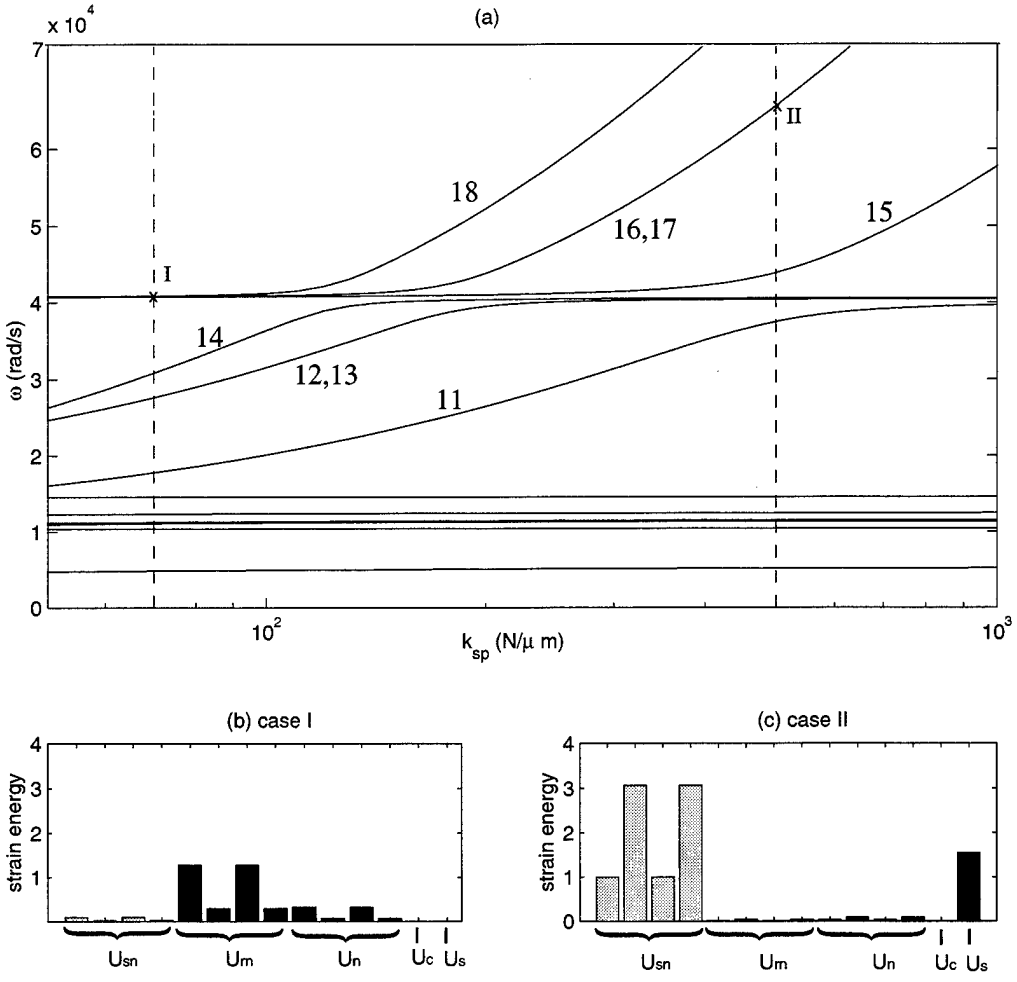

Figure 4.1 (a) natural frequency versus the sun-planet mesh stiffness k_{sp}. (b), (c) Mode 16 strain energy distribution in case I and case II. All U are defined in (3.11).

4.2.2 Mistuned System

In practical planetary gears, mistuning may be caused by differing mesh stiffnesses between planets due to differing numbers of teeth in contact, manufacturing variations, and assembly errors. To study the effects of mistuning on eigensolutions, we examine the sensitivity to parameter variations that differ between the planets. Consider an example with only the first sun-planet mesh stiffness k_{s1} varying from the nominal (unperturbed) value k_{sp}. The derivatives of the mass and stiffness matrices with respect to k_{s1} are $\mathbf{M}'=\mathbf{M}''=\mathbf{K}''=0$, $\mathbf{K}' = \partial\mathbf{K} / \partial k_{s1}$.

The eigensensitivities of the rotational modes are obtained from (4.2)-(4.4)

$$\frac{\partial \lambda_i}{\partial k_{s1}} = (\delta_{s1}^i)^2 = \frac{2}{k_{s1}} U_{s1} \tag{4.22}$$

$$\frac{\partial \phi_i}{\partial k_{s1}} = \sum_{\substack{k=1 \\ k\neq i}}^{L} \frac{\delta_{s1}^k \delta_{s1}^i}{\lambda_i - \lambda_k} \phi_k \tag{4.23}$$

$$\frac{\partial^2 \lambda_i}{\partial k_{s1}^2} = \sum_{\substack{k=1 \\ k\neq i}}^{L} \frac{2}{\lambda_i - \lambda_k} (\delta_{s1}^k \delta_{s1}^i)^2 \tag{4.24}$$

Equation (4.22) relates λ_i' to the modal strain energy in the first sun-planet mesh. Equations (4.22)-(4.24) are similar to (4.13)-(4.15) without the summation over n because the varying parameter is located only at the first sun-planet mesh.

For translational modes, the eigensensitivities are (Lin and Parker, 1999b)

$$\frac{\partial \lambda_1}{\partial k_{s1}} = (\delta_{s1}^1)^2, \qquad \frac{\partial \lambda_2}{\partial k_{s1}} = (\delta_{s1}^2)^2 = 0 \tag{4.25}$$

$$\frac{\partial \phi_1}{\partial k_{s1}} = \sum_{k=3}^{L} \frac{\delta_{s1}^k \delta_{s1}^i}{\lambda_1 - \lambda_k} \phi_k, \qquad \frac{\partial \phi_2}{\partial k_{s1}} = \mathbf{0} \tag{4.26}$$

$$\frac{\partial^2 \lambda_1}{\partial k_{s1}^2} = \sum_{k=3}^{L} \frac{2(\delta_{s1}^k \delta_{s1}^i)^2}{\lambda_1 - \lambda_k}, \qquad \frac{\partial^2 \phi_2}{\partial k_{s1}^2} = \mathbf{0} \tag{4.27}$$

The behavior of ϕ_1 and ϕ_2 is shown in Figure 4.2 for the example of Appendix B, case II. A pair of translational mode natural frequencies separate as a disorder $\varepsilon=k_{s1}/k_{sp}-1$ is introduced. The modal strain energy distributions in the four sun-planet meshes are shown for $\varepsilon = 0, -0.1$. ϕ_1 is sensitive to k_{s1} because of the high strain energy in the first sun-planet mesh. ϕ_2 has no strain energy in the first sun-planet mesh and is independent of k_{s1}. The linear ($\lambda_2 + \varepsilon k_{sp}\lambda_2'$) and quadratic ($\lambda_2 + \varepsilon k_{sp}\lambda_2' + \varepsilon^2 k_{sp}\lambda_2''$) approximations of the loci are shown in Figure 4.2 and agree well with the exact loci. These two loci intersect exactly at $\varepsilon = 0$ when there is only one disorder in the perturbed system. If one more disorder $\varepsilon_2=k_{s2}/k_{sp}-1= 0.1$ is added at the second mesh (Figure 4.3), the two loci suddenly change direction and veer away. For an initially tuned (cyclically symmetric) system, two independent varying parameters (*e.g.*, k_{s1} and k_{s2}) are necessary to break the symmetry of both ϕ_1 and ϕ_2 and cause frequency loci veering (Happawana et al., 1998). The regular perturbation does not give a good approximation in the veering zone where two loci are close to each other. Singular or improved perturbation methods are needed (Pierre and Murthy, 1992; Wu, 1993; Chen et al., 1995; Lin and Lim, 1997). If the number of planets N= 4 or 5, the planet modes have multiplicity $m=1,2$ and their eigensensitivities are obtained from (4.22)-(4.24) or (4.25)-(4.27). When $N>5$, eigensolutions of matrix **D** in (4.5) are difficult to achieve in closed-form, but can be obtained numerically.

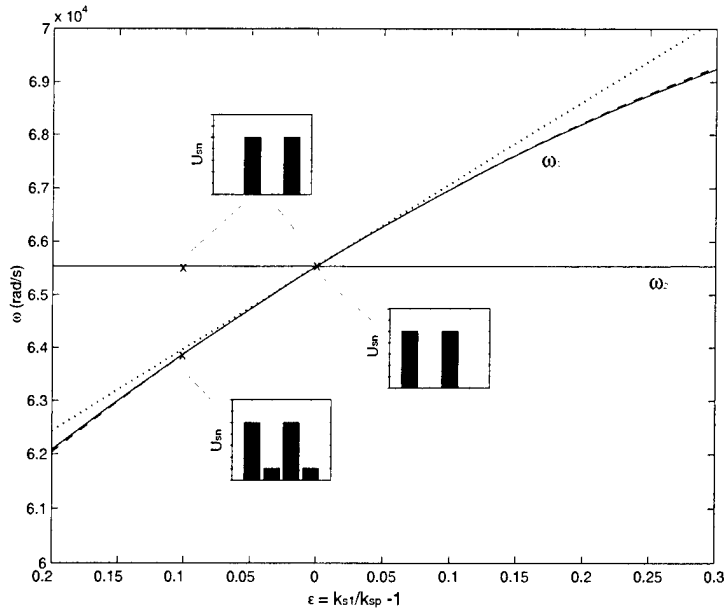

Figure 4.2 Influence of the disorder ε on the natural frequencies. Linear (...) and quadratic (---) approximations agree well with the exact loci (—).

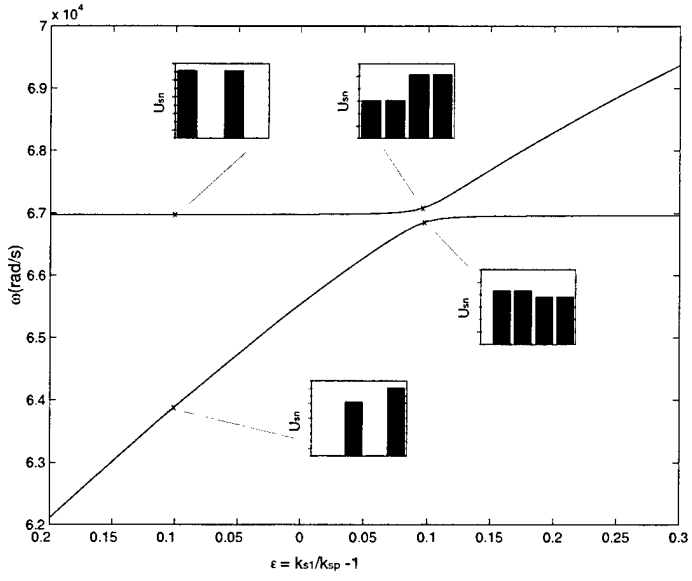

Figure 4.3 Influence of two disorders on the natural frequencies. Another disorder $\varepsilon_2=k_{s2}/k_{sp}-1=0.1$ at the second mesh is added to the system shown in Figure 4.2.

4.3 Eigensensitivity to Gear Mass and Inertia

The parameters of interest consist of masses (m_c, m_r, m_s, m_p) and moments of inertia (I_c,I_r, I_s, I_p) for the carrier, ring, sun, and planets. When the perturbed system remains tuned, the eigenvalue derivatives for the three types of modes are

$$\frac{\partial \lambda_i}{\partial m_h} = -\lambda_i (x_h^2 + y_h^2) = -\frac{2}{m_h} T_h, \qquad \frac{\partial \lambda_i}{\partial m_{hu}} = -\lambda_i u_h^2 = -\frac{2}{I_h} T_{hu}, \qquad h = c,r,s \tag{4.28}$$

$$\frac{\partial \lambda_i}{\partial m_p} = -\lambda_i \sum_{n=1}^{N} (\zeta_n^2 + \eta_n^2) = -\frac{2}{m_p} \sum_{n=1}^{N} T_n, \qquad \frac{\partial \lambda_i}{\partial I_p} = -\frac{\lambda_i}{r_p^2} \sum_{n=1}^{N} u_n^2 = -\frac{2}{I_p} \sum_{n=1}^{N} T_{nu} \tag{4.29}$$

where T_h, T_{hu}, h=c, r, s and T_n, T_{nu} are the modal kinetic energies defined in (3.12). Expressions for ϕ_i' and λ_i'' for all of the mass and inertia parameters are collected in Lin and Parker (1999b). Figure 4.4a shows an example plot of the natural frequencies versus the sun moment of inertia I_s. Most natural frequencies are insensitive to changes in I_s. The kinetic energy distribution and vibration modes of mode 18 (a rotational mode) are shown in Figure 4.4b,c for cases I and II. The sun has more rotational kinetic energy T_{su} in case I than in case II, so ω_{18} locus has larger slope in case I. Equations (4.28) and (4.29) allow quantitative calculation of natural frequency sensitivity to all masses and moments of inertia directly from the modal kinetic energy distributions. Considering the properties of vibration modes, some conclusions are immediate from (4.28) and (4.29):

1. Rotational modes are independent of the masses of the carrier, ring, and sun because such modes have no translations of these components.
2. Translational modes are similarly independent of the moments of inertia of the carrier, ring, and sun.
3. Planet modes are independent of both masses and inertias of the carrier, ring, and sun.

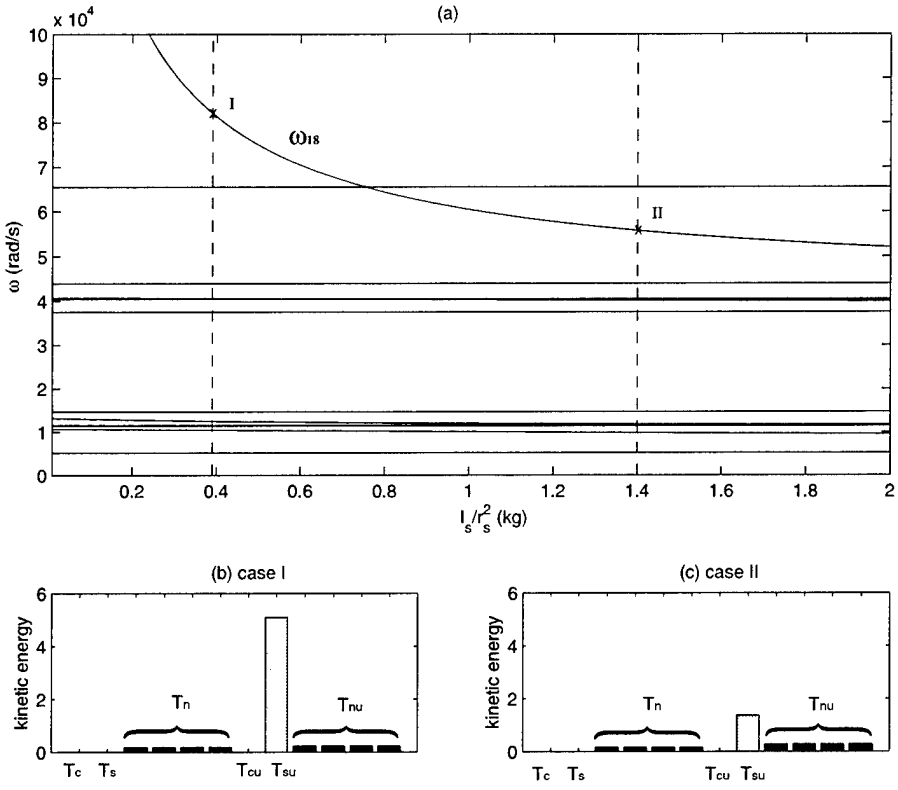

Figure 4.4 (a) Natural frequency versus the sun moment of inertia I_s. (b), (c) Mode 18 kinetic energy distribution in case I and II. The T are defined in (3.12).

4.4 Eigensensitivity to Operating Speed

In high-speed applications (*e.g.* aircraft engines), gyroscopic effects may significantly alter the system stability and dynamic behavior. Eigenvalue derivatives evaluated for $\Omega_c=0$ are calculated to assess the influence of operating speed on the natural frequency spectrum. The gyroscopic eigenvalue problem of (3.1) is obtained from the separable solution $\mathbf{q} = \phi_i e^{j\omega_i t}$

$$[-\omega_i^2\mathbf{M} + j\omega_i\Omega_c\mathbf{G} + (\mathbf{K} - \Omega_c^2\mathbf{K}_\Omega)]\phi_i = \mathbf{0} \,. \tag{4.30}$$

For practical operating speeds $\Omega_c=0$ (*i.e.*, subcritical), the eigenvalues remain purely imaginary. Suppose a zero speed natural frequency ω_i has multiplicity m and the arbitrarily chosen independent eigenvectors are $\Gamma=[\gamma_1,\ldots,\gamma_m]$ with normalization $\Gamma^T\mathbf{M}\Gamma = \mathbf{I}_{m\times m}$. While eigenvectors for $\Omega_c\neq 0$ are complex, the γ_i are real. Differentiation of (4.30) with respect to Ω_c and evaluation at $\Omega_c=0$ yield

$$(\mathbf{K} - \omega_i^2\mathbf{M})\phi_i' = (2\omega_i\omega_i'\mathbf{M} - j\omega_i\mathbf{G})\Gamma\mathbf{a}_i = \mathbf{f} \tag{4.31}$$

where $\phi_i = \Gamma\mathbf{a}_i$. Applying solvability and normalization conditions results in an $m\times m$ Hermitian eigenvalue problem

$$\mathbf{D}\mathbf{a}_i = \omega_i'\mathbf{a}_i, \qquad \mathbf{D} = j\Gamma^T\mathbf{G}\Gamma/2 \tag{4.32}$$

The natural frequency sensitivities ω_i' are obtained from the eigenvalues of (4.32) for the three classes of vibration modes. Rotational mode natural frequencies are distinct and (4.32) becomes a scalar equation. Hence $\omega_i' = 0$ because $\gamma_i^T\mathbf{G}\gamma_i = 0$ for real γ_i and skew-symmetric **G**. For translational modes γ_1 and γ_2, **D** and its eigenvalues are

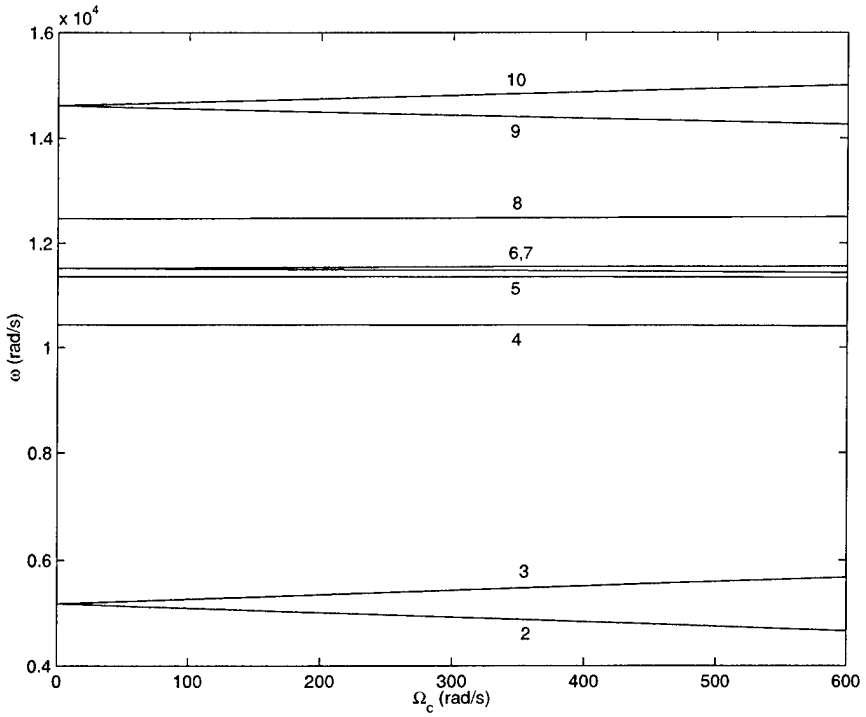

Figure 4.5 Natural frequency versus the carrier rotation speed

$$D = \frac{j}{2}\begin{bmatrix} 0 & \gamma_1^T \mathbf{G}\gamma_2 \\ -\gamma_1^T \mathbf{G}\gamma_2 & 0 \end{bmatrix}, \qquad \omega'_{1,2} = \pm\, \gamma_1^T \mathbf{G}\gamma_2 / 2 \tag{4.33}$$

For a group of planet modes $\gamma_1, \ldots, \gamma_m$, the properties (3.3) guarantee $D_{ij} = \gamma_i^T \mathbf{G}\gamma_j = 0$ for $i \neq j$. $D_{ii}=0$, $i=1, \ldots, m$ because of the skew-symmetry of **G**. Thus, **D=0** and all planet mode natural frequency sensitivities vanish, *i.e.*, $\omega_i' = 0$.

Equation (4.33) can be used to approximate the frequency loci $\tilde{\omega}_i = \omega_i + \Omega_c \omega_i'$. The result $\omega_i' = 0$ for rotational and planet modes at $\Omega_c = 0$ indicates the natural frequencies of these modes are scarcely affected by operating speed. Figure 4.5 shows the

first 10 frequency loci versus Ω_c for the gear system in Appendix B case II. The rotational mode (ω_4, ω_8) and planet mode (ω_5) loci are nearly flat lines and not sensitive to operating speed. Translational mode frequencies ($\omega_{2,3}$, $\omega_{6,7}$, $\omega_{9,10}$) split as Ω_c is increased from zero. In this example, ω_2 and ω_3 at Ω_c=*600 rad/s* deviate about 10 percent from the zero speed value. Typical helicopter carrier speeds are less than 100 *rad/s*. For applications with high speed (*e.g.* turbofan and turboprop engine systems), heavy component masses, and compliant stiffnesses, the gyroscopic effects can be more significant. If a natural frequency locus has large slope and decreases to zero in the range of operating speed, the stability and system behavior are dramatically impacted.

4.5 Natural Frequency Veering

In the plots of natural frequencies versus design parameters, eigenvalue veering occurs, where two eigenvalue loci approach each other as a parameter is varied but then abruptly veer away like two similar charges repelling (point *B* in Figure 4.6a). The phenomenon has been studied extensively (Leissa, 1974; Perkins and Mote, 1986; Pierre, 1988; Chen and Ginsberg, 1992). The vibration modes of the veering eigenvalues are strongly coupled and undergo dramatic changes in the veering neighborhood. In the case of especially sharp veering, it is sometimes difficult to distinguish between intersection and veering just by observing eigenvalue plots. When multiple curves veer or intersect close together (Figure 4.6a), strong modal coupling, and the associated operating condition response changes that occur, are not identifiable from frequency loci plots. The

objective of this work is to analytically characterize the rules of eigenvalue veering in planetary gear vibration. Simple rules emerge to predict if two eigenvalues veer or cross. The veering sharpness is also calculated.

4.5.1 Veering/Crossing Criterion

A method for detecting eigenvalue veering/crossing in general dynamic systems is developed by Perkins and Mote (1986). When two eigenvalue loci veer away, their loci curvatures indicate the abruptness of curve direction changes. Perkins and Mote estimated the loci curvature in the veering neighborhood using coupling factor

$$\chi_r = \frac{2[\phi_r^T(\mathbf{K}' - \lambda_r\mathbf{M}')\phi_s]^2}{\lambda_r - \lambda_s}, \qquad \chi_s = \frac{2[\phi_s^T(\mathbf{K}' - \lambda_r\mathbf{M}')\phi_r]^2}{\lambda_s - \lambda_r} \tag{4.34}$$

The coupling factors χ_r, χ_s approximate the local curvatures and the coupling strength. Figure 4.6b shows $\chi = \chi_{14} = -\chi_{18}$ versus the varying parameter k_{sp} for the veering loci ω_{14} and ω_{18} in Figure 4.6a. Notice the sharply changing vibration modes indicated in Figure 4.6b. The two veering loci exchange mode shapes from point *A* to *C*, even though the loci do not intersect. The modes are strongly coupled at *B* and do not look like either of the veering modes just outside the veering zone. When a parameter is adjusted in the veering zone, the drastic changes in the vibration modes can greatly impact the operating condition dynamic response, tooth loads, load sharing, and bearing forces and possibly lead to mode localization. The degree to which individual modes are excited by dynamic mesh forces (*i.e.*, the modal forces) also changes dramatically as veering alters the modes. If the coupling factors are all zero, λ_r and λ_s loci cross; otherwise, veering occurs.

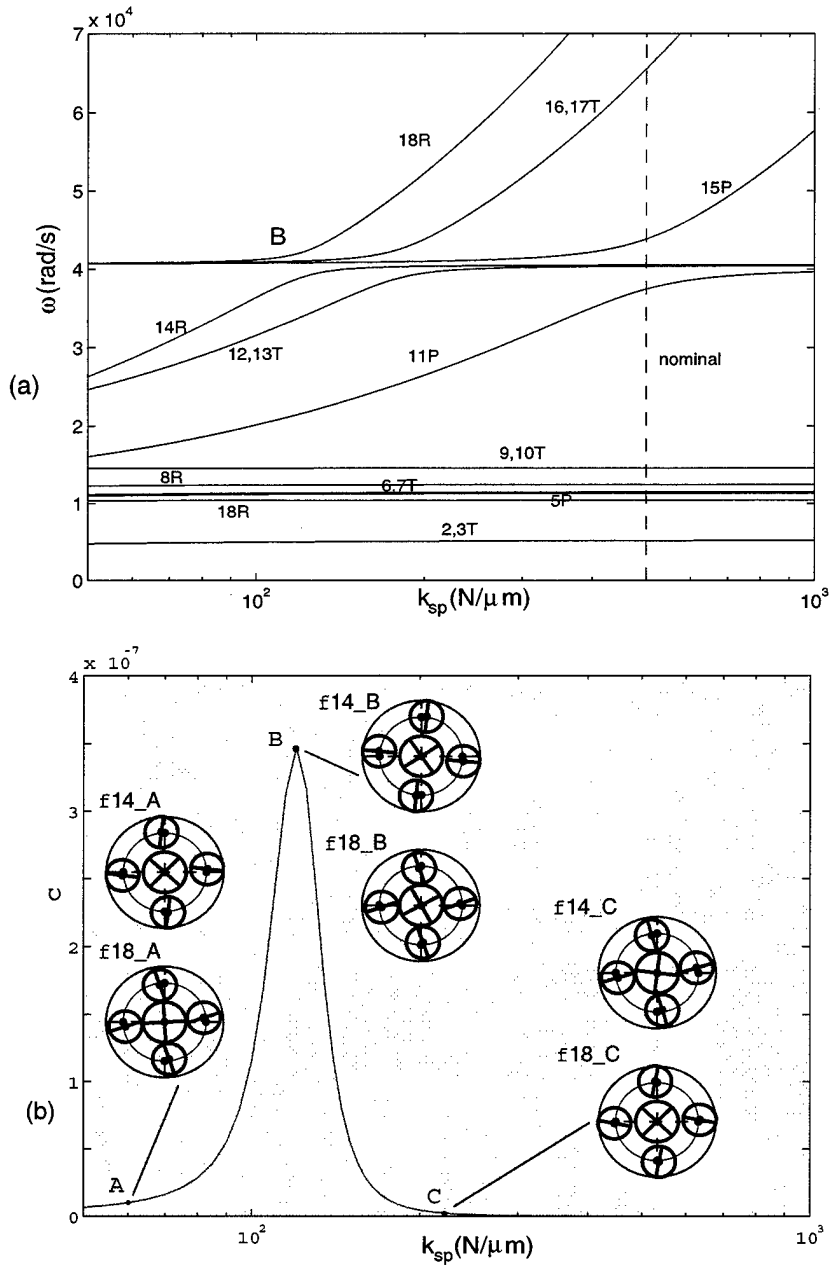

Figure 4.6 (a) Natural frequencies versus the sun-planet mesh stiffness. Natural frequencies are numbered under the nominal conditions (dashed line) in Table C.1. Three pairs of veering are loci 14 and 18, (12,13) and (16,17), and 11 and 15. (b) Coupling factor χ of ω_{14} and ω_{18}. These two loci exchange mode shapes from point *A* to *C*.

4.5.2 Veering Patterns In Planetary Gears

When applied to planetary (or any epicyclic) gears, the coupling factors reduce to particularly simple forms because of the unique structure of the vibration modes. In the frequency plots of tuned planetary gears, loci of the same type (rotational, translation, and planet modes) never cross each other but veer away when they come close. The modes of different types can cross each other but never switch modes through veering. This special veering pattern is analytically proved using the well-defined vibration mode properties (Lin and Parker, 2000b). The general veering/crossing patterns are summarized in Table 4.1. *This pattern is generally valid when stiffness or inertia parameters are varied.*

The special veering patterns are helpful to trace the evolution of eigenvalue loci and identify the effects of design parameters on planetary gear vibration. The planetary gear in a helicopter powertrain is used as an example. The nominal model parameters are given in Table C.1, case II. Table 3.1 identifies the mode type and where the dominant strain energy is in each mode. The natural frequencies are numbered at the nominal conditions (indicated by the dashed lines in Figure 4.6-11).

	R	T	P1	P2	P3
R	V	X	X	X	X
T	X	V	X	X	X
P1	X	X	---	X/V*	X/V*
P2	X	X	X/V*	---	V
P3	X	X	X/V*	V	---

Table 4.1 Veering (V) and crossing (X) patterns in planetary gears. X/V means crossing only occurs when $k_{sp}= k_{rp}$ and $\alpha_r=\alpha_s$.

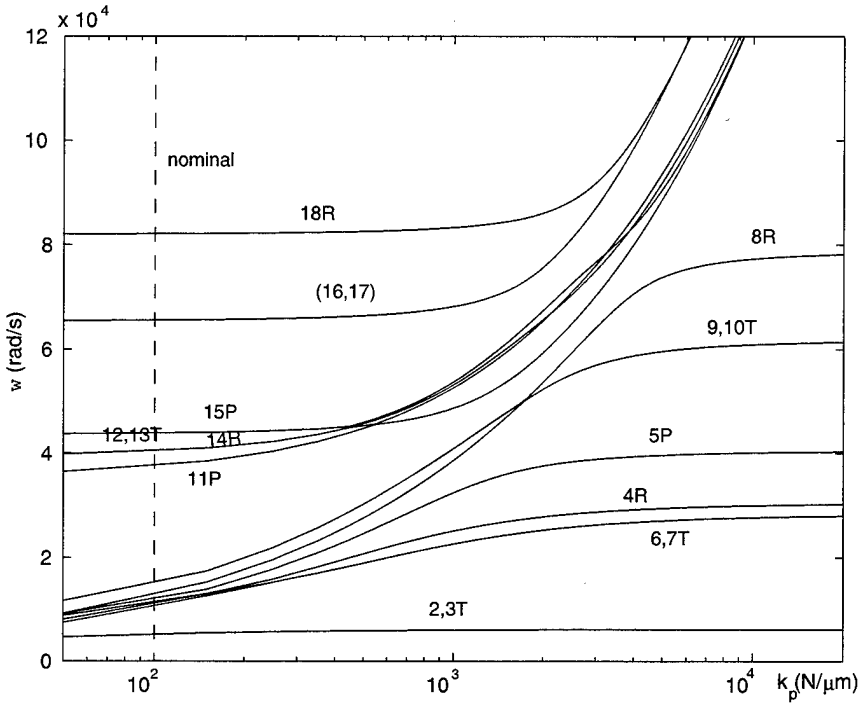

Figure 4.7 Natural frequencies versus the planet bearing stiffness k_p. The planet mode 11 (pure tangential type P1) crosses the planet mode 15 (no tangential motion type P2). The nominal conditions (dashed line) are listed in Table C.1, case II.

Mesh stiffnesses k_{sp}, k_{rp} (Figure 4.6and 4.8) have little influence on the low natural frequencies $\omega_1 \sim \omega_{10}$. This is because these modes are governed by bearing stiffnesses (Table 3.1) that are much smaller than the mesh stiffnesses. Modes 15-18 have large strain energy in the sun-planet meshes and are affected by k_{sp} (Figure 4.6); modes 11-14 have substantial strain energy in the ring-planet meshes and are affected by k_{rp} (Figure 4.8). When k_{sp} is reduced from the nominal value, the changing $\omega_{15} \sim \omega_{18}$ approach the $\omega_{11} \sim \omega_{14}$ loci. Because loci of the same type can not intersect, veering occurs between rotational modes 18 and 14, translational mode pairs (16,17) and (12,13), and planet

modes 15 and 11. Below the veering zones ($k_{sp}<100\ N/\mu m$), modes 11~14 are very similar to modes 15~18 above the veering zones ($k_{sp}>800\ N/\mu m$). In the same way, one can predict the trend of frequency loci as k_{rp} is increased (Figure 4.8). Using the derived veering patterns and modal properties, the actual modes affected by varying parameters can be detected easily although the plots are complicated by veering phenomena.

Support stiffnesses k_h, k_{hu}, $h=c,r,s$ of the carrier, ring, and sun can vary over a wide range depending on the configuration (fixing or floating these components). Rotational and planet modes are independent of the transverse support stiffness k_h because they have no translation of the carrier, ring, and sun; only translational modes are affected by changes in k_h (Figure 4.9a,b). Considering the veering effects, k_h significantly affects only one pair of translational modes with dominant strain energy in the transverse supports. When the rotational support stiffnesses k_{hu} are altered, similar results are obtained (Figure 4.9c,d), except it is the rotational modes that are susceptible to k_{hu} variations.

Altering planet parameters affects most natural frequencies as all modes involve planet deflections, in general. Applying the derived veering results, five pairs of veering are identified for changing planet bearing stiffness in Figure 4.7: rotational modes 8 and 18, 4 and 14, translational modes (9,10) and (16,17), (6,7) and (12,13), and planet modes 5 and 15. For large stiffness $k_p>5000\ N/\mu m$, eight natural frequencies increase rapidly to outside the range of interest. Planet mass m_p and moment of inertia I_p also have significant influence on the natural frequencies (Figure 4.10).

4.6 Discussion and Summary

Eigenvalue loci veering also occurs when degenerate modes of symmetric system are separated by small disorders. In planetary gears, the cyclic symmetry can be broken by differing mesh stiffnesses at each planet mesh, manufacturing variations, and assembly errors. For cyclically symmetric or periodic systems with small disorders and weak structural coupling, mode localization often accompanies eigenvalue loci veering (Pierre, 1988). Planetary gears have relatively strong coupling between the planets through the carrier and teeth meshes, so strong mode localization is unlikely even in the presence of loci veering. After examination of many cases with various configurations and parameters, the authors have not found a realistic example of mode localization in planetary gears.

The special veering patterns of planetary gear eigenvalue loci are easily summarized. Two approaching eigenvalue loci of the same type (rotational mode, translational mode, and planet mode) veer away while two loci of different mode types cross each other. The mode shapes are exchanged across the veering zone. In the veering zone, the modes are strongly coupled and markedly different than outside the zone. One can expect significant differences in response from these changed modes. These rules result from planetary gears' unique modal properties and apply to all design parameters.

The effects of key design parameters are summarized below:

1. **Mesh stiffness.** k_{sp} and k_{rp} each control three different natural frequencies associated with one rotational mode, one pair of translational modes, and one group of planet modes. Dominant strain energy occurs in the tooth meshes of these vibration modes.

2. **Carrier, ring, and sun parameters.** k_h and k_{hu}, $h=c,r,s$ each affect only one natural frequency. The transverse stiffness k_h controls one pairs of translational modes and the torsional stiffness k_{hu} controls one rotational mode. Floating or fixing the carrier, ring, or sun has limited influence on planetary gear modal properties. The carrier, ring, and sun masses and moments of inertia affect the same frequencies as their corresponding support stiffness, though the frequencies vary in the opposite direction.

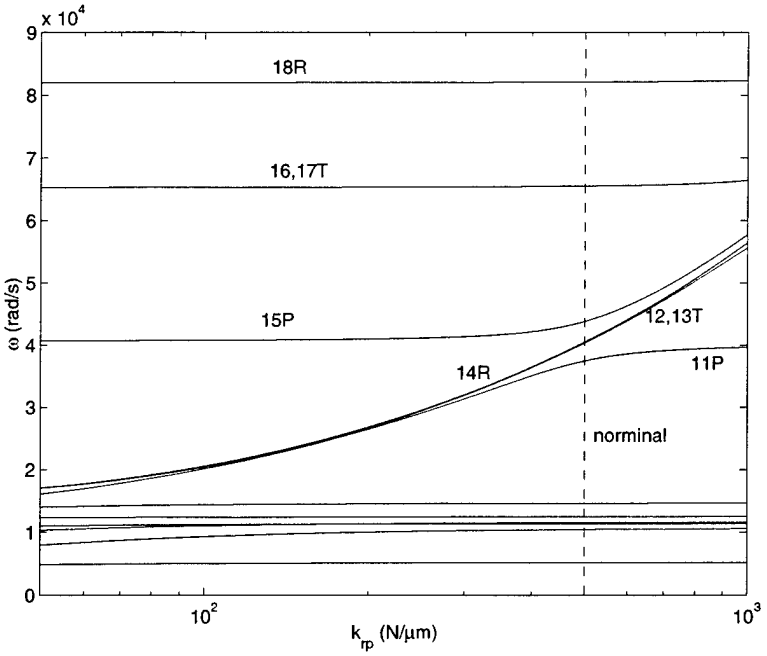

Figure 4.8 Natural frequencies versus the ring-planet mesh stiffness k_{rp}. Loci 12-14 will veer with loci 16-18 when k_{rp} is further increased. The nominal conditions (dashed line) are listed in Table C.1, case II.

3. **Planet parameters**. Planet bearing stiffness and planet inertia are the most influential parameters and affect most natural frequencies. A stiff planet bearing can be beneficial for resonance tuning because it substantially reduces the number of natural frequencies in the lower frequency range that is commonly of most interest.

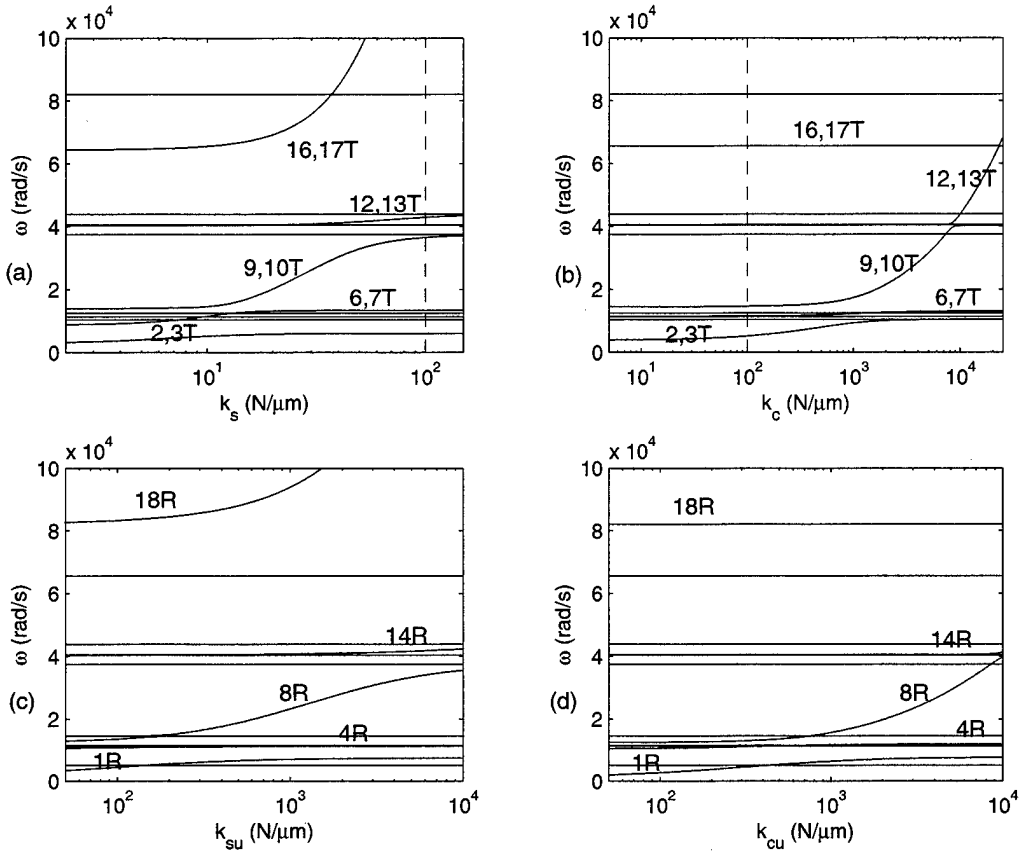

Figure 4.9 (a), (b) $k_h, h=s,c$ only affect translational modes. (c), (d) k_{hu}, $h=s,c$ only affect rotational modes. The nominal conditions (dashed line) are listed in Table C.1.

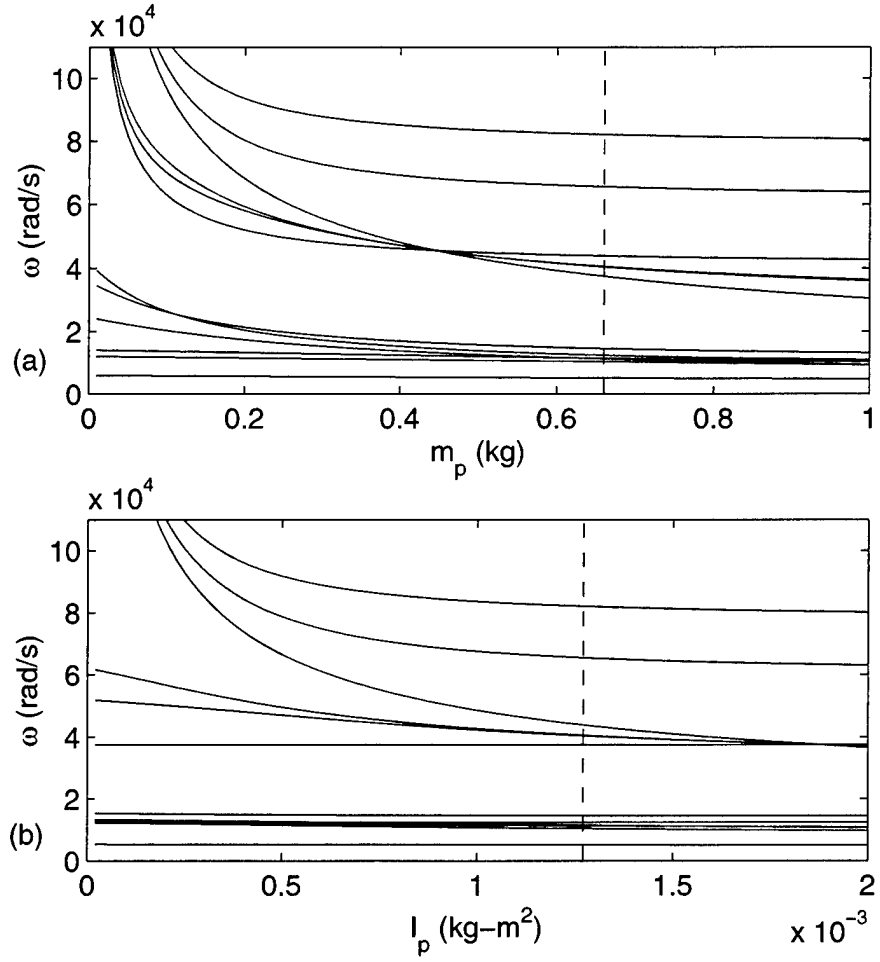

Figure 4.10 Natural frequencies versus (a) the planet mass m_p, (b) the planet moment of inertia I_p. The nominal conditions (dashed line) are listed in Table C.1.

CHAPTER 5

PARAMETRIC INSTABILITY FROM MESH STIFFNESS VARIATION

In previous chapters, the mesh stiffnesses are considered constant. Current work investigates the impacts of mesh stiffness variation on planetary gear dynamics. The variation of mesh stiffness gives rise to a parametric excitation. The linear, time-varying system studied herein is governed by a set of coupled Hill's equation

$$\mathbf{M}\ddot{\mathbf{q}} + [\mathbf{K}_0 + \mathbf{K}_v(t)]\mathbf{q} = \mathbf{F}(t) \tag{5.1}$$

where $\mathbf{K}_0$ is the mean stiffness matrix and $\mathbf{K}_v(t)$ is the variational part of the stiffness matrix. $\mathbf{F}(t)$ is the external excitation. $\mathbf{K}_v(t)$ is periodic with frequency Ω (mesh frequency). Mesh stiffness depends on element compliance, tooth error, profile modification, transmitted torque, and the position of contact (Kasuba and Evans, 1981). When $\mathbf{K}_v(t)$ is simple harmonic in t, (5.1) becomes a set of coupled Mathieu equations.

The parametric excitation from $\mathbf{K}_v(t)$ causes instability and severe vibration when harmonics of the excitation frequencies are close to particular combinations of the natural frequencies. Three types of instability are of most interest: (1) primary instability $\Omega \approx 2\omega_p$, (2) secondary instability $\Omega \approx \omega_p$, and (3) combination instability $\Omega \approx \omega_p + \omega_q$. The objective of this study is to systematically determine the operating conditions leading to parametric

instabilities in planetary gears. As discussed in Chapter 1, the existing analysis on parametric instability is scarce, inconsistent, and incomplete for multi-mesh gears systems. A simple two-stage gear chain is analyzed first, and then the analysis is extended to planetary gears with multiple meshes. Perturbation methods are used in this study to determine the boundaries separating the stable and unstable regions. Floquet theory and numerical integration are used to validate the analytical findings. The effects of contact ratios and mesh phasing on parametric instability are quantitatively identified. The interaction of instability, tooth separation nonlinearity, and dynamic response is discussed.

5.1 Two Stage Gear Systems

5.1.1 System Model

Two-stage gear trains have three-gear and four-gear configurations (Figure 5.1). The gear bodies and intermediate shaft connecting gears 2 and 4 are assumed rigid. The tooth meshes are modeled as linear springs with stiffnesses k_{L1}, k_{L2}. The anchored shaft is flexible with torsional stiffness k_{L0}. The gears have base radii r_i, $i=1,2,3,4$. Only rotational vibrations θ_1, θ_2, θ_3 are considered. The equivalent masses are $m_1= I_1/r_1^2$, $m_2= I_2/r_2^2$, and $m_3= vI_3/r_3^2$, where I_i are the moments of inertia of the gears and their connected shafts, $v=r_4/r_2$ for four-gear trains, and $v=1$ for three-gear chains. The equivalent stiffnesses are $k_0= k_{L0}/r_1^2$, $k_1= k_{L1}$, and $k_2= v^2k_{L2}$. The shaft/gear rotations are measured by the base radius deflections $x_1= \theta_1 r_1$, $x_2= \theta_2 r_2$, and $x_3=\theta_3 r_3/v$. The system stability is governed by the free vibration equation

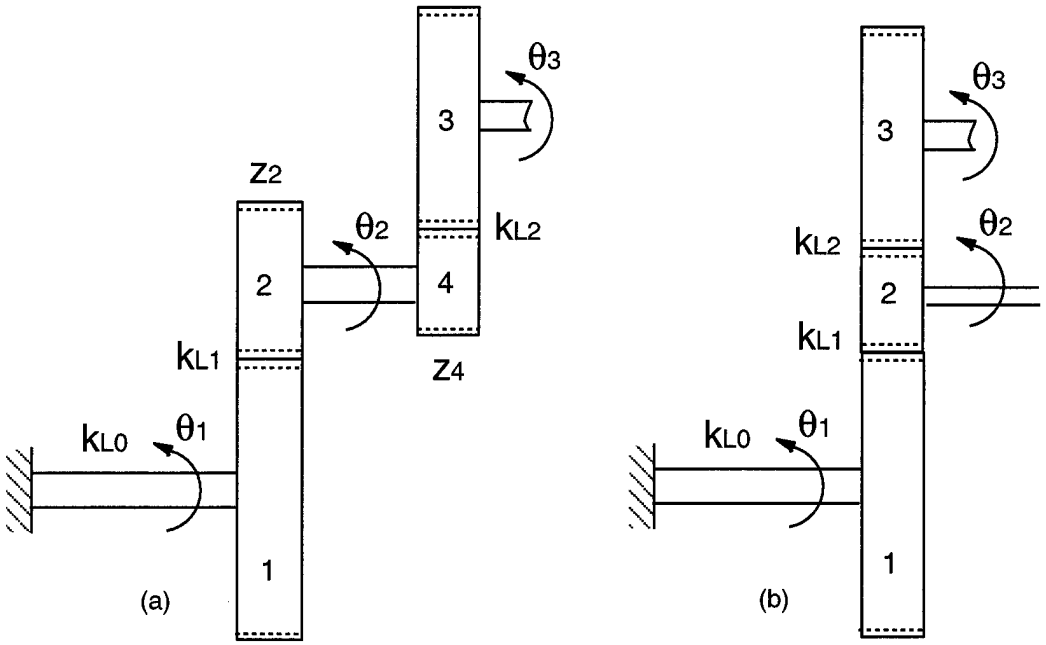

Figure 5.1 Two-stage gear systems with (a) four gears and (b) three gears. k_{L1}, k_{L2} denote mesh stiffnesses and Z_2, Z_4 are numbers of gear teeth. k_{L0} is the torsional stiffness of the anchored shaft.

$$\mathbf{M}\ddot{\mathbf{q}} + [\mathbf{K}_0 + \mathbf{K}_v(t)]\mathbf{q} = 0 \tag{5.2}$$

where $\mathbf{q} = [x_1,\ x_2, x_3]^{\mathrm{T}}$. $\mathbf{M}$=*diag*(m_1, m_2 , m_3) is the inertia matrix. The stiffness matrix is represented by a mean value $\mathbf{K}_0$ and a variational part $\mathbf{K}_v(t)$ as

$$\mathbf{K}_0 = \begin{bmatrix} k_{g1} + k_0 & k_{g1} & 0 \\ k_{g1} & k_{g1} + k_{g2} & k_{g2} \\ 0 & k_{g2} & k_{g2} \end{bmatrix} \qquad \mathbf{K}_v(t) = \begin{bmatrix} k_{v1} & k_{v1} & 0 \\ k_{v1} & k_{v1} + k_{v2} & k_{v2} \\ 0 & k_{v2} & k_{v2} \end{bmatrix} \tag{5.3}$$

where k_{gi} and $k_{vi}(t)$ are the mean and time-varying components of the mesh stiffnesses, $k_i(t) = k_{gi} + k_{vi}(t)$ (Figure 5.2). The variational parts $k_{vi}(t)$ are periodic at the mesh frequency Ω_i and expressed in Fourier series as

$$k_{vi}(t) = 2k_{ai}\sum_{l=1}^{\infty}(a_i^{(l)}\sin s\Omega_i t + b_i^{(l)}\cos s\Omega_i t), \qquad i = 1,2 \tag{5.4}$$

where $2k_{ai}$ is the peak-to-peak amplitude of k_{vi} (Figure 5.2). The mesh frequencies Ω_1 and Ω_2 are related by $\Omega_1 = R\Omega_2$, where $R = Z_2/Z_4$ and Z_2, Z_4 are the numbers of teeth on gears *2* and *4* (Figure 5.1a). Note $R = 1$, $\Omega_1 = \Omega_2$ for three-gear systems (Figure 5.1b). Mesh stiffness variation is obtained through measurement, calculation, or simple specification (*e.g.*, sinusoidal or rectangular wave). For spur gears, rectangular waves are often used to approximate the mesh stiffness alternating between n and $n+1$ pairs of teeth in contact (Kahraman and Blankenship, 1999a). In this study, the k_{vi} are specified as rectangular waves with variational amplitudes k_{ai}, periods $T_i = \Omega_i/2\pi$, contact ratios c_i, and phasing angles $p_i T_i$ (Figure 5.2b). Thus,

$$a_i^{(l)} = -\frac{2}{l\pi}\sin[l\pi(c_i - 2p_i)]\sin(l\pi c_i), \qquad b_i^{(l)} = -\frac{2}{l\pi}\cos[l\pi(c_i - 2p_i)]\sin(l\pi c_i) \tag{5.5}$$

in (5.4) for $l = 1, 2, \cdots$. Without loss of generality, one can specify $p_1 = 0$, $p_2 = h$ (h is called mesh phasing). In practice, the first three or four Fourier terms reasonably approximate the mesh stiffness variation.

For the time-invariant case, the eigenvalue problem associated with (5.1) is $\mathbf{K}_0\phi_i = \omega_i^2\mathbf{M}\phi_i$. The vibration modes ϕ_i are normalized as $\Phi^{\mathrm{T}}\mathbf{M}\Phi = \mathbf{I}$ with $\Phi = [\phi_1, \phi_2, \phi_3]$. Applying the modal transformation $\mathbf{q} = \Phi\mathbf{u}$ and using (5.4), equation (5.2) becomes

$$\begin{aligned} \ddot{u}_n + \omega_n^2 u_n + \sum_{r=1}^{3}\sum_{l=1}^{\infty}[2\varepsilon_1(D_{nr}^{(l)}\sin l\Omega_1 t + E_{nr}^{(l)}\cos l\Omega_1 t) \\ + 2\varepsilon_2(F_{nr}^{(l)}\sin l\Omega_2 t + G_{nr}^{(l)}\cos l\Omega_2 t)]u_r = 0, \qquad n = 1,2,3 \end{aligned} \tag{5.6}$$

where $\varepsilon_i = k_{ai}/k_{gi}$, $i = 1, 2$ and the matrices **D**, **E**, **F**, **G** are

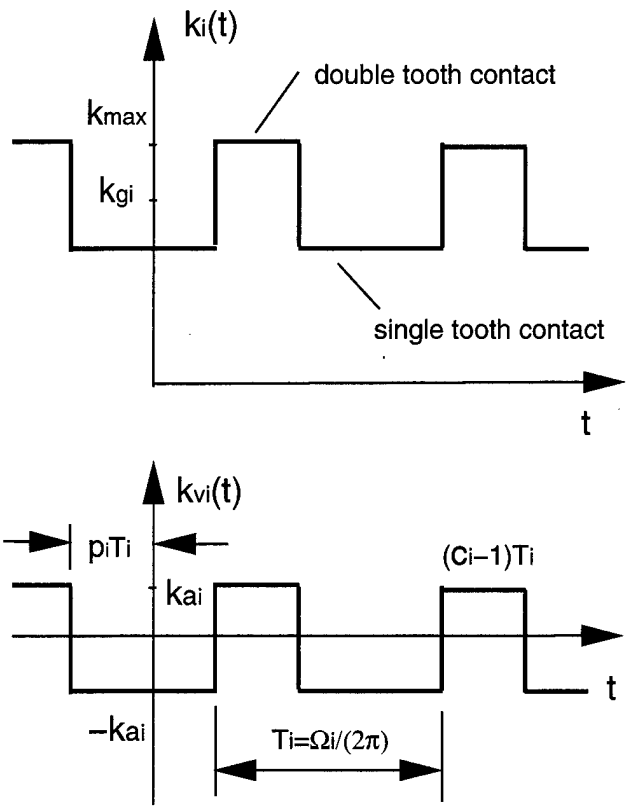

Figure 5.2 Modeling of mesh stiffnesses $k_i(t) = k_{gi} + k_{vi}(t)$. c_i are contact ratios, k_{gi} are average mesh stiffnesses, and $p_i T_i$ are phasing angles.

$$\mathbf{D}^{(l)} = k_{g1}\Phi^T \begin{bmatrix} a_1^l & a_1^l & 0 \\ a_1^l & a_1^l & 0 \\ 0 & 0 & 0 \end{bmatrix} \Phi \qquad \mathbf{E}^{(l)} = k_{g1}\Phi^T \begin{bmatrix} 0 & 0 & 0 \\ 0 & b_1^l & b_1^l \\ 0 & b_1^l & b_1^l \end{bmatrix} \Phi$$

$$\mathbf{F}^{(l)} = k_{g2}\Phi^T \begin{bmatrix} a_2^l & a_2^l & 0 \\ a_2^l & a_2^l & 0 \\ 0 & 0 & 0 \end{bmatrix} \Phi \qquad \mathbf{G}^{(l)} = k_{g2}\Phi^T \begin{bmatrix} 0 & 0 & 0 \\ 0 & b_2^l & b_2^l \\ 0 & b_2^l & b_2^l \end{bmatrix} \Phi \tag{5.7}$$

Equation (5.6) is a set of coupled Hill's equations subjected to multi-frequency parametric excitations from two gear meshes.

5.1.2 Conditions of Parametric Instability

Parametric instability depends on the frequency, amplitude, and shape of the parametric excitations. In gear systems, these factors are directly associated with the operating speed and gear design parameters such as contact ratio, facewidth, diametral pitch, pressure angle, material properties, and so on. The corresponding model parameters are the stiffness variation amplitudes k_{a1}, k_{a2}, mesh frequencies Ω_1, Ω_2, contact ratios c_1, c_2, and mesh phasing h.

The variation amplitudes k_{ai} are assumed small compared to the average mesh stiffnesses k_{gi}, so $\varepsilon_i = k_{ai}/k_{gi} << 1$ in (5.6). At this point, $\varepsilon_1 = \varepsilon_2 = \varepsilon$ is specified; the case of $\varepsilon_1 \neq \varepsilon_2$ is discussed later. Using the method of multiple scales, three different mesh conditions are examined.

1. Three-gear Systems: Equal Mesh Stiffness Variations

In three-gear systems (Figure 5.1b), the two meshes have the same mesh frequencies $\Omega_1 = \Omega_2 = \Omega$. We consider the case where the gear facewidths and material properties, which primarily determine mesh stiffness for a given number of teeth in contact, are such that the amplitudes of mesh stiffness variation are the same at the two meshes ($\varepsilon_1 = \varepsilon_2 = \varepsilon$). The contact ratios and mesh phasing are allowed to differ between the two meshes, however. In practice, the contact ratios are changed using center distance, diametral pitch, pressure angle, tooth addendum, and other parameters. The mesh phasing depends on the layout of the gears and the numbers of teeth.

The parametric instability when $s\Omega$ is close to $\omega_p+\omega_q$ is considered. Let $l\Omega = \omega_p + \omega_q + \sigma\varepsilon$, where σ is a detuning parameter. Using multiple scale method in (5.6), the boundaries of the instability regions are (Lin and Parker, 2000c)

$$\Omega = \frac{1}{s}(\omega_p + \omega_q \pm \varepsilon\sqrt{\Lambda_{pq}^{(l)}}) \qquad \Lambda_{pq}^{(l)} = \frac{1}{\omega_p\omega_q}[(D_{pq}^{(l)} + F_{pq}^{(l)})^2 + (E_{pq}^{(l)} + G_{pq}^{(l)})^2] \tag{5.8}$$

For single mode instabilities ($p=q$), equation (5.8) becomes

$$\Omega = \frac{2\omega_p}{l} \pm \frac{\varepsilon}{l\omega_p}[(D_{pp}^{(l)} + F_{pp}^{(l)})^2 + (E_{pp}^{(l)} + G_{pp}^{(l)})^2]^{1/2}, \qquad l=1,2,\ldots \tag{5.9}$$

As an example, Figure 5.3 shows the boundaries for primary ($l=1$), secondary ($l=2$), and combination ($p\neq q$, $l=1$) instabilities. The parameters are given in Table 5.1 and $c_1 = c_2 = 1.5$, $h = 0$. Floquet theory, numerical integration to compute the fundamental matrix, and the fundamental matrix eigenvalues (Nayfeh and Mook, 1979) are used to determine the actual instability regions denoted by * in the figures. The first-order approximations from (5.8) agree well with the numerical solution, even when ε is not small. In Figure 5.3, the instability region around $\Omega \approx 2\omega_3$ is much larger than that of the primary instabilities around $2\omega_1$ and $2\omega_2$. This is explained by examining the vibration modes. From (5.8), the primary instability boundary slopes are governed by $\sqrt{\Lambda_{pp}^{(l)}}$. Expansion of **D**, **E**, **F**, **G** in (5.7) yields the diagonal terms

$$\begin{aligned} D_{pp}^{(l)} &= k_{g1}(\phi_{1p} + \phi_{2p})^2 a_1^{(l)}, & F_{pp}^{(l)} &= k_{g2}(\phi_{2p} + \phi_{3p})^2 a_2^{(l)} \\ E_{pp}^{(l)} &= k_{g1}(\phi_{1p} + \phi_{2p})^2 b_1^{(l)}, & G_{pp}^{(l)} &= k_{g2}(\phi_{2p} + \phi_{3p})^2 b_2^{(l)} \end{aligned} \tag{5.10}$$

where ϕ_{1p}, ϕ_{2p}, ϕ_{3p} are the gear rotations in mode ϕ_p. Let $\delta_{1p}=\phi_{1p}+\phi_{2p} = x_1+x_2$ be the relative deflection of the first mesh in mode ϕ_p. Similarly, $\delta_{2p}=\phi_{2p}+\phi_{3p} = x_2+x_3$ represents the modal deflection in the second mesh. For the primary instability boundary around $2\omega_p$, insertion of (5.10) into (5.8) yields

$$\Lambda_{pp}^{(1)} = [(k_{g1}\delta_{1p}^2 a_1^{(1)} + k_{g2}\delta_{2p}^2 a_2^{(1)})^2 + (k_{g1}\delta_{1p}^2 b_1^{(1)} + k_{g2}\delta_{2p}^2 b_2^{(1)})^2]/\omega_p^2 \tag{5.11}$$

The mesh deflections δ_1, δ_2 in each mode can be observed from the mode shapes (Figure 5.4). The two meshes in ϕ_1 are both in phase and have smaller δ_1, δ_2 than those of ϕ_3, where the two meshes are both out of phase. Thus, $\Lambda_{33}^{(1)} > \Lambda_{11}^{(1)}$ and the instability boundaries around $2\omega_3$ have larger slope than those around $2\omega_1$. Mode ϕ_2 has one mesh in phase and the other out of phase, so the size of its primary instability regions is between that of ϕ_1 and ϕ_3 ($\Lambda_{33}^{(1)} > \Lambda_{22}^{(1)} > \Lambda_{11}^{(1)}$). In addition, the mesh deflections in a vibration mode are related to the modal strain energy $U_1 = k_1\delta_1^2/2$, $U_2 = k_2\delta_2^2/2$. Examination of (5.11) shows that vibration modes with more strain energy in the meshes have larger instability regions and are more susceptible to parametric excitations. The above results apply for mesh stiffness variations of arbitrary shape.

For mesh stiffnesses having rectangular waveforms, one can clearly identify the effects of contact ratios and mesh phasing on the instability regions. Use of (5.5) in (5.11) yields

$$\begin{aligned}\Lambda_{pp}^{(1)} = [&k_{g1}^2\delta_{1p}^4 \sin^2(c_1\pi) + k_{g2}^2\delta_{2p}^4 \sin^2(c_2\pi) + \\ &2k_{g1}k_{g2}\delta_{1p}^2\delta_{2p}^2 \sin(c_1\pi)\sin(c_2\pi)\cos(c_1 - c_2 + 2h)\pi](\frac{2}{\pi\omega_p})^2\end{aligned} \tag{5.12}$$

Inertia	$m_1=1,\ m_2=0.3,\ m_3=4.0$
Average mesh stiffness	$k_{g1}=k_{g2}=1$
Shaft stiffness	$k_0=0.5$
Contact ratio	$1\le c_1, c_2 \le 2$
Mesh phasing	$p_1=0,\ 0\le p_2=h\le 1$
Variational amplitude	$0\le k_{a1}, k_{a2} \le 0.5$

Table 5.1 Parameters of an example system in Figure 5.2.

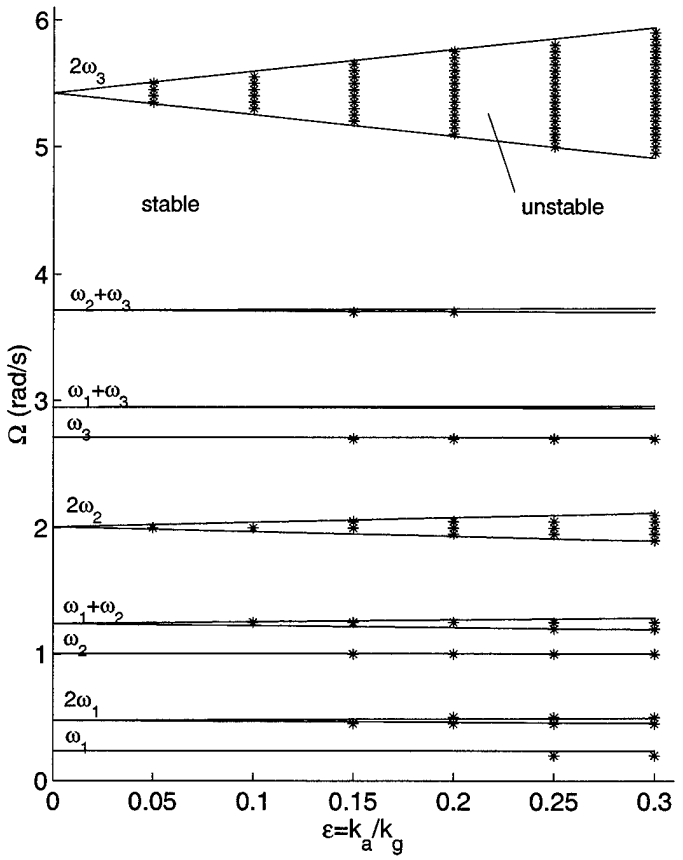

Figure 5.3 Instabilities regions when $\Omega_1=\Omega_2=\Omega, \varepsilon_1=\varepsilon_2=\varepsilon$; — analytical solution; *** numerical solution. The parameters are from Table 5.1 and $c_1=c_2=1.5,\ h=0$.

The minimum value $\Lambda_{pp}^{(1)} = 0$ is obtained when $\sin c_1\pi = \sin c_2\pi = 0$ and the unstable region vanishes. This is achieved for integer contact ratios c_1, c_2 where the number of tooth pairs in contact remains constant and mesh stiffnesses are time-invariant. For given, non-integer $c_{1,2}$ between *1* and *2*, $\Lambda_{pp}^{(1)}$ is minimized by setting $\cos(c_1 - c_2 + 2h)\pi = -1$ or $c_1 - c_2 + 2h = \pm 1, 3$. By properly choosing the contact ratios and mesh phasing, the parametric instability regions can be dramatically reduced. Figure 5.5 compares the instability regions for three cases. The most severe condition for primary instabilities (dash-dot lines) is $c_1 = c_2 = 1.5$ and $h = 0$, which maximizes $\Lambda_{pp}^{(1)}$ in (5.12). This condition is markedly improved by changing the phasing $h = 0.5$ so that $c_1 - c_2 + 2h = 1$ (dashed lines). When the contact ratios are close to integers (solid lines, $c_1 = 1.1,\ c_2 = 1.9,\ h = 0.4$), the primary instability region becomes even smaller.

Similar conditions are obtained for secondary and combination instabilities (Lin and Parker, 2000c). Unfortunately, the primary, secondary, and combination instability regions cannot be minimized at the same time. The conditions reducing the primary instability regions (dashed lines, Figure 5.5) result in large combination instability regions, and *vice versa* (dash-dot lines). Depending on specific applications, a trade-off may be made to reduce multiple instability regions, though none are true minima (solid lines). Adjusting contact ratios and mesh phasing is clearly an effective means to minimize instability regions and avoid resonances under operating conditions.

2. Four-gear Systems: Equal Mesh Stiffness Variations

Two-stage countershaft systems (Figure 5.1a) have two different mesh frequencies $\Omega_1 = R\Omega_2$, which means more instability regions than three-gear systems. We consider the case where the

gear facewidth and material are such that the mesh stiffness amplitudes are identical at the two meshes ($\varepsilon_1=\varepsilon_2=\varepsilon$), although the contact ratios and phasing are not restricted. Depending on the ratio $R=Z_2/Z_4$, the parametric instability regions associated with Ω_1 and Ω_2 may overlap each other. For $R = m/j$ (m, j are integers), the $l=j$ instabilities (single mode and combination) of Ω_1 and the $l=m$ instabilities of Ω_2 occur simultaneously. Because their instability regions are typically the largest, the interactions involving either m or $j=1$ are of most interest.

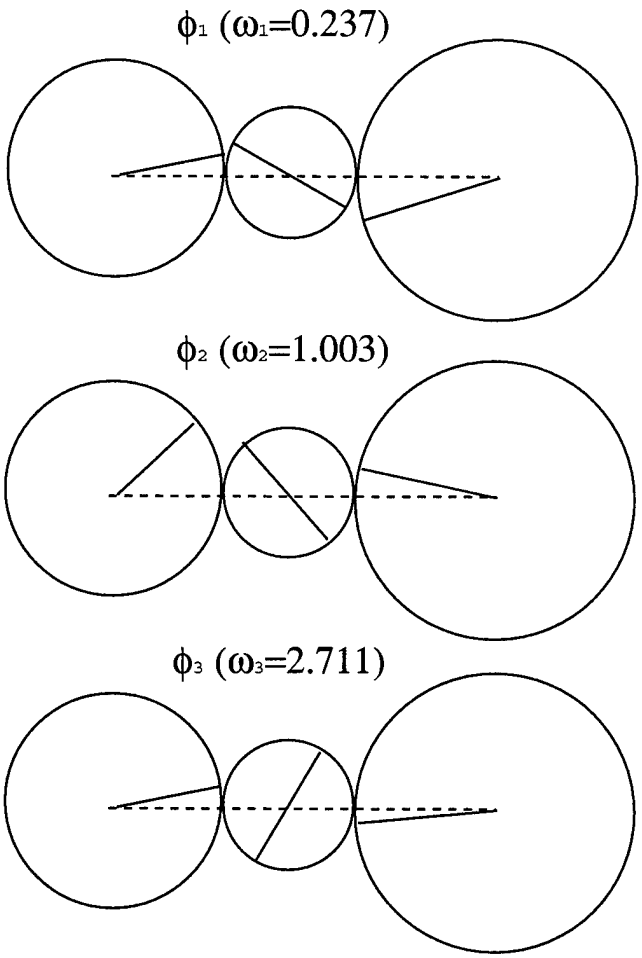

Figure 5.4 Vibration modes for the time-invariant system with parameters in Table 5.1.

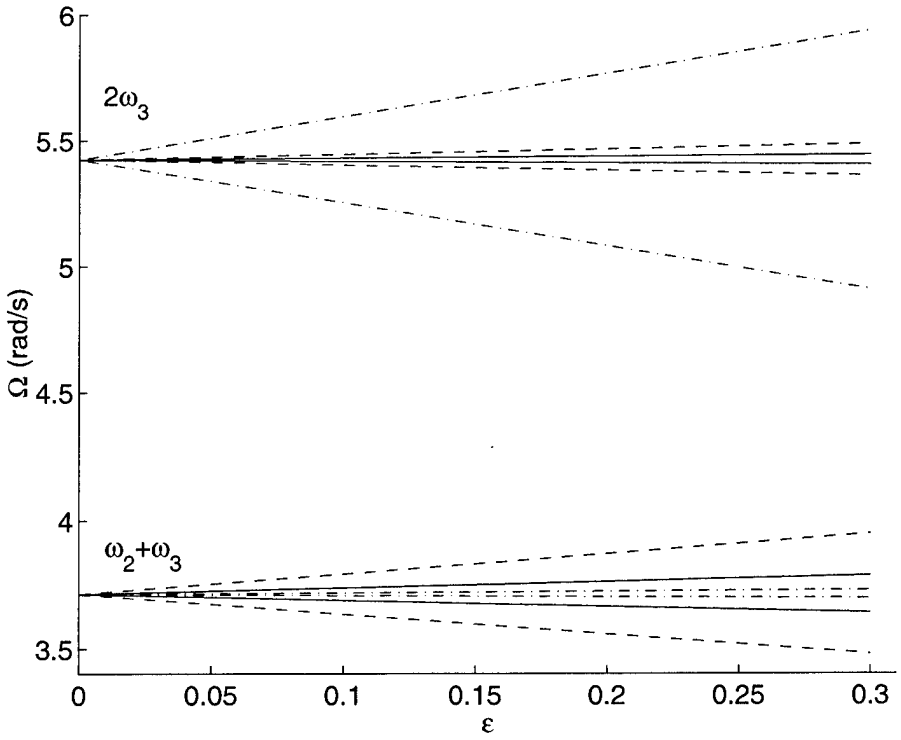

Figure 5.5 Comparison of instability regions for various contact ratios and mesh phasing. The parameters are in Table 5.1. --- $c_1 = c_2 = 1.5,\ h = 0.5$; —$c_1 = 1.1,\ c_2 = 1.9,\ h = 0.4$; -·-·- $c_1 = c_2 = 1.5,\ h = 0$.

When $R \neq m,\ 1/m$ for integer m, the $l=1$ instabilities from one mesh decouple from the $l=m$ instabilities of the other mesh. In this case, instability occurs when $l\Omega_1$ or $l\Omega_2$ is close to $\omega_p+\omega_q$, but these instability boundaries can be calculated independently. For $l\Omega_1 = \omega_p+\omega_q+\varepsilon\sigma_1$, the condition separating bounded and unbounded solutions is

$$\Omega_1 = \frac{\omega_p+\omega_q}{l} \pm \frac{2\varepsilon k_{g1}\delta_{1p}\delta_{1q}}{l^2\pi\sqrt{\omega_p\omega_q}}\sin(lc_1\pi)$$
$$\Omega_2 = \frac{\omega_p+\omega_q}{l} \pm \frac{2\varepsilon k_{g2}\delta_{2p}\delta_{2q}}{l^2\pi\sqrt{\omega_p\omega_q}}\sin(lc_2\pi) \qquad (5.13)$$

The stability regions associated with each mesh frequency depend on the individual contact ratios but are independent of mesh phasing as the two mesh excitations are uncoupled. For primary and combination instabilities ($l=1$), maximum regions occur when $c_1 = c_2 = 1.5$ and minimum regions require $c_1 = c_2 = \{1, 2\}$. For secondary instabilities ($l=2$), the maximum and minimum conditions are $c_1 = c_2 = \{1.25, 1.75\}$ and $c_1 = c_2 = \{1, 1.5, 2\}$, respectively. Figure 5.6a shows the instability regions for $R=3/5$. The primary instability associated with $\Omega_2=2\omega_3+\varepsilon\sigma_2$ occurs at $\Omega_1 = R\Omega_2 = R(2\omega_3+\varepsilon\sigma_2)$ in Figure 5.6a.

When $R = m$ or $1/m$ for integer m, the parametric excitations from the two meshes interact. Consider the case with $R=1/m$, where the $l=m$ instabilities caused by Ω_1 overlap with the primary instabilities caused by Ω_2. Considering instability of the p-th mode where $\Omega_1=2\omega_p/m+\varepsilon\sigma_1$ and $\Omega_2=m\Omega_1=2\omega_p+m\varepsilon\sigma_1$, the boundaries have

$$\sigma_1 = [(D_{pp}^{(m)} + F_{pp}^{(1)})^2 + (E_{pp}^{(m)} + G_{pp}^{(1)})^2]^{1/2} / (m\omega_p) \tag{5.14}$$

For example, when $\Omega_2=2\Omega_1$ ($R=1/2$), the boundaries for Ω_1 secondary instabilities (overlapping with Ω_2 primary instabilities) are

$$\Omega_1 = \omega_p \pm \frac{\varepsilon}{2\omega_p}[(D_{pp}^{(2)} + F_{pp}^{(1)})^2 + (E_{pp}^{(2)} + G_{pp}^{(1)})^2]^{1/2} \tag{5.15}$$

Figure 5.6b shows instability regions in the (Ω_1, ε) plane for $R=1/2$. Note the instability at $\Omega_1 \approx \omega_3$ couples with the instability at $\Omega_2 \approx 2\omega_3$, and the combined instability region is much larger than the case without interaction (Figure 5.6a). Using (5.5) and (5.10) in (5.15), the slopes of these boundaries are

$$\sigma_1 = [k_{g1}^2 \delta_{1p}^4 \sin^2(2c_1\pi) + k_{g2}^2 \delta_{2p}^4 \sin^2(c_2\pi) + 2k_{g1}k_{g2}\delta_{1p}^2\delta_{2p}^2 \sin(2c_1\pi)\sin(c_2\pi)\cos(2c_1 - c_2 + 2h)\pi]^{1/2} / \omega_p \quad (5.16)$$

Minimization of σ_1 requires $c_1 = \{1, 1.5, 2\}$ and $c_2 = \{1, 2\}$ for $1 \le c_{1,2} \le 2$. The instability region can also be reduced by adjusting the phasing h according to $\cos(2c_1 - c_2 + 2h)\pi = \pm 1$ with sign the same as $\sin(2c_1\pi)$. The primary instability regions under Ω_1 ($l=1$) do not coincide with any other instability regions. Other overlap situations are possible, such as the Ω_2 secondary instability ($l=2$) overlaps with the Ω_1 fourth instability ($l=4$), but the interaction between these higher instabilities is typically weak and the instablity regions are much smaller. Combination instabilities can be analyzed similarly.

3. Three and Four-gear Systems: Unequal Mesh Stiffness Variations

This general case allows all parameters of the two mesh stiffnesses to differ. In contrast with prior cases, the gears may have differing facewidths and material properties such that the amplitudes of stiffness variation at each mesh vary independently ($\varepsilon_1 \neq \varepsilon_2$). The contact ratios and mesh phasing are unrestricted. The design of one mesh must account for dynamic interactions with the mesh stiffness variation of the other.

When $R \neq m, 1/m$ for integer m, there is no interaction between the parametric excitations from the two meshes. The Ω_1 instabilities are only affected by ε_1 and the Ω_2 instabilities are only affected by ε_2.

When $R = m$ or $1/m$ for integer m, a mode may be simultaneously driven to instability by both mesh excitations. In this case, the first mesh instability regions can be significantly affected by the presence of ε_2 and *vice versa*. Closed-form boundaries of the

form (for primary instability) $\Omega_1 = 2\omega_p+\varepsilon_1\sigma_1+\varepsilon_2\sigma_2$ for independently varying ε_1, ε_2 are cumbersome. Alternatively, simple yet accurate approximations for the instability boundaries are obtained by presuming a linear variation of the boundaries in the (Ω_1, ε_1) plane for given ε_2. To construct this linear approximation, one point is calculated under the condition $\varepsilon_1 = 0, \varepsilon_2 = C$ and a second point is obtained at $\varepsilon_1 = \varepsilon_2 = C$. The primary stability boundary limits for $\varepsilon_1 = 0, \varepsilon_2 = C$ are

$$\Omega_1 = 2\omega_p \pm \frac{C}{\omega_p}[(F_{pp}^{(1)})^2 + (G_{pp}^{(1)})^2]^{1/2} \tag{5.17}$$

From (5.9), the stability boundary limits for $\varepsilon_1 = C, \varepsilon_2 = C$ are

$$\Omega_1 = 2\omega_p \pm \frac{C}{\omega_p}[(D_{pp}^{(1)} + F_{pp}^{(1)})^2 + (E_{pp}^{(1)} + G_{pp}^{(1)})^2]^{1/2} \tag{5.18}$$

An example is for the primary instability when *R=1, C=0.3*. Connecting the two points obtained from (5.17) and (5.18) yields the instability boundaries, which agree well with the numerical solution (Figure 5.7a). Assembling the (Ω_1, ε_1) planes for various $\varepsilon_2=C$ generates three-dimensional plots of Ω_1 versus ε_1, ε_2 (Figure 5.7b). The parametric excitation in the second mesh dramatically changes the shapes of the instability regions. Notice that the second parametric excitation *widens* the primary instability region for small ε_1 compared to mono-frequency excitation (Figure 5.3). In contrast, the combination instability at $\Omega_1 \approx \omega_2 + \omega_3$ disappears near $\varepsilon_1 = 0.23$ in Figure 5.7a. In other words, an otherwise unstable system is stabilized by the presence of a second parametric excitation. The solid line in Figure 5.7b indicates points where the $\omega_2 + \omega_3$ combination instability vanishes.

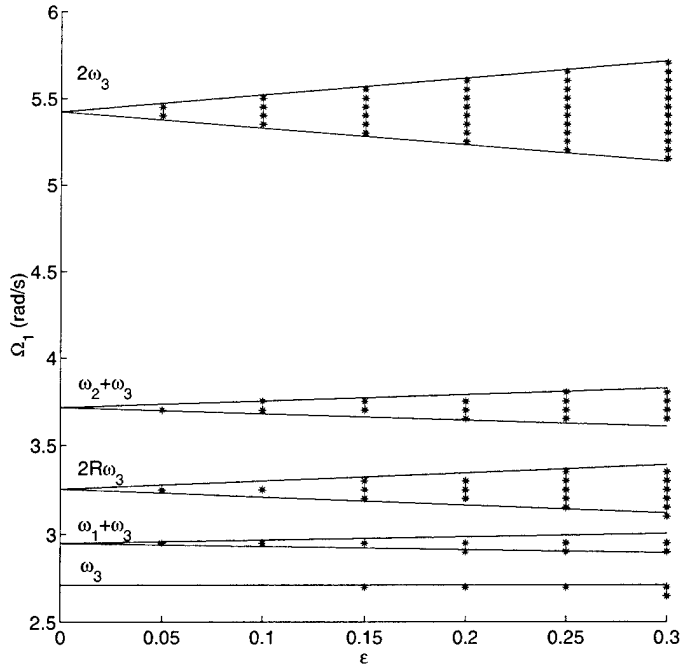

(a)

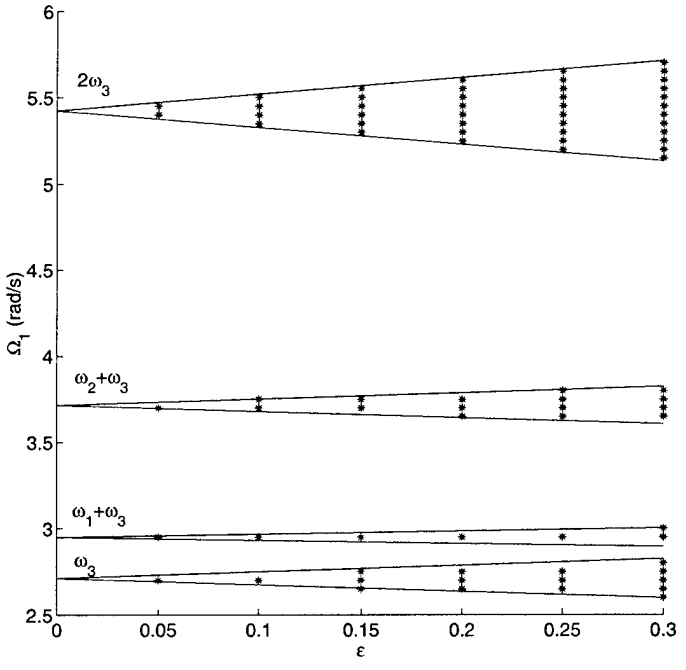

(b)

Figure 5.6 Instabilities regions when $\Omega_1 = R\Omega_2$, $\varepsilon_1 = \varepsilon_2 = \varepsilon$. (a) *R=3/5,* (b) *R=1/2.* The parameters are in Table 5.1 and $c_1 = c_2 = 1.5$, $h = 0$. *** denotes numerical solutions.

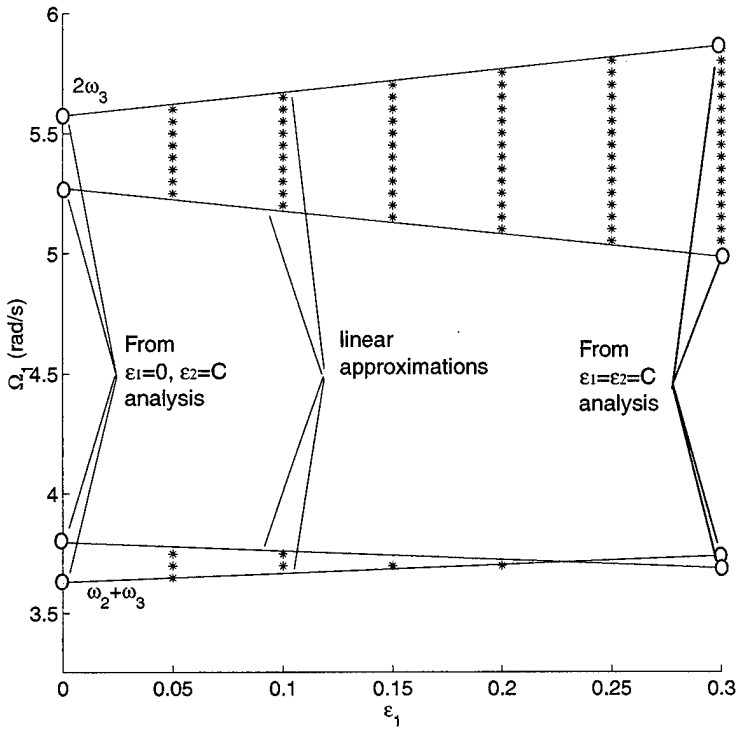

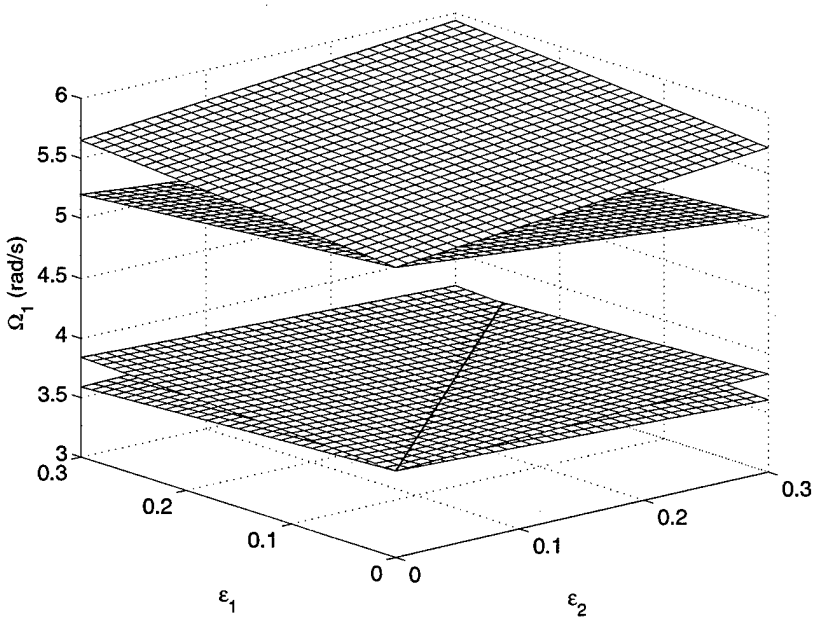

(b)

Figure 5.7 Instabilities regions when $\Omega_1=\Omega_2$. (a) Ω_1 vs. ε_1 and $\varepsilon_2=C=0.3$. (b) Ω_1 vs. ε_1, ε_2 and the solid line indicates vanishing of the combination instability. The parameters are in Table 5.1 and $c_1 = c_2 = 1.5,\ h = 0$.

5.1.3 An Example

The two-stage gear system (Figure 5.1a) studied by Tordion and Gauvin (1977) and Benton and Seireg (1980b) is used as an example. These two papers come to markedly different conclusions as discussed below. The system parameters are given in Table 5.1 and $c_1 = 1.47$, $c_2 = 1.57$. In keeping with the published work, the double-tooth contact mesh stiffness $k_{max}=1$ is kept constant, and the average mesh stiffnesses k_{gi} decrease as k_{ai} is increased (Figure 5.2b).

Tordion and Gauvin assumed that k_{v1} and k_{v2} have the same amplitude and frequency but different contact ratios and phasing. They applied an infinite determinant method (Bolotin, 1964) to plot the boundaries of primary and secondary instabilities (dashed lines in Figure 5.8). Their results deviate significantly from the numerical solution as a result of analytical errors. In addition, the Fourier expansion they derived for rectangular waveforms (equations (11) and (12) in Tordion and Gauvin, 1977) is incorrect. Nevertheless, they conclude that "The phase displacement between the meshing stiffnesses has a great influence on the width of the instability regions."

Benton and Seireg (1980b) considered the same system. They decoupled the equations using the modal transformation and *neglected* the off-diagonal terms of the transformed time-varying stiffness matrix (that is, $\Phi^T \mathbf{K}_v(t)\Phi$). These treatments reduce (5.6) to three *uncoupled* Mathieu equations. The average value of two contact ratios was used to make the stiffness variations k_{v1} and k_{v2} identical. With these approximations, they conclude that the instability regions are independent of the mesh phasing, that is, "the normal mode technique ... without considering the phase variations ... provide(s) a

relatively simple means of predicting the instability regions with sufficient accuracy for practical purposes." This conflicts directly with Tordion and Gauvin. In fact, the mode uncoupling method does not provide satisfactory results when the mesh phasing is non-zero (Figure 5.8b).

The perturbation results resolve the discrepancy: Mesh phasing strongly impacts the mesh stiffness variation instabilities. The excellent agreement of analytical and numerical stability boundaries confirms this finding (Figures 5.3-5.8).

To further validate the stability conditions, free responses under non-trivial initial conditions are calculated numerically (Figure 5.9) for the parameters at point *A* of Figure 5.8 ($\Omega = 4.2$, $k_a=\varepsilon=0.3$). For point *A* in Figure 5.8a, the responses are unstable (Figure 5.9a), as identified by perturbation and numerical methods. This point, however, is stable according to Tordion and Gauvin (Figure 5.8a). When the phasing $h=0.4$ at point *A* (Figure 5.8b), stable responses occur (Figure 5.9b). This is consistent with the perturbation and numerical solutions but conflicts with both Tordion and Gauvin's and Benton and Seireg's results.

5.1.4 Discussion

Rectangular waveforms are close approximations of the mesh stiffness in spur gears with involute teeth. For helical gears or spur gears with tooth modification, mesh stiffness deviates from the rectangular shape. Equation (5.5) is not valid for other functions, but the general Fourier expansion (5.6) can still be used in matrices **D**, **E**, **F**, **G** to determine the instability boundaries.

If damping is considered, the system stability improves and the instability regions shift to the right in the (Ω, ε) plane. Furthermore, damping and non-linearity (*e.g.*, tooth separation) must be considered to determine the limit cycle amplitude of the dynamic response when operating conditions cause instability.

The instability analysis can be reduced to single mesh gears with one natural frequency ω_n. From (5.9), primary and secondary instabilities vanish as the contact ratio $c_1=\{1,2\}$ and $c_1=\{1, 1.5, 2\}$, respectively. Maximum primary and secondary instability occurs at $c_1=1.5$ and $c_1=\{1.25, 1.75\}$, respectively. Kahraman and Blankenship (1999) experimentally studied a pair of spur gears under mesh stiffness excitation for various contact ratios. They showed that the amplitude A_1 in the first mesh frequency harmonic of the response is minimized when the contact ratio $c_1=\{1.0, 2.0\}$. This is because parametric excitations are eliminated for integer contact ratios. When the mesh frequency $\Omega\approx\omega_n$, their measured A_1 reaches maximum for $c_1\approx1.4$. A possible explanation for the high A_1 at this contact ratio is due to the combined effects of primary and secondary instabilities. First, for both primary instability excited by the first harmonic of $k(t)$ and secondary instability excited by the second harmonic of $k(t)$, the dominant response frequency is ω_n. We now examine the contact ratios where both instabilities are active. Although the maximum primary instability region occurs at $c_1=1.5$, the secondary instability region is eliminated there. For $c_1=1.25$, the secondary instability region is maximal but the primary instability region is small. For $c_1\approx1.4$ (average of *1.25* and *1.5*) or *1.6* (average of *1.75* and *1.5*), however, both primary and secondary instabilities have significant instability regions. Generally, the larger an instability region, the higher

response amplitude occurs due to this instability (to see this heuristically, note that both the slope of the stability boundaries in (17) and excitation of first order response in (10) are proportional to the same quantities **D**, **E**, **F**, and **G**). Accordingly, for $c_1 \approx 1.4$ and 1.6, both instabilities induce large response and jointly contribute to large A_1. When the mesh frequency $\Omega \approx 2\omega_n$ (not shown in Kahraman and Blankenship, 1999), the instability is caused only by primary instability excited by the first harmonic of $k(t)$. Because the primary instability region is maximal at $c_1 = 1.5$, the response amplitude A_1 around $\Omega \approx 2\omega_n$ also becomes maximal. Therefore, from the viewpoint of dynamic instability and amplitude, contact ratios in the range 1.4~1.6 are harmful to single-mesh gears at high speeds.

5.2 Planetary Gear Parametric Instability

Planetary gears have multiple time-varying mesh stiffnesses and their parametric instability has not been analytically investigated. In planetary gears, parametric excitations are complicated as different contact ratios and phasing conditions exist between the sun-planet and the ring-planet meshes. The objective of this study is to analyze parametric instability excited by different time-varying mesh stiffnesses in planetary gears. The perturbation method used for two-stage gears is extended to planetary gears that have degenerate vibration modes due to their cyclic symmetry. The well-defined modal properties of planetary gears are used to derive simple expressions for instability boundaries separating the stable and unstable regions. From these expressions, the effects of contact ratios and mesh phasing are analytically determined to

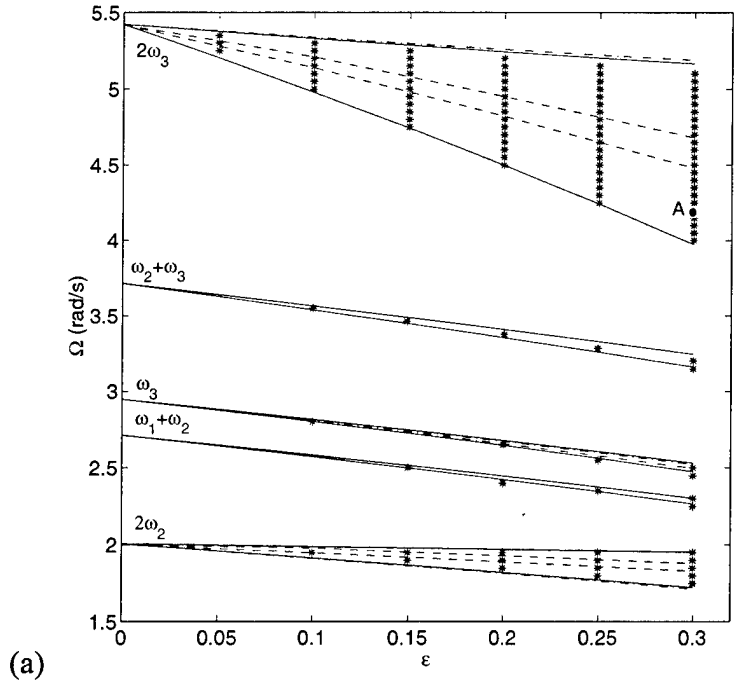

(a)

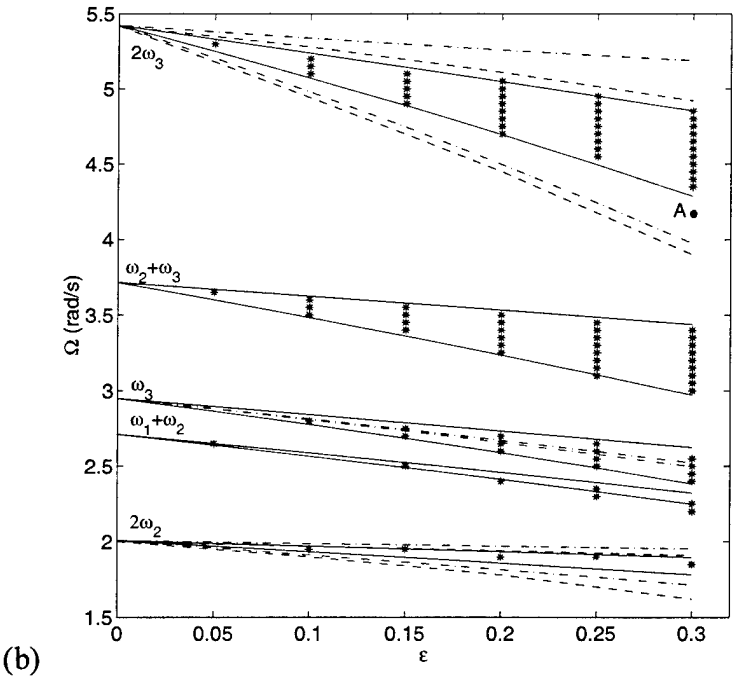

(b)

Figure 5.8 Comparison of instability regions. The parameters are from Table 5.1, $c_1 = 1.47$, $c_2 = 1.57$, and phasing (a) *h=0*, (b) *h=0.4*. — Perturbation method; *** Numerical method; --- Tordion and Gauvin (1977); ·-·-· Benton and Seireg (1980b).

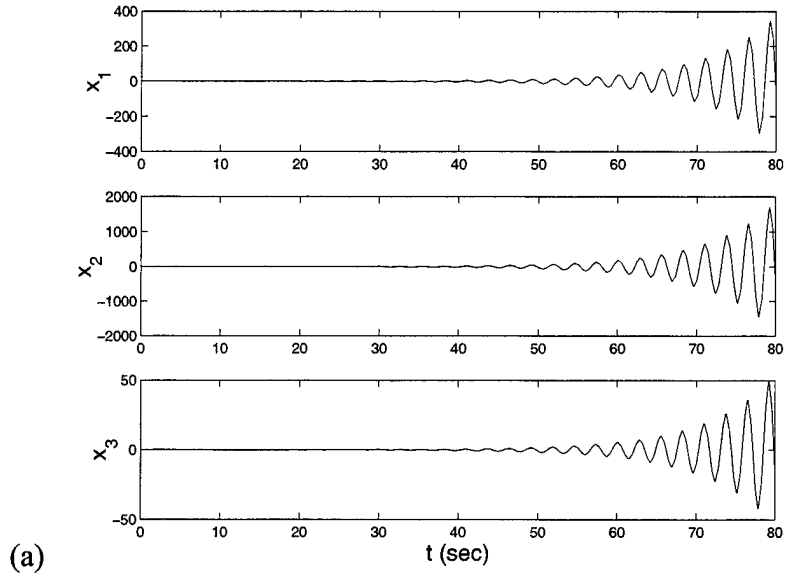

(a)

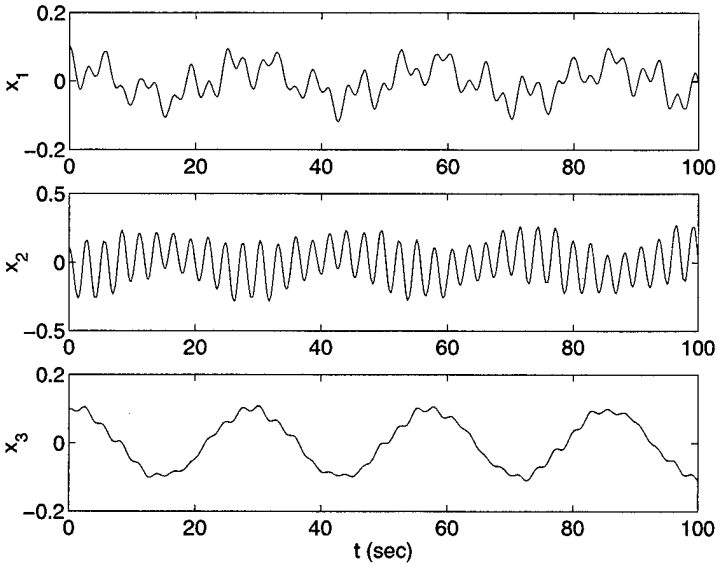

(b)

Figure 5.9 Free responses for $\Omega = 4.2$, $k_a=\varepsilon=0.3$ (point A in Figure 5.8) and the parameters of (a) Figure 5.8a and (b) Figure 5.8b. The initial conditions are $x_1 = x_2 = x_3 = 0.1$, $\dot{x}_1 = \dot{x}_2 = \dot{x}_3 = 0$.

provide insight into planetary gear design. In practice, planet mesh-phasing schemes are often applied to cancel or neutralize resonant response at speeds where the mesh frequency is near a natural frequency (Seager, 1975; Kahraman, 1994b; Kahraman and Blankenship, 1994; Parker, 2000). In this same spirit, this study shows that particular parametric instabilities can be eliminated under certain phasing conditions that can be achieved by proper selection of design parameters. Tooth separation nonlinearity induced by parametric instability is numerically simulated.

5.2.1 System Model and Mode Properties

The planetary gear dynamic model used is based on the one developed in Chapter 2 (Figure 2.2). Translational degrees of freedom in that model are eliminated, and only rotational motions of the gear bodies are considered. The sun-planet and ring-planet tooth meshes are modeled as linear springs with time-varying stiffnesses $k_{sn}(t)$, $k_{rn}(t)$, $n=1,...N$. The system equations of motion are

$$\mathbf{M}\ddot{\mathbf{q}} + \mathbf{K}(t)\mathbf{q} = \mathbf{F} \tag{5.19}$$

$$\mathbf{M} = diag\left[I_c / r_c^2 + \sum m_p,\ I_r / r_r^2,\ I_s / r_s^2,\ I_p / r_p^2,\ \cdots,\ I_p / r_p^2\right]$$

$$\mathbf{K}(t) = \begin{bmatrix} \sum(k_{sn}+k_{rn}) & -\sum k_{rn} & -\sum k_{sn} & k_{r1}-k_{s1} & \cdots & k_{rN}-k_{sN} \\ & \sum k_{rn} & 0 & -k_{r1} & \cdots & -k_{rN} \\ & & \sum k_{sn} & k_{s1} & \cdots & k_{sN} \\ & & & k_{r1}+k_{s1} & 0 & \cdots & 0 \\ & & & & \ddots & \ddots & \vdots \\ & & & & & \ddots & 0 \\ \text{symmetric} & & & & & & k_{rN}+k_{sN} \end{bmatrix} \tag{5.20}$$

$$\mathbf{q} = [u_c, u_r, u_s, u_1, \cdots, u_N]^T, \qquad \mathbf{F} = [T_c/r_c,\ T_r/r_r,\ T_s/r_s,\ 0, \cdots, 0]^T$$

where the summation index n ranges from *1* to N. In the stiffness matrix $\mathbf{K}(t)$, each mesh stiffness is represented by $k_{sn}(t) = k_{sp} + k_{1n}(t)$, $k_{rn}(t) = k_{rp} + k_{2n}(t)$, $n=1,...N$, where k_{sp}, k_{rp} are mean values and k_{1n}, k_{2n} are time-varying components of the n-th sun-planet and ring-planet meshes. For spur gears, rectangular waves are often used to approximate mesh stiffnesses alternating between d and $d+1$ pairs of teeth in contact. Figure 5.10 shows the mesh stiffness variations k_{1n}, k_{2n} with peak-to-peak amplitudes $2k_{vs}$, $2k_{vr}$, contact ratios c_s, c_r, and phasing angles $\gamma_{sn}T$, $(\gamma_{sr}+\gamma_{rn})T$. The sun-planet and ring-planet meshes have the identical mesh frequency $\Omega=2\pi/T$. The sun-planet mesh stiffnesses between planets differ only by a time transition (or phase angle), and likewise for the ring-planet meshes. Mesh phasing in planetary gears is determined by planet position angles ψ_n and the numbers of teeth z_s, z_r, z_p for the sun, ring, and planets (Kahraman and Blankenship, 1994). $\gamma_{sn}=\psi_n z_s/(2\pi)$ denotes the mesh phasing between the first and n-th sun-planet meshes ($\gamma_{s1}=0$); $\gamma_{rn}=\psi_n z_r/(2\pi)$ is the mesh phasing between the first and n-th ring-planet meshes ($\gamma_{r1}=0$); $\gamma_{sr}=z_p/2$ is the mesh phasing between the sun-planet and ring-planet meshes for each planet. Note $\gamma_{sr}=0$ for even z_p and $\gamma_{sr}=1/2$ for odd z_p. Expansion of k_{1n}, k_{2n} in Fourier series yields

$$\begin{aligned} k_{1n}(t) &= 2k_{vs}\sum_{l=1}^{\infty}(a_{sn}^{(l)}\sin l\Omega t + b_{sn}^{(l)}\cos l\Omega t), \\ k_{2n}(t) &= 2k_{vr}\sum_{l=1}^{\infty}(a_{rn}^{(l)}\sin l\Omega t + b_{rn}^{(l)}\cos l\Omega t) \end{aligned} \tag{5.21}$$

$$a_{sn}^{(l)} = -\frac{2}{l\pi}\sin[l\pi(c_s - 2\gamma_{sn})]\sin(l\pi c_s), \qquad a_{rn}^{(l)} = -\frac{2}{l\pi}\sin[l\pi(c_r - 2\gamma_{sr} - 2\gamma_{rn})]\sin(l\pi c_r)$$

$$b_{sn}^{(l)} = -\frac{2}{l\pi}\cos[l\pi(c_s - 2\gamma_{sn})]\sin(l\pi c_s), \qquad b_{rn}^{(l)} = -\frac{2}{l\pi}\cos[l\pi(c_r - 2\gamma_{sr} - 2\gamma_{rn})]\sin(l\pi c_r)$$

Mesh stiffnesses depend on many parameters including the number of teeth in contact, gear facewidth, material properties, profile modifications, and applied load (Kasuba and Evans, 1981). Let $\varepsilon_1 = k_{vs}/k_{sp}$ and $\varepsilon_2 = k_{vr}/k_{rp}$ be the relative amplitudes of mesh stiffness variation. In the simplest approximation, mesh stiffnesses are assumed proportional to the number of tooth pairs in contact, that is, $k_{sp}=c_s\, k_{1t}$, $k_{rp}=c_r\, k_{2t}$ and $k_{vs}= k_{1t}/2$, $k_{vr}= k_{2t}/2$, where k_{1t}, k_{2t} are one-pair tooth bending stiffnesses of the sun-planet and ring-planet meshes. With this simplifying assumption, the nominal amplitudes of stiffness variations are $\varepsilon_1=1/(2c_s)$, $\varepsilon_2=1/(2c_r)$, and one obtains the explicit relation $\varepsilon_2=\varepsilon_1\, c_s/c_r$. In practice and in the analysis that follows, however, ε_1 and ε_2 are not constrained to these "nominal" values but vary independently of the contact ratios to account for the many factors influencing mesh stiffness variation amplitudes. For this modeling, we let $\varepsilon_1=\varepsilon_2/g=\varepsilon$ where $g=O(1)$ (and $g=c_s/c_r$ under the simplifying assumption noted above). Substitution of (5.4) and (5.21) into (5.20) yields

$$\mathbf{K}(t) = \mathbf{K}_0 + 2\varepsilon\sum_{l=1}^{\infty}(\mathbf{K}_{v1}^{(l)}\sin l\Omega t + \mathbf{K}_{v2}^{(l)}\cos l\Omega t) \tag{5.22}$$

where the average stiffness matrix $\mathbf{K}_0$ has the same form as (5.20) with k_{sn}, k_{rn} substituted by k_{sp}, k_{rp}. The Fourier coefficient matrices are also in the form (5.20) with k_{sn}, k_{rn} substituted by $k_{sp}a_{sn}^{(l)}$, $gk_{rp}a_{rn}^{(l)}$ for $\mathbf{K}_{v1}^{(l)}$ and substituted by $k_{sp}b_{sn}^{(l)}$, $gk_{rp}b_{rn}^{(l)}$ for $\mathbf{K}_{v2}^{(l)}$.

For the time-invariant case, the eigenvalue problem associated with (5.19) is

$$\mathbf{K}_0\phi_i = \omega_i^2\mathbf{M}\phi_i \tag{5.23}$$

The natural frequencies and vibration modes have unique properties (3.7), (3.14), (3.20). We specialize these properties for the case of a rotational vibration model with fixed ring and $L=N+2$ degrees of freedom. In this case, all vibration modes can be classified into one of three categories: (1) a rigid body mode ($\omega_1=0$), (2) two modes with distinct natural frequencies (ω_2, ω_L), and (3) a group of degenerate modes with multiplicity $N-1$ ($\omega_3=\ldots=\omega_{N+1}$). In the distinct modes, all planets have identical motion

$$u_n = u_1, \qquad n=1,2,\ldots,N \tag{5.24}$$

In the degenerate modes, the carrier, ring, and sun have no motion, and the planet rotations satisfy

$$u_n = [u_1\sin(\psi_2-\psi_n)+u_2\sin\psi_n]/\sin\psi_2, \qquad n=1,2,\ldots,N \tag{5.25}$$

These well-defined properties are valid not only for equally spaced planets with position angles $\psi_n = 2\pi(n-1)/N$, but also for diametrically opposed planets with $\psi_{n+N/2} = \psi_n + \pi$.

5.2.2General Expression for Instability Boundaries

We determine the operating conditions (that is, mesh frequency Ω and stiffness variation amplitude ε) that lead to instability when $l\Omega\approx\omega_p+\omega_q$ for integer l. The rigid body mode ($\omega_1=0$) is not excited under operating conditions, and does not affect the instabilities of other modes. Only the two distinct modes and the group of degenerate modes are considered in what follows. The parametric instability when $l\Omega$ is close to $\omega_p+\omega_q$ is considered. Let $l\Omega = \omega_p + \omega_q + \varepsilon\sigma$, where σ is a detuning parameter to be determined. From (5.8), when ω_p and ω_q are both distinct, the instability boundaries are

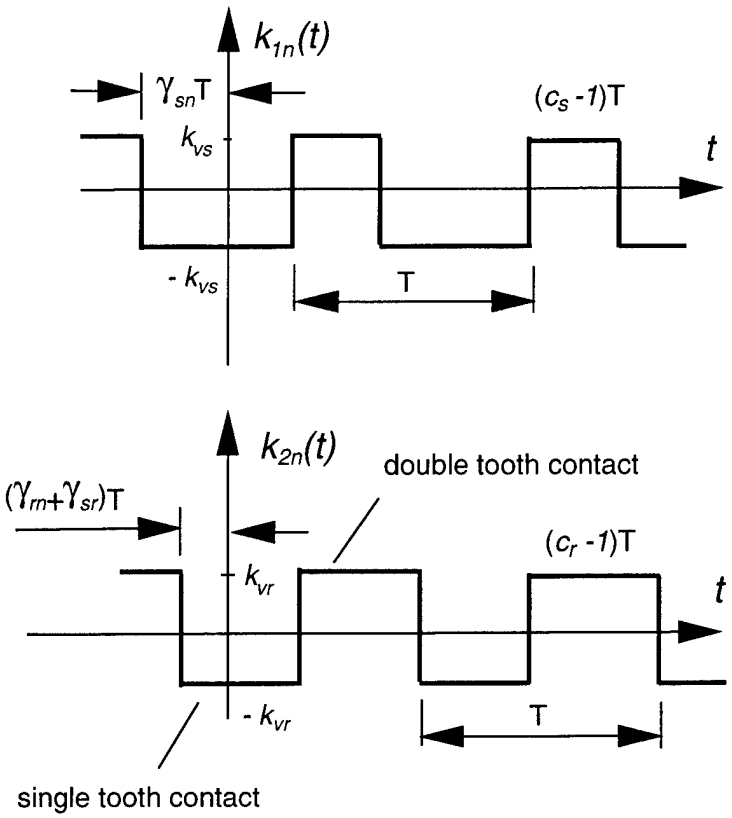

Figure 5.10 Modeling of mesh stiffness variations in the sun-planet and ring-planet meshes. c_s, c_r are contact ratios, and γ_{sn}, γ_{rn}, γ_{sr} are mesh phasing.

$$\text{single mode instability: } \Omega = \frac{2\omega_p}{l} \pm \frac{\varepsilon}{l\omega_p}\sqrt{\Lambda_{pp}^{(l)}} \tag{5.26}$$

$$\text{combination instability: } \Omega = \frac{\omega_p + \omega_q}{l} \pm \frac{\varepsilon}{l}\sqrt{\Lambda_{pq}^{(l)}/(\omega_p\omega_q)} \tag{5.27}$$

where $\Lambda_{pq}^{(l)} = (D_{pq}^{(l)})^2 + (E_{pq}^{(l)})^2$.

When ω_p or ω_q are degenerate, the complexity of instability solutions depends on the multiplicity of the degenerate natural frequencies. We first study the case with multiplicity two, say $\omega_p=\omega_q$. The single-mode instability boundaries for $\omega_p=\omega_q$ are (Lin and Parker, 2000d)

$$\Omega = \frac{2\omega_p}{l} \pm \frac{\varepsilon}{l\omega_p}\sqrt{\Gamma^{(l)}},$$

$$\Gamma^{(l)} = D_{pq}^{(l)} D_{qp}^{(l)} + E_{pq}^{(l)} E_{qp}^{(l)} + \frac{1}{2}[(D_{pp}^{(l)})^2 + (D_{qq}^{(l)})^2 + (E_{pp}^{(l)})^2 + (E_{qq}^{(l)})^2] \tag{5.28}$$

When $\omega_p=\omega_q$ are degenerate but ω_r is distinct, the combination instability is

$$\Omega = \frac{\omega_p + \omega_r}{l} \pm \frac{\varepsilon}{l}[(D_{pr}^{(l)} D_{rp}^{(l)} + D_{qr}^{(l)} D_{rq}^{(l)} + E_{pr}^{(l)} E_{rp}^{(l)} + E_{qr}^{(l)} E_{rq}^{(l)})/(\omega_p \omega_r)]^{1/2} \tag{5.29}$$

When the degenerate natural frequencies $\omega_3=\ldots=\omega_{m+2}$ have multiplicity $m > 2$, the critical σ is obtained by requiring the real parts of the eigenvalues of the following matrix to be non-positive,

$$\begin{bmatrix} \mathbf{E}_{sub}^{(l)} & \mathbf{D}_{sub}^{(l)} - (\sigma\omega_3)\mathbf{I}_{m\times m} \\ \mathbf{D}_{sub}^{(l)} + (\sigma\omega_3)\mathbf{I}_{m\times m} & -\mathbf{E}_{sub}^{(l)} \end{bmatrix} \tag{5.30}$$

where $\mathbf{D}_{sub}^{(l)}, \mathbf{E}_{sub}^{(l)}$ are $m\times m$ submatrices of $\mathbf{D}^{(l)}$, $\mathbf{E}^{(l)}$ including rows and columns *3, ..., m+2*. Generally, no closed-form solution can be derived for these single-mode instabilities, but numerical evaluation can determine σ and the instability boundaries unless $\mathbf{D}_{sub}^{(l)}, \mathbf{E}_{sub}^{(l)}$ have special features (*e.g.,* diagonal matrices) as discussed later. More is possible for combination instabilities. For combination instability of distinct ω_r and degenerate $\omega_3=\ldots=\omega_{m+2}$, the instability boundaries are

$$\Omega = \frac{\omega_3 + \omega_r}{l} \pm \frac{\varepsilon}{l}\sum_{q=3}^{m+2}\sqrt{(D_{qr}^{(l)} D_{rq}^{(l)} + E_{qr}^{(l)} E_{rq}^{(l)})/(\omega_r \omega_3)} \tag{5.31}$$

The above expressions apply for a general system with degenerate natural frequencies. These results reduce to simple forms when specialized to planetary gears.

5.2.3. Planetary Gear Parametric Instability

Planetary gears' well-defined modal properties are now used to simplify the above instability conditions to compact expressions suitable for use in applications. Mesh stiffness are approximated by rectangular waveforms (5.21). Expansion of $\mathbf{D}^{(l)}$, $\mathbf{E}^{(l)}$ gives

$$\begin{aligned} D_{pq}^{(l)} &= \phi_p^T \mathbf{K}_{v1}^{(l)} \phi_q = k_{sp} \sum_{n=1}^{N} a_{sn}^{(l)} \delta_{sn}^{(p)} \delta_{sn}^{(q)} + k_{rp} g \sum_{n=1}^{N} a_m^{(l)} \delta_m^{(p)} \delta_m^{(q)} \\ E_{pq}^{(l)} &= \phi_p^T \mathbf{K}_{v2}^{(l)} \phi_q = k_{sp} \sum_{n=1}^{N} b_{sn}^{(l)} \delta_{sn}^{(p)} \delta_{sn}^{(q)} + k_{rp} g \sum_{n=1}^{N} b_m^{(l)} \delta_m^{(p)} \delta_m^{(q)} \end{aligned} \tag{5.32}$$

where $\delta_{sn}^{(p)} = u_s - u_c + u_n$ is the deformation of the n-th sun-planet mesh in mode ϕ_p and $\delta_m^{(p)} = -u_c - u_n$ is the deformation of the n-th ring-planet mesh. For different spacing and phasing of planets, matrices $\mathbf{D}^{(l)}$, $\mathbf{E}^{(l)}$ have special features that simplify the instability conditions.

1. Equally spaced planets

For equally spaced planets ($\psi_n = 2\pi(n-1)/N$), the vibration modes have structured properties (5.24) and (5.25). In this case, $(z_s+z_r)/N$ = integer and the planet meshes have phasing $\gamma_{sn}=(n-1)z_s/N$ and $\gamma_{rn}=(n-1)z_r/N$, $n=1,...,N$. The two possible phasing conditions are examined below.

(1) In-phase Planet Meshes

Consider the case when all the sun-planet meshes are in-phase ($\gamma_{sn}=0$, $n=1,...,N$) and all the ring-planet meshes are in-phase ($\gamma_{rn}=0$, $n=1,...,N$). This design is typical when optimizing load sharing and results when z_s and z_r are each integer multiples of N. However, there is a constant phasing $\gamma_{sr}=0$ (even z_p) or $1/2$ (odd z_p) between the sun-

planet and ring-planet meshes for each planet. The Fourier coefficients $a_{sn}^{(l)}, a_{rn}^{(l)}, b_{sn}^{(l)}, b_{rn}^{(l)}$ in (5.21) are independent of the planet index n.

For a distinct natural frequency ω_p, vibration mode property (5.24) leads to $\delta_{sn}^{(p)} = \delta_{s1}^{(p)}$, $\delta_{rn}^{(p)} = \delta_{r1}^{(p)}$ for any planet n. Using (5.21) and (5.32) on (5.26), the primary instability boundaries have

$$\Lambda_{pp}^{(1)} = (\frac{2N}{\pi})^2[(\delta_{s1}^{(p)})^4(k_{sp}\sin\pi c_s)^2 + (\delta_{r1}^{(p)})^4(k_{rp}g\sin\pi c_r)^2 + 2\,k_{sp}k_{rp}g(\delta_{s1}^{(p)}\delta_{r1}^{(p)})^2\sin(\pi c_s)\sin(\pi c_r)\cos\pi(c_s - c_r + 2\gamma_{sr})] \tag{5.33}$$

Obviously, $\Lambda_{pp}^{(1)} = 0$ when c_s, c_r are integers and all instabilities vanish. If c_s, $c_r \neq$ integer, a second choice to reduce the instability regions is to set the third term in (5.33) to be negative by adjusting c_s, c_r, and γ_{sr}. From (5.27), the combination instability boundaries for two distinct modes have

$$\Lambda_{pq}^{(1)} = (\frac{2N}{\pi})^2[(k_{sp}\delta_{s1}^{(p)}\delta_{s1}^{(q)}\sin\pi c_s)^2 + (k_{rp}g\delta_{r1}^{(p)}\delta_{r1}^{(q)}\sin\pi c_r)^2 + 2\,k_{sp}k_{rp}g\delta_{s1}^{(p)}\delta_{s1}^{(q)}\delta_{r1}^{(p)}\delta_{r1}^{(q)}\sin(\pi c_s)\sin(\pi c_r)\cos\pi(c_s - c_r + 2\gamma_{sr})] \tag{5.34}$$

Inertias (kg)	$I_c/r_c^2=6$, $I_s/r_s^2=2.5$, $I_p/r_p^2=2$
Planet mass (kg)	$m_p=4$
Mesh stiffness (N/m)	$k_{sp}= k_{rp}=10^8$
Natural frequencies (kHz)	$\omega_1=0$, $\omega_2=1.212$, $\omega_3=\omega_4=1.592$, $\omega_5=2.196$

Table 5.2 Parameters and natural frequencies of an example planetary gear with fixed ring and three planets.

For the degenerate natural frequencies $\omega_3=...=\omega_{N+1}$, the single-mode instability boundaries are the same as (5.28) with

$$\Gamma^{(l)} = (D_{pp}^{(l)})^2 + (E_{pp}^{(l)})^2 = (\frac{2\Delta}{l\pi})^2[(k_{sp}\sin l\pi c_s)^2 + (k_{rp}g\sin l\pi c_r)^2 + 2k_{sp}k_{rp}g\sin(l\pi c_s)\sin(l\pi c_r)\cos l\pi(c_s - c_r + 2\gamma_{sr})] \quad (5.35)$$

Equation (5.35) applies to any number of planets N.

For the combination instability of degenerate $\omega_3=...=\omega_{N+1}$ and distinct ω_1, the combination instabilities ($l=1$) of a distinct mode and a degenerate mode *always* vanish for any N when the planet meshes are in-phase. A more general condition for vanishing of these combination instabilities is that each of $(lz_s\pm1)/N$, $(lz_r\pm1)/N \neq$ integer.

As an example, Figure 5.11 shows the instability boundaries for a planetary gear with three equally spaced planets. The parameters and nominal natural frequencies are given in Table 5.2 and the vibration modes are shown in Figure 5.12. The mesh phasing is $\gamma_{sn}=\gamma_{rn}=0$, $\gamma_{sr}=1/2$ and the contact ratios are $c_s=1.4$, $c_r=1.6$. We specify $\varepsilon_1=\varepsilon_2=\varepsilon$ (that is, $g=1$). The natural frequencies change as ε varies because the average mesh stiffnesses depend on the amplitude of the mesh stiffness variation. The analytical solutions (solid lines) from (5.26), (5.27), (5.28), and (5.29) agree well with the numerical solutions using Floquet theory and numerical integration. Note the combination instabilities at $\omega_2+\omega_3$, $\omega_3+\omega_5$ vanish because they involve the distinct (ω_2, ω_5) and degenerate ($\omega_3=\omega_4$) natural frequencies. Figure 5.13a shows the primary instability regions for different contact ratios c_s, c_r; the stiffness variation amplitude $\varepsilon=0.3$ and phasing $\gamma_{sr}=0$. All instabilities vanish when the contact ratios are integers. The size of the $2\omega_2$ instability region is primarily affected by c_r while insensitive to changes in c_s. This is because the dominant

deformation of mode ϕ_2 occurs in the ring-planet meshes (Figure 5.12). The $2\omega_5$ instability region is mostly affected by c_s because most deformation occurs in the sun-planet meshes for this mode. The primary instability of the degenerate modes at $2\omega_3=2\omega_4$ is influenced by both c_s and c_r. The primary instability regions are maximized for $c_s=c_r=1.5$, which is expected from (5.33) and (5.35). The relative phasing γ_{sr} between the sun-planet and ring-planet meshes can have a major impact. When the phasing $\gamma_{sr}=1/2$ and other parameters are the same as in Figure 5.13a, the $2\omega_3=2\omega_4$ instability vanishes for any $c_s=c_r$ (Figure 5.13b). This is because $\Gamma^{(l)}=0$ in (5.35) for $k_{sp}=k_{rp}$, $g=1$ and $c_s=c_r$.

The above analyses show that contact ratios and mesh phasing significantly affect the operating condition instability regions. In practice, particular instabilities can be minimized by proper selection of contact ratios and mesh phasing, which are adjusted by center distance, diametral pitch, pressure angle, tooth addendum, numbers of teeth, and other parameters.

(2) Sequentially Phased Planet Meshes

Here we consider equally spaced planet systems where the sun-planet and ring-planet meshes are sequentially phased with $\gamma_{sn}=(n-1)z_s/N$ and $\gamma_{rn}=(n-1)z_r/N$. This case corresponds to z_s/N, $z_r/N\neq$ integer but $(z_s+z_r)/N$=integer. A constant phasing γ_{sr} exists between the sun-planet and ring-planet meshes for each planet. For the sequential phasing, the Fourier coefficients in (5.21) satisfy

$$\sum_{n=1}^{N} a_{sn}^{(l)} = \sum_{n=1}^{N} a_{rn}^{(l)} = \sum_{n=1}^{N} b_{sn}^{(l)} = \sum_{n=1}^{N} b_{rn}^{(l)} = 0 \tag{5.36}$$

when lz_s/N, lz_r/N are non-integer.

For distinct natural frequencies ω_p, the primary instabilities ($l=1$) of distinct modes *always* vanish when the planets are sequentially phased. Physically, it means that these instabilities are not excited because the resultant modal excitations from the sun-planet and ring-planet meshes each are zero. The secondary instabilities ($l=2$) of distinct modes also vanish when $2z_s/N$, $2z_r/N$ are non-integer. Similarly, combination instabilities ($l=1$) of distinct ω_p and ω_q, $D_{pp}^{(1)} = E_{pp}^{(1)} = 0$ *always* vanish in this case.

For instabilities involving the degenerate modes, it is difficult to obtain simple expressions for the instability boundaries; their instability conditions can be calculated from (5.28), (5.30), and (5.31). A special case is the combination instability ($l=1$) of degenerate $\omega_3=\ldots=\omega_{N+1}$ and distinct ω_1 when $(z_s\pm1)/N$, $(z_r\pm1)/N$ each is non-integer. In this case, the combination instabilities of distinct and degenerate modes vanish.

Figure 5.14 shows the instability boundaries for the same system as in Figure 5.11, except the three planets are sequentially phased with γ_{sn}=[*0, 1/3, 2/3*], γ_{rn}=[*0, 2/3, 1/3*]. Note the primary, secondary, and combination instability regions vanish for the distinct natural frequencies ω_2, ω_5; only instabilities involving at least one of the degenerate modes $\omega_3=\omega_4$ exist.

The foregoing results for equally spaced planets are summarized in Table 5.3.

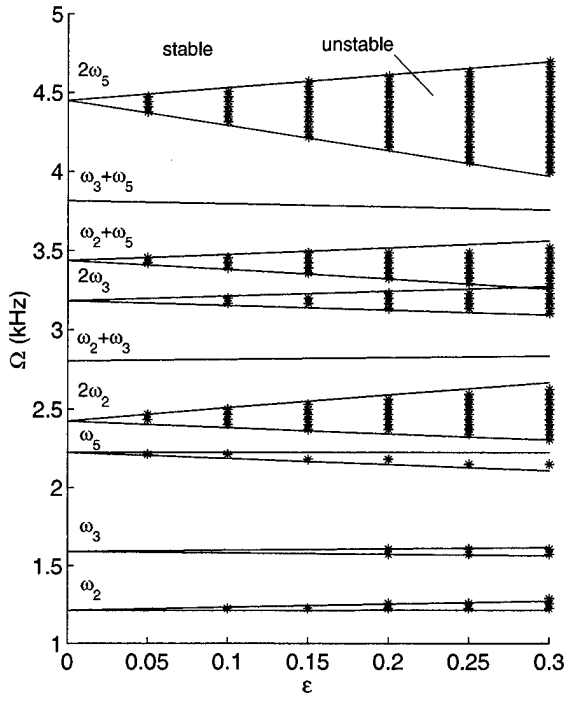

Figure 5.11 Instability regions for the system in Table 5.2 and in-phase meshes $\gamma_{sn}=\gamma_{rn}=0$, $\gamma_{sr}=1/2$. $c_s=1.4$, $c_r=1.6$, $\varepsilon=\varepsilon_1=\varepsilon_2$ $(g=1)$. — analytical solution; *** numerical solution.

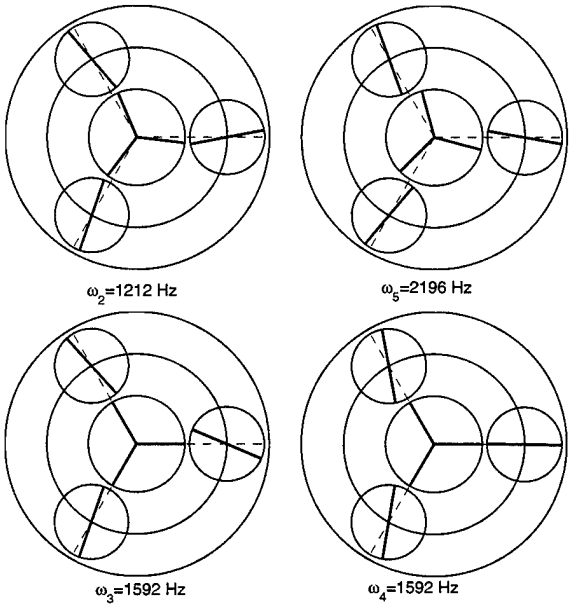

Figure 5.12 Mode shapes of the system in Table 5.2. The carrier motion is not shown.

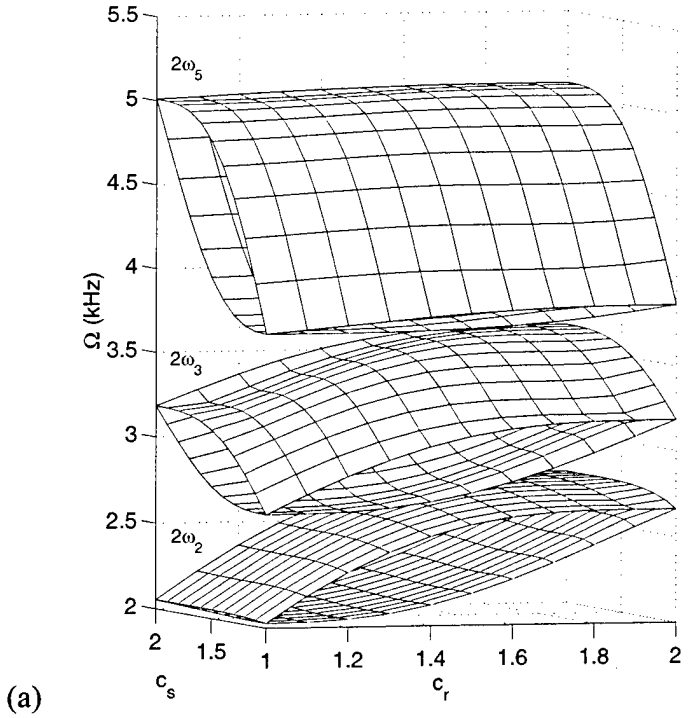

(a)

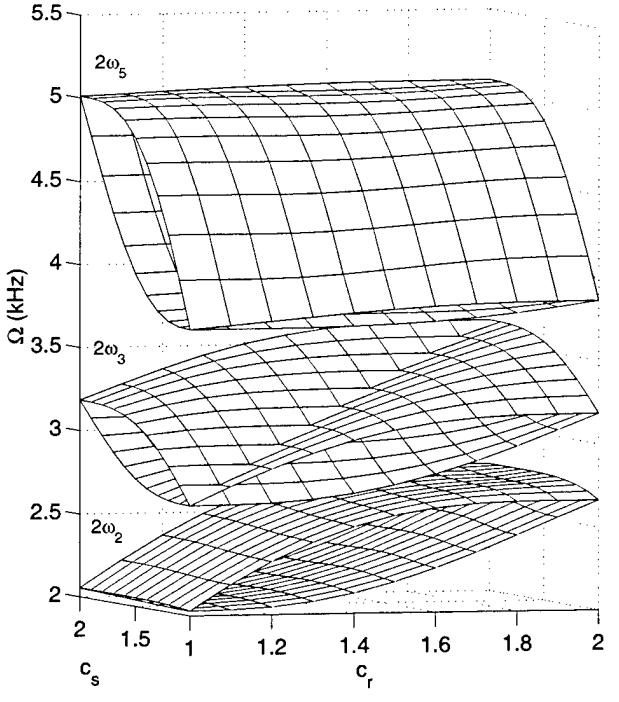

(b)

Figure 5.13 Instability regions of the system in Table 5.2 for different contact ratios. $\varepsilon=\varepsilon_1=\varepsilon_2=0.3$ $(g=1)$. The planets are equally spaced with in-phase meshes ($\gamma_{sn}=\gamma_{rn}=0$). (a) $\gamma_{sr}=0$, (b) $\gamma_{sr}=1/2$.

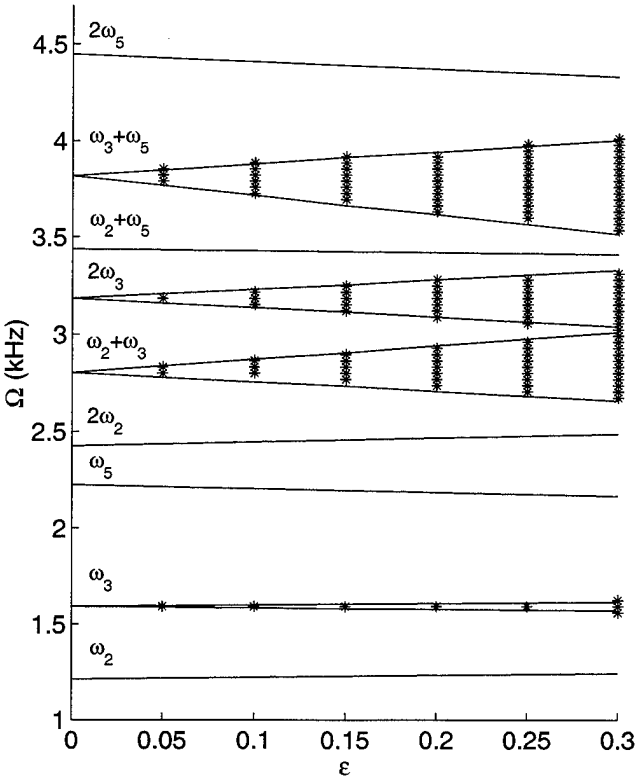

Figure 5.14 Instability regions for the three-planet system in Table 5.2 and sequentially phased planet meshes with γ_{sn}=[*0, 1/3, 2/3*], γ_{rn}=[*0, 2/3, 1/3*]. c_s=*1.4*, c_r=*1.6*, $\varepsilon=\varepsilon_1=\varepsilon_2$ *(g=1)*, γ_{sr}=*1/2*. — analytical solution; *** numerical solution.

Planet Mesh Phasing	Single-Mode Instabilities		Combination Instabilities	
	Distinct Mode	Degenerate Mode	Distinct + Distinct Mode	Degenerate + Distinct Mode
In-phase $\frac{z_s}{N}, \frac{z_r}{N}$ = integer	from (5.26)	from (5.28), (5.30)	from (5.27)	always vanish
Sequentially phased $\frac{z_s}{N}, \frac{z_r}{N} \neq$ integer	primary always vanish; secondary from (5.26) and vanish if $2z_s/N$, $2z_r/N \neq$ integer	from (5.28), (5.30)	always vanish	from (5.31) and vanish if $(z_s \pm 1)/N$, $(z_r \pm 1)/N \neq$ integer

Table 5.3 Instability boundary solutions when the planets are equally spaced (satisfying $(z_s+z_r)/N$ = integer).

2. Unequally spaced planets

When the planets are arbitrarily spaced, the structured modal properties do not exist and the general expressions for instability boundaries cannot be further simplified. For the practically important case of diametrically opposed planets, however, the vibration modes retain the well-defined properties (5.24) and (5.25). The following discussion focuses on this case for *N/2* pairs of diametrically opposed planets. For the sun-planet meshes, each pair of diametrically opposed planets are in-phase ($\gamma_{s(n+N/2)} = \gamma_{sn}$) for even z_s and are counter-phased ($\gamma_{s(n+N/2)} = \gamma_{sn} + 1/2$) for odd z_s. Analogous rule applies for the ring-planet mesh phasing. Note that adjacent planets have arbitrary mesh phasing $\gamma_{sn} = \psi_n z_r /(2\pi)$, $\gamma_{rn} = \psi_n z_r /(2\pi)$, $n=1,\ldots,N/2$.

When the sun-planet and ring-planet meshes are both counter-phased (odd z_s, z_r), equation (5.36) holds for odd l because $a_{sn}^{(l)} = -a_{s(n+N/2)}^{(l)}$ and similar relations for $a_{rn}^{(l)}$, $b_{sn}^{(l)}$, $b_{rn}^{(l)}$. Recalling modal property (5.24), $D_{pq}^{(l)} = E_{pq}^{(l)} = 0$ in (5.32) for distinct ω_p, ω_q and odd l. From (5.26) and (5.27), primary and combination ($l=1$) instabilities of distinct modes *always* vanish in the counter-phased case. Physically, these instabilities are eliminated because the modal excitations from each pair of diametrically opposed planets always cancel each other. The instability regions involving degenerate modes are obtained from numerical evaluation of the eigenvalues of (5.30).

When pairs of opposing sun-planet or ring-planet meshes are in-phase (even z_s or even z_r), no simple expressions for instabilities regions are available; numerical solutions are obtained from (5.26), (5.27), (5.30), and (5.31).

5.2.4 Dynamic Response and Contact Loss

When planetary gears are operated inside an instability region, damping and nonlinearities from friction, tooth separation, *etc* bound the unstable linear model motion. Figure 5.15a shows the RMS steady-state planet response amplitude versus mesh frequency for the same system as in Figure 5.11 and the stiffness variation $\varepsilon=0.3$. Rayleigh damping $\mathbf{C}=(0.07)*\mathbf{M}+(0.07)*\mathbf{K}$ is added to system (5.2) and the force vector is $\mathbf{F}=[-2000\ 1000\ 0\ 0\ 0]^T$ *N*. The solutions are obtained from numerical integration using mesh stiffnesses in rectangular waveforms (Figure 5.15b). The degenerate modes $\omega_3=\omega_4$ only have planet motion, so they are not excited for the torques applied to the carrier and sun. The combination instability $\omega_2+\omega_5$ is sufficiently damped so that it is not apparent in Figure 5.15a and 16a. The resonance excited by the primary instability $2\omega_5$ is extremely large because tooth separation is *not* considered; the mesh stiffnesses are pre-specified functions of time (Figure 5.15b). In practice, tooth separation (clearance nonlinearity) occurs for large dynamic responses and its effects are dramatic. Figure 5.16a shows the response for the same system as in Figure 5.15a, but tooth separations is modeled. The mesh stiffness k_{sn} or k_{rn} is set to zero if the corresponding tooth deformation $\delta_{sn}<0$ or $\delta_{rn}<0$ at any step of the integration. The response amplitude of the $2\omega_5$ primary instability is *significantly* reduced from that in Figure 5.15a. Moreover, a softening jump phenomenon occurs. Sun-planet tooth separation ($k_{sp}=0$) is apparent in Figure 5.16b for $\Omega\approx 2\omega_5$. The interactions of mesh stiffness variation and clearance nonlinearity was studied by Kahraman and Blankenship (1996, 1997) for single-mesh gears. Their effects on multi-mesh planetary gears need additional investigation.

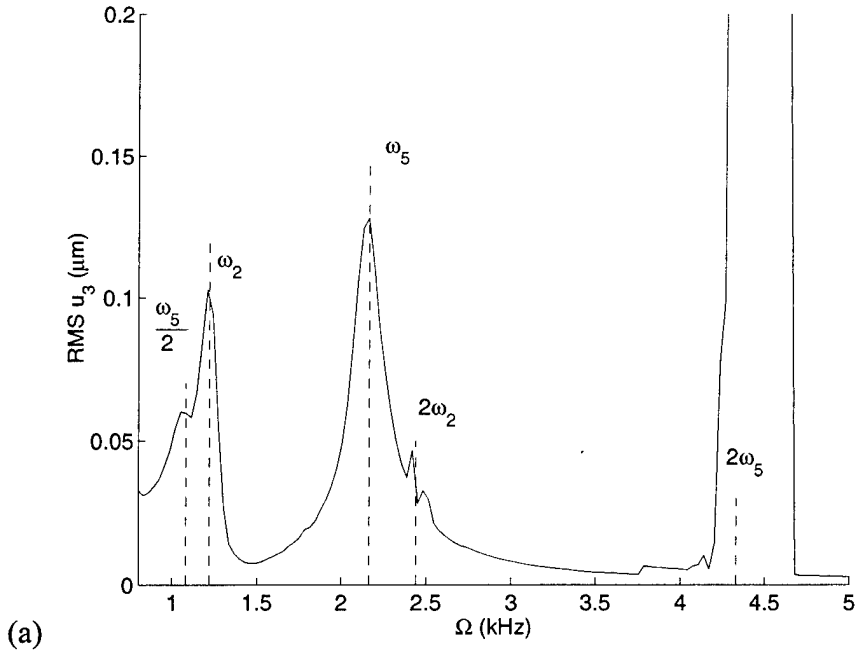

(a)

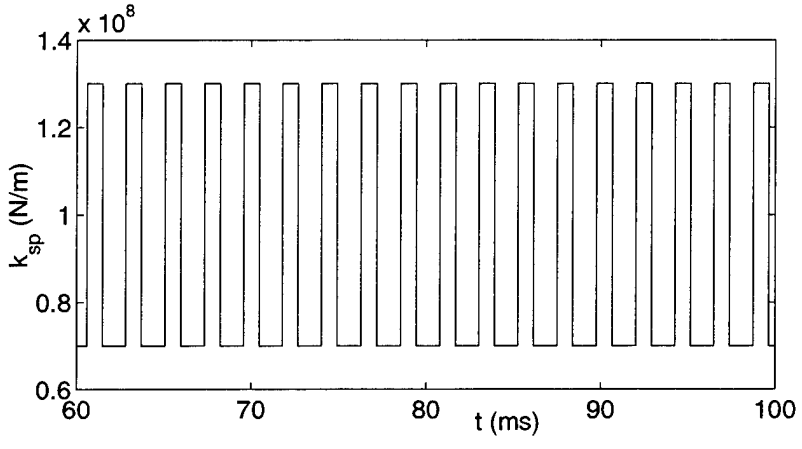

(b)

Figure 5.15 (a) Steady state RMS of dynamic planet rotation versus mesh frequency Ω when tooth separation is not considered. The parameters are as in Figure 5.11 with $\varepsilon=0.3$. (b) The sun-planet mesh stiffness is pre-specified as shown.

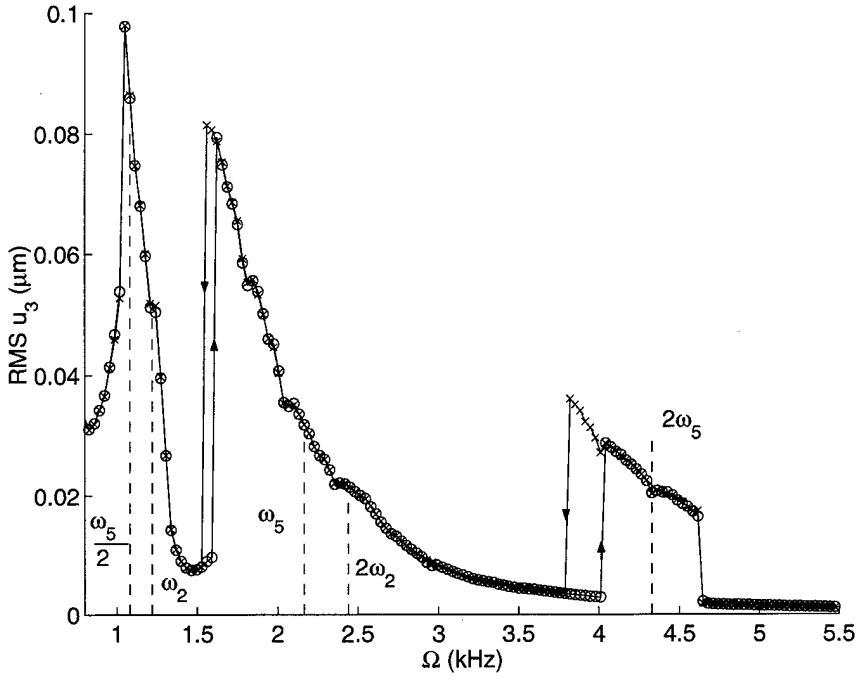

(a)

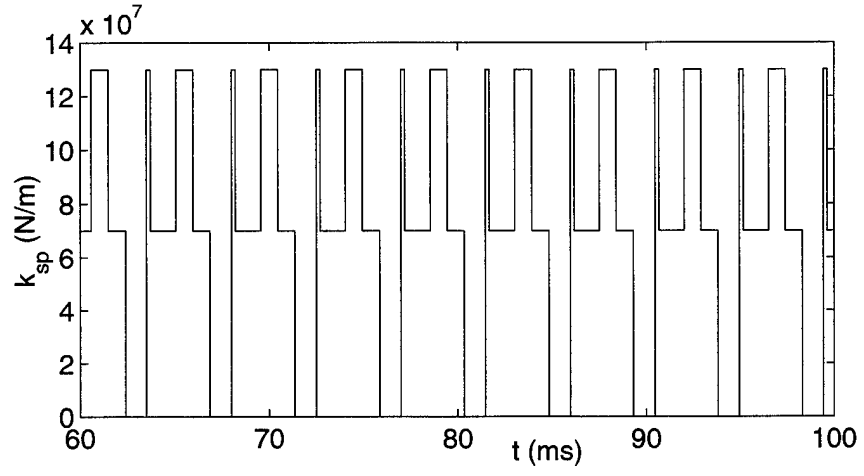

(b)

Figure 5.16 (a) Steady state RMS of dynamic planet rotation versus mesh frequency Ω when tooth separation is considered. The parameters are as in Figure 5.11 with $\varepsilon=0.3$. Circles (o) indicate increasing speed Ω and crosses (x) indicate decreasing Ω. (b) Sun-planet tooth separation ($k_{sp}=0$) occurs for $\Omega=4.5kHz\approx 2\omega_5$.

CHAPTER 6

SUMMARY AND FUTURE WORK

6.1 Summary and Benefits

This work analytically investigates several key issues in planetary gear dynamics. The main results and their benefits are summarized for each specific topic.

1. Dynamic Model of Planetary Gears

A lumped-parameter model is developed for spur planetary gears. Critical factors to gear vibration are considered, including arbitrary planet spacing and phasing, gyroscopic effects that are important in high-speed applications, mesh stiffness variation, and transmission error excitation. The model is applicable to general epicyclic gears with various configurations. It is suitable for the dynamic analysis of critical issues in planetary gear vibration and useful for design guidance (response, natural frequencies, etc.). This model is a key building block that can be expanded to couple with the housing and include multiple stages.

2. Modal Properties

This study characterizes the natural frequency spectrum and vibration mode properties in planetary gears. Planetary gears possess rich modal structure that is crucial for eigensensitivity, dynamic response, and stability analysis. Rigorous characterization of these special properties is a fundamental advance for planetary gear vibration research. These properties are capsulized as follows:

- When N planets are equally spaced, the vibration modes can be classified into six rotational modes with distinct natural frequencies, six pairs of translational modes with degenerate natural frequencies of multiplicity two, and three groups of planet modes with degenerate natural frequencies of multiplicity N-3. Each type of vibration mode has unique properties due to the cyclic symmetry of the system.
- When N/2 pairs of planets are diametrically opposed, the rotational and planet modes have the same structure as for equally spaced planets; translational modes lose their degeneracy but retain their distinct properties.
- When the planets are arbitrarily spaced, the rotational and translational modes generally lose their well-defined structure; the remarkable properties of planet modes are not affected by planet spacing.

3. Design Parameter Variations

The effects of design parameter variations on planetary gear free vibration are analytically investigated. The sensitivities of natural frequencies and vibration modes to key parameters are expressed in simple, closed-form formulae that allow one to quickly identify the parameters that most impact the modal properties. Well-defined veering rules are derived to examine the dramatic changes of vibration modes that are possible even for

small parameter variations. These results rely on the structured vibration mode properties characterized before. For design use, the results allow qualitative and quantitative assessment of the effects of design parameters on planetary gear free vibration:

- Each of the sun-planet and ring-planet mesh stiffnesses affect one rotational mode, one translational mode, and one planet mode.
- The transverse support stiffnesses and component masses of the carrier, ring, and sun only affect translational modes.
- The torsional support stiffnesses and moments of inertia of the carrier, ring, and sun only affect rotational modes.
- The planet bearing stiffness and inertia are critical parameters that affect most modes.
- The operating speed does not affect rotational and planet modes; translational mode natural frequencies at zero speed split into distinct ones as speed increases.

4. Mesh Stiffness Variation Excitation

The parametric instabilities excited by mesh stiffness variations are investigated for two-stage and planetary gear trains. The operating conditions leading to parametric instabilities are analytically determined and numerically verified. The following findings are obtained from this study.

- The contact ratios and mesh phasing strongly impact the instabilities induced by mesh stiffness variation. Simple, exact formulae derived from perturbation analyses provide design guidance to suppress particular instabilities by adjusting the contact ratios and mesh phasing.

- For two-stage gears in a countershaft configuration, the mesh excitations interact when one mesh frequency is an integer multiple of the other and dramatically change the instability conditions compared to two decoupled excitations.
- For planetary gears, the structured modal properties lead to vanishing of certain instabilities, including the combination instability of distinct and degenerate natural frequencies when planet meshes are in-phase, and the single-mode and combination instabilities of distinct natural frequencies when planet meshes are sequentially phased. Along with contact ratios, selection of planet phasing is an effective means to avoid parametric instability and its associated large response.

6.2 Future Work

To thoroughly understand planetary gear dynamics and develop reliable design tools for noise and vibration reduction, this research needs to be advanced in several challenging areas discussed below.

1. Nonlinear Effects

Tooth separation nonlinearity strongly affects the dynamic behaviors of single-mesh gears, including jump phenomena and multiple steady state solutions (Blankenship and Kahraman 1995; Kahraman, 1992; Kahraman and Blankenship, 1996, 1997; Kahraman and Singh, 1991; Parker et al., 2000b; Rook and Singh, 1995; Theodossiades and Natsiavas, 2000). Typical methodologies such as direct integration, harmonic balance, perturbation, and shooting method were used in the above analyses. This nonlinearity has not been fully investigated in planetary gears. The contact loss nonlinearity, coupled with

mesh stiffness variation, transmission error excitation, and mesh phasing, is expected to impact dynamic responses, load sharing among planets, bearing loads, tooth fatigue, and gear noise. Analytical study of nonlinear effects will provide improved design guidance for planetary gears based on dynamic response.

2. Transmission Error Modeling

For single-mesh gears, static transmission error (STE) is naturally defined and widely used as a metric for vibration and noise (Gregory et al., 1963-64; Smith, 1987; Ozguven and Houser, 1988b). The specification of transmission errors in planetary gears is complicated due to the carrier rotation and multiple meshes coupled together. Donley and Steyer (1992) simply used a "net transmission error" that is the average of all individual transmission errors of the sun-planet and ring-planet meshes. Although this simplification reduces the computational and modeling effort, it is a significant simplification difficult to interpret of the dynamic mesh forces. Other studies (Kahraman, 1994b, 1999; Kahraman and Blankenship, 1994) used Fourier series to represent STE in each mesh, but did not address the physical modeling related to profile error, pitch error, run-out error, and misalignment. It remains a question how to synthesize transmission errors from these parameters in planetary gears. More investigations are needed to define, calculate, and measure a useful analog of STE in planetary gears.

3. Dynamic Response

Dynamic response from analytical models is useful to predict the noise and vibration early in the design stage. To reliably determine dynamic response, it requires precise representation of dynamic excitation from tooth meshes. The time-varying mesh

stiffness and transmission error for single-mesh gears can be calculated from the contact analysis program LDP (Houser, 1990) or other tools. A major challenge is to match dynamic response obtained from analytical models using these approximations as input with benchmark computational and experimental results. No such comparison exists for planetary gears, and this restricts the application of analytical models in practical design. In addition, the effects of major design factors (*e.g.*, contact ratio, mesh phasing, mesh stiffness variation, support/bearing stiffness, tooth modification) on dynamic response need be characterized for design guidance. This investigation will start with two-stage spur gears and then extend to more complicated planetary gears.

4. Ring Gear Flexibility

The ring body is considered rigid in this dissertation. In practice, internal gears with thin rims may distort elastically. Experimental measurements (Ma and Botman, 1984) and finite element computations (Kahraman and Vijayakar, 2000) have shown dramatic changes in load sharing among planets from the ring flexibility. Because the ring is usually connected to the housing, its flexibility directly influences the transmission of structure-borne noise. The elastic distortion of the ring can also affect the mesh stiffnesses and lead to contact loss. Qualitative and quantitative analyses of the effects of ring flexibility is necessary to improve understanding of physical behaviors. The fundamental task is to extend the current discrete model by including the continuous deformation of the ring body. The analytical and computational methods discussed in this work can likely be used on this extended model.

5. Experimental Verification

5. Experimental Verification

The inherent complexity of gear dynamics requires experimental validation of analytical and numerical results. For single-mesh gear models, there are extensive experiments verifying analytical findings as well as presenting questions for research and design. The analytical models of planetary gears, however, have not been properly validated because of the lack of benchmark experimentation. The calculated vibrations from the finite element tool Calyx agree well with measured results at NASA Glenn Research Center (Krantz, 1992) and General Motors (Blankenship and Kahraman, 1996; Kahraman and Blankenship, 1997, 1999a, b; Parker et al., 2000b). More experimental studies are needed to develop reliable dynamic models suitable for practical design and investigate critical issues in planetary gear vibration.

APPENDIX A: SYSTEM MATRICES

$$\mathbf{M} = diag(\mathbf{M}_c, \mathbf{M}_r, \mathbf{M}_s, \mathbf{M}_1, \cdots, \mathbf{M}_N)$$

$$\mathbf{M}_h = diag(m_h, m_h, I_h / r_h^2), \quad h = c, r, s, 1, \cdots, N$$

$$\mathbf{G} = \begin{bmatrix} 0 & -2m_h & 0 \\ 2m_h & 0 & 0 \\ 0 & 0 & 0 \end{bmatrix}$$

$$\mathbf{K}_\Omega = diag(m_c, m_c, 0, m_r, m_r, 0, m_s, m_s, 0, m_p, m_p, 0, \cdots, m_p, m_p, 0)$$

$$\mathbf{K}_b = diag(\mathbf{K}_{cb}, \mathbf{K}_{rb}, \mathbf{K}_{sb}, \mathbf{0}, \cdots, \mathbf{0})$$

$$\mathbf{K}_{hb} = diag(k_{hx}, k_{hy}, k_{hu}), \quad h = c, r, s$$

$$\mathbf{K}_m = \begin{bmatrix} \sum \mathbf{K}_{c1}^n & \mathbf{0} & \mathbf{0} & \mathbf{K}_{c2}^1 & \mathbf{K}_{c2}^2 & \cdots & \mathbf{K}_{c2}^N \\ & \sum \mathbf{K}_{c1}^n & \mathbf{0} & \mathbf{K}_{r2}^1 & \mathbf{K}_{r2}^2 & \cdots & \mathbf{K}_{r2}^N \\ & & \sum \mathbf{K}_{s1}^n & \mathbf{K}_{s2}^1 & \mathbf{K}_{s2}^2 & \cdots & \mathbf{K}_{s2}^N \\ & & & \mathbf{K}_{pp}^1 & \mathbf{0} & \cdots & \mathbf{0} \\ & \text{symmetric} & & & \ddots & & \vdots \\ & & & & & & \mathbf{K}_{pp}^N \end{bmatrix}$$

$$\mathbf{K}_{c1}^n = \begin{bmatrix} 1 & 0 & -\sin\psi_n \\ & 1 & \cos\psi_n \\ \text{symmetric} & & 1 \end{bmatrix} \qquad \mathbf{K}_{c2}^n = \begin{bmatrix} -\cos\psi_n & \sin\psi_n & 0 \\ -\sin\psi_n & -\cos\psi_n & 0 \\ 0 & -1 & 0 \end{bmatrix}$$

$$\mathbf{K}_{c3}^n = diag(k_{pn}, k_{pn}, 0)$$

$$\mathbf{K}_{r1}^{n} = k_{sn}(t)\begin{bmatrix} \sin^2\psi_{rn} & -\cos\psi_{rn}\sin\psi_{rn} & -\sin\psi_{rn} \\ & \cos^2\psi_{rn} & \cos\psi_{rn} \\ \text{symmetric} & & 1 \end{bmatrix}$$

$$\mathbf{K}_{r2}^{n} = k_{rn}(t)\begin{bmatrix} -\sin\psi_{rn}\sin\alpha_r & -\sin\psi_{rn}\cos\alpha_r & \sin\psi_{rn} \\ \cos\psi_{rn}\sin\alpha_r & -\cos\psi_{rn}\cos\alpha_r & -\cos\psi_{rn} \\ \sin\alpha_r & -\cos\alpha_r & 1 \end{bmatrix}$$

$$\mathbf{K}_{r3}^{n} = k_{rn}(t)\begin{bmatrix} \sin^2\alpha_r & -\cos\alpha_r\sin\alpha_r & -\sin\alpha_r \\ & \cos^2\alpha_r & \cos\alpha_r \\ \text{symmetric} & & 1 \end{bmatrix}$$

$$\mathbf{K}_{s1}^{n} = k_{sn}(t)\begin{bmatrix} \sin^2\psi_{rn} & -\cos\psi_{sn}\sin\psi_{sn} & -\sin\psi_{sn} \\ & \cos^2\psi_{sn} & \cos\psi_{sn} \\ \text{symmetric} & & 1 \end{bmatrix}$$

$$\mathbf{K}_{s2}^{n} = k_{sn}(t)\begin{bmatrix} \sin\psi_{sn}\sin\alpha_s & \sin\psi_{sn}\cos\alpha_s & -\sin\psi_{sn} \\ -\cos\psi_{sn}\sin\alpha_s & -\cos\psi_{sn}\cos\alpha_s & \cos\psi_{sn} \\ -\sin\alpha_s & -\cos\alpha_s & 1 \end{bmatrix}$$

$$\mathbf{K}_{s3}^{n} = k_{sn}(t)\begin{bmatrix} \sin^2\alpha_s & \cos\alpha_s\sin\alpha_s & -\sin\alpha_s \\ & \cos^2\alpha_s & -\cos\alpha_s \\ \text{symmetric} & & 1 \end{bmatrix}$$

$$\mathbf{T}(t) = [0,0,T_c,0,0,T_r,0,0,T_r,0,\cdots 0]^T$$

$$\mathbf{F}(t) = [\mathbf{0},\mathbf{F}_r,\mathbf{F}_s,\mathbf{F}_1\cdots\mathbf{F}_N]^T,$$

$$\mathbf{F}_r = k_{rn}e_{rn}[\sin\psi_{rn},-\cos\psi_{rn},1]^T,$$

$$\mathbf{F}_s = k_{sn}e_{sn}[\sin\psi_{sn},-\cos\psi_{sn},1]^T$$

$$\mathbf{F}_n = k_{rn}e_{rn}[\sin\alpha_r,-\sin\alpha_r,-1]^T + k_{sn}e_{sn}[\sin\alpha_s,-\sin\alpha_r,1]^T$$

Note that the mesh stiffness variation is modeled by the time-varying stiffnesses $k_{sn}(t)$ and $k_{rn}(t)$.

APPENDIX B: EXAMPLE SYSTEM

The planetary gear used in the U.S. Army's Helicopter OH-58 is the benchmark example in the work. Two cases of the system are used in the study.

Case I: The ring gear is free and the system has $3(N+3)$ degree of freedom, where N is the number of planets. The model parameters are given in Table C.1.

Case II: The ring gear is fixed ($k_r = k_{ru} = 0$) and other parameters are the same as Table C.1. The system has four planets and 18 degrees of freedom.

	Sun	Ring	Carrier	Planet
Mass (kg)	0.4	2.35	5.43	0.66
I/r^2 (kg)	0.39	3.00	6.29	0.61
Base diameter (mm)	77.42	275.03	177.8	100.35
Teeth number	27	99		35
Mesh stiffness (N/m)	$k_{sp} = k_{rp} = k_m = 5\times10^8$			
Bearing stiffness (N/m)	$k_p = k_s = k_r = k_c = 10^8$			
Torsional stiffness (N/m)	$k_{ru} = 10^9 \quad k_{su} = k_{cu} = 0$			
Pressure angle (°)	$\alpha_s = \alpha_r = \alpha = 24.6$			

Table B.1 Model parameters of the planetary gear in the U.S. Army's helicopter OH-58

BIBLIOGRAPHY

1. Adelman, H.M. and Haftka, R.T., 1986, Sensitivity Analysis of Discrete Structural Systems, AIAA Journal, 24(5): 823-832.
2. Agashe, V., 1998, Computational Analysis of the Dynamic Response of a Planetary Gear System, Master Thesis, Ohio State University.
3. Amabili, M. and Rivola, A., 1997, Dynamic Analysis of Spur Gear Pairs: Steady-State Response and Stability of the SDOF Model with Time-Varying Meshing Damping, Mechanical Systems and Signal Processing, 11(3): 375-390.
4. Arakere, N.K. and Nataraj, C., 1999, Numerical Simulation of Nonlinear Spur Gear Dynamics, ASME Design Engineering Technical Conferences, DETC99/VIB-8110, September, Las Vegas, NV.
5. August, R., 1983, Dynamics of Planetary Gear Trains, Ph. D. Thesis, Cleveland State University.
6. August, R. and Kasuba, R., 1986, Torsional Vibrations and Dynamic Loads in a Basic Planetary Gear System, Journal of Vibration, Acoustics, Stress, and Reliability in Design, 108(3): 348-353.
7. Benton, M. and Seireg, A., 1978, Simulation of Resonances and Instability Conditions in Pinion-Gear Systems, ASME Journal of Mechanical Design, 100: 26-30.
8. Benton, M. and Seireg, A., 1980a, Application of the Ritz Averaging Method to Determining the Response of Systems with Time Varying Stiffness to Harmonic Excitation, ASME Journal of Mechanical Design, 102(2): 384-390.
9. Benton, M. and Seireg, A., 1980b, Normal Mode Uncoupling of Systems with Time Varying Stiffness, ASME Journal of Mechanical Design, 102(2): 379-383.
10. Benton, M. and Seireg, A., 1981, Factors Influencing Instability and Resonances in Geared Systems, ASME Journal of Mechanical Design, 103(2): 372-378.
11. Bernard, M.L. and Bronowicki, A.J., 1994, Modal Expansion Method for Eigensensitivity with Repeated Roots, AIAA Journal, 32(7): 1500-1506.
12. Blankenship, G.W. and Kahraman, A., 1995, Steady State Forced Response of a Mechanical Oscillator with Combined Parametric Excitation and Clearance Type Non-Linearity, Journal of Sound and Vibration, 185(5): 743-765.
13. Blankenship, G.W. and Kahraman, A., 1996, Gear Dynamics Experiments, Part I: Characterization of Forced Response, Proceedings of the 1996 Power Transmission and Gearing Conference, 373-380.

14. Blankenship, G.W. and Singh, R., 1995, Analytical Solution for Modulation Side-Band Associated with a Class of Mechanical Oscillators, Journal of Sound and Vibration, 179(1): 13-36.

15. Bollinger, J.G. and Harker, R.J., 1967, Instability Potential of High Speed Gearing, Journal of the Industrial Mathematics, 17: 39-55.

16. Bolotin, V.V., 1964, The Dynamic Stability of Elastic Systems, Holden-Day, San Francisco.

17. Botman, M., 1976, Epicyclic Gear Vibrations, Journal of Engineering for Industry, 96: 811-815.

18. Botman, M., 1980, Vibration Measurements on Planetary Gears of Aircraft Turbine Engines, AIAA Journal, 17: 351-357.

19. Butcher, E.A. and Sinha, S.C., 1996, Hybrid Formulation for the Analysis of Time-Periodic Linear Systems Via Chebyshev Polynomials, Journal of Sound and Vibration, 195(3): 518-527.

20. Chen, P. and Ginsberg, J.H., 1992, On the Relationship between Veering of Eigenvalue Loci and Parameter Sensitivity of Eigenfunctions, Journal of Vibration and Acoustics, 114: 141-148.

21. Chiang, T. and Badgley, R.H., 1973, Reduction of Vibration and Noise Generated by Planetary Ring Gears in Helicopter Aircraft Transmission, Journal of Engineering for Industry, 93: 1149-1158.

22. Cornwell, P.J. and Bendiksen, O.O., 1992, Numerical Study of Vibration Localization in Disordered Cyclic Structures, AIAA Journal, 30(2): 473-481.

23. Courant, R. and Hilbert, D., 1989, Methods of Mathematical Physics, John Wiley & Sons, New York.

24. Cunliffe, F., Smith, J.D. and Welbourn, D.B., 1974, Dynamic Tooth Loads in Epicyclic Gears, Journal of Engineering for Industry, 94: 578-584.

25. Dailey, R.L., 1989, Eigenvector Derivatives with Repeated Eigenvalues, AIAA Journal, 27(4): 486-491.

26. Donley, M.G. and Steyer, G.C., 1992, Dynamic Analysis of a Planetary Gear System, Proc. of the 1992 International Power Transmission and Gearing Conference, 117-127.

27. Fox, R.L. and Kapoor, M.P., 1968, Rates of Change of Eigenvalues and Eigenvectors, AIAA Journal, 6: 2426-2429.

28. Frater, J.L., August, R. and Oswald, F.B., 1983, Vibration in Planetary Gear Systems with Unequal Planet Stiffnesses, NASA Technical Memorandum 83428.

29. Friswell, M.I., 1996, The Derivatives of Repeated Eigenvalues and Their Associated Eigenvectors, Journal of Vibration and Acoustics, 118: 390-397.

30. Gregory, R.W. et al., 1963-64, Dynamic Behavior of Spur Gears, Proceedings of Institute of Mechanical Engineers, 178(8): 207-226.

31. Happawana, G.S., Bajaj, A.K. and Nwokah, O.D.I., 1991, Singular Perturbation Perspective on Mode Localization, Journal of Sound and Vibration, 147(2): 361-365.

32. Happawana, G.S., Bajaj, A.K. and Nwokah, O.D.I., 1993, Singular Perturbation Analysis of Eigenvalue Veering and Modal Sensitivity in Perturbed Linear Periodic Systems, Journal of Sound and Vibration, 160(2): 225-242.

33. Happawana, G.S., Nwokah, O.D.I., Bajaj, A.K. and Azene, M., 1998, Free and Forced Response of Mistuned Linear Cyclic Systems: A Singular Perturbation Approach, Journal of Sound and Vibration, 211: 761-789.

34. Heath, G. and Bossler, R., 1993, Advanced Rotorcraft Transmission (Art) Program-Final Report, NASA CR-191057, ARL-CR 14.

35. Hidaka, T., Terauchi, Y. and Nagamura, K., 1976a, Dynamic Behavior of Planetary Gears - 1st Report: Load Distribution, Bull. JSME, 19(132): 690-698.

36. Hidaka, T., Terauchi, Y. and Ishioka, K., 1976b, Dynamic Behavior of Planetary Gear -2nd Report, Displacement of Sun Gear and Ring Gear, Bulletin of the JSME, 19(138): 1563-1570.

37. Hidaka, T., et al., 1977, Dynamic Behavior of Planetary Gear-3rd Report, Displacement of Ring Gear in Direction of Line of Action, Bulletin of the JSME, 20: 1663-1672.

38. Hidaka, T., Terauchi, Y. and Ishioka, K., 1979a, Dynamic Behavior of Planetary Gear-4th Report, Influence of the Transmitted Tooth Load on the Dynamic Increment Load, Bulletin of the JSME, 22(168): 877-884.

39. Hidaka, T., Terauchi, Y. and Nagamura, K., 1979b, Dynamic Behavior of Planetary Gear - 5th Report, Dynamic Increment of Torque, Bulletin of the JSME, 22(169): 1017-1025.

40. Hidaka, T., Terauchi, Y. and Nagamura, K., 1979c, Dynamic Behavior of Planetary Gear - 6th Report, Influence of Meshing-Phase, Bulletin of the JSME, 22(169): 1026-1033.

41. Hidaka, T., Terauchi, Y. and Nagamura, K., 1979d, Dynamic Behavior of Planetary Gear - 7th Report, Influence of the Thickness of the Ring Gear, Bulletin of the JSME, 22(170): 1142-1149.

42. Hidaka, T., Terauchi, Y. and Dohi, K., 1979e, On the Relation between the Run-out Errors and the Motion of the Center of Sun Gear in a Stoeckicht Planetary Gear, Bulletin of the JSME, 22(167): 748-754.

43. Hidaka, T., Terauchi, Y. and Fujii, M., 1980, Analysis of Dynamic Tooth Load on Planetary Gear, Bulletin of the JSME, 23(176): 315-323.

44. Hidaka, T., Sugimoto, N. and Ishida, T., 1986, Effects of Errors of Elements on Load Distribution in Planetary Gears with Various Load Equalizing Mechanisms, 52(480): 2200-2206.

45. Hidaka, T., Ishida, T., Wang, K.-j. and Emoto, M., 1993, Vibration of Solar-Type Planetary Gears, Transactions of the Japan Society of Mechanical Engineers, Part C, 59(567): 3548-3554.

46. Houser, D. R., 1990, Gear Noise Sources and Their Prediction Using Mathematical Models, Gear Design Manufacturing and Inspection Manual, Chapter 16, SAE.

47. Hsu, C.S., 1963, On the Parametric Excitation of a Dynamic System Having Multiple Degrees of Freedom, Journal of Applied Mechanics, 30: 367-372.

48. Hsu, C.S., 1965, Further Results on Parametric Excitation of a Dynamic System, Journal of Applied Mechanics, 32: 373-377.

49. Hsu, C.S. and Cheng, W.H., 1974, Steady-State Response of a Dynamical System under Combined Parametric and Forcing Excitations, Journal of Applied Mechanics, 41: 371-378.

50. Ibrahim, R.A. and Barr, A.D.S., 1978, Parametric Vibration Part-I: Mechanics of Linear Problems, Shock and Vibration Digest, 10: 15-29.

51. Kahraman, A., 1992, On the Response of a Preloaded Mechanical Oscillator With a Clearance: Period-Doubling and Chaos, Nonlinear Dynamics, 3: 183-198.

52. Kahraman, A., 1994a, Load Sharing Characteristics of Planetary Transmissions, Mechanism and Machine Theory, 29: 1151-1165.

53. Kahraman, A., 1994b, Planetary Gear Train Dynamics, ASME Journal of Mechanical Design, 116(3): 713-720.

54. Kahraman, A., 1994c, Natural Modes of Planetary Gear Trains, Journal of Sound and Vibration, 173(1): 125-130.

55. Kahraman, A., 1994d, Dynamic Analysis of a Multi-Mesh Helical Gear Train, ASME Journal of Mechanical Design, 116(3): 706-712.

56. Kahraman, A., 1999, Static Load Sharing Characteristics of Transmission Planetary Gear Sets: Model and Experiment, Transmission and Driveline Systems Symposium, SAE paper 1999-01-1050.

57. Kahraman, A. and Blankenship, G.W., 1994, Planet Mesh Phasing in Epicyclic Gear Sets, Proc. of International Gearing Conference, Newcastle, UK, 99-104.

58. Kahraman, A. and Blankenship, G.W., 1996, Interactions between Commensurate Parametric and Forcing Excitations in a System with Clearance, Journal of Sound and Vibration, 194(3): 317-336.

59. Kahraman, A. and Blankenship, G.W., 1997, Experiments on Nonlinear Dynamic Behavior of an Oscillator with Clearance and Periodically Time-Varying Parameters, Journal of Applied Mechanics, 64: 217-226.

60. Kahraman, A. and Blankenship, G.W., 1999a, Effect of Involute Contact Ratio on Spur Gear Dynamics, ASME Journal of Mechanical Design, 121(1): 112-118.

61. Kahraman, A. and Blankenship, G.W., 1999b, Effect of Involute Tip Relief on Dynamic Response of Spur Gear Pairs, ASME Journal of Mechanical Design, 121(2): 313-315.

62. Kahraman, A. and Singh, R., 1991, Nonlinear Dynamics of a Geared Rotor-Bearing System with Multiple Clearances, Journal of Sound and Vibration, 144(3): 469-506.

63. Kahraman, A. and Vijayakar, S.M., 2000, Effect of Internal Flexibility on the Quasi-Static Behavior of a Planetary Gear Set, ASME Design Engineering Technical Conferences, Paper No. DETC2000/PTG-14364, September, Baltimore, MD.

64. Kasuba, R. and August, R., 1984, Gear Mesh Stiffness and Load Sharing in Planetary Gearing, ASME 4th Power Transmission Conference, ASME Paper 84-DET-229, Cambridge, MA.

65. Kasuba, R. and Evans, J.W., 1981, An Extended Model for Determining Dynamic Loads in Spur Gearing, ASME Journal of Mechanical Design, 103: 398-409.

66. Krantz, T.L., 1992, Gear Tooth Stress Measurements of Two Helicopter Planetary Stages, NASA Technical Memorandum 105651.

67. Krantz, T. L., 1993, Mechanical Systems Technology Branch Research Summary, 1985-1992, NASA Technical Memorandum 106329.

68. Kryloff, N. and Bogoliuboff, N., 1947, Introduction to Non-Linear Mechanics, Princeton university press, Princeton.

69. Leissa, A.W., 1974, On a Curve Veering Aberration, Journal of Applied Mathematics and Physics, 25: 99-112.

70. Lim, T.C. and Li, J., 1999, Dynamic Analysis of Multi-Mesh Counter-Shaft Transmission, Journal of Sound and Vibration, 219: 905-919.

71. Lin, H.H., Townsend, D.P. and Oswald, F.B., 1993, Prediction of Gear Dynamics Using Fast Fourier-Transform of Static Transmission Error, Mechanics Of Structures And Machines, 21(2): 237-260.

72. Lin, J. and Parker, R.G., 1999a, Analytical Characterization of the Unique Properties of Planetary Gear Free Vibration, Journal of Vibration and Acoustics, 121: 316-321.

73. Lin, J. and Parker, R.G., 1999b, Sensitivity of Planetary Gear Natural Frequencies and Vibration Modes to Model Parameters, Journal of Sound and Vibration, 228(1): 109-128.

74. Lin, J. and Parker, R.G., 2000a, Structured Vibration Characteristics of Planetary Gears with Unequally Spaced Planets, Journal of Sound and Vibration, 233(5): 921-928.

75. Lin, J. and Parker, R.G., 2000b, Natural Frequency Veering in Planetary Gears under Design Parameter Variations, Mechanics of Structures and Machines, submitted.

76. Lin, J. and Parker, R.G., 2000c, Mesh Stiffness Variation Instabilities in Two-Stage Gear Systems, Journal of Vibration and Acoustics, submitted.

77. Lin, J. and Parker, R.G., 2000d, Parametric Instabilities in Planetary Gears under Mesh Stiffness Variations, Journal of Vibration and Acoustics, in preparation.

78. Lindh, K. G. and Likins, P. W., 1970, Infinite Determinant Methods for Stability Analysis of Periodic-Coefficient Differential Equations, AIAA Journal, 8: 680-686.

79. Liu, H.-J. and Zhao, L.-C., 1997, Mode Localization Due to Asymmetric Structural Changes, Computers and Structures, 65(1): 91-96.

80. Lynwander, P., 1983, Gear Drive Systems: Design and Application, Dekker, New York.

81. Ma, P. and Botman, M., 1984, Load Sharing in a Planetary Gear Stage in the Presence of Gear Errors and Misalignment, Journal of Mechanisms, Transmissions and Automation in Design, 104: 1-7.

82. McLachlan, N.W., 1947, Theory and Application of Mathieu Functions, Clarendon Press, Oxford.

83. Meirovitch, L., 1967, Analytical Methods in Vibration, Macmillan, New York.

84. Mills-Curran, W.C., 1988, Calculation of Eigenvector Derivatives for Structures with Repeated Eigenvalues, AIAA Journal, 26(7): 867-871.

85. Müller, H.W., 1982, Epicyclic Drive Trains: Analysis, Synthesis, and Applications, Wayne State University Press, Detroit.

86. Nataraj, C. and Arakere, N.K., 1999, Dynamic Response and Stability of a Spur Gear Pair, ASME Design Engineering Technical Conferences, DETC99/VIB-8110, Las Vegas, NV.

87. Nataraj, C. and Whitman, A.M., 1997, Parameter Excitation Effects in Gear Dynamics, ASME Design Engineering Technical Conferences, DETC97/VIB-4018, Sacramento, CA.

88. Nayfeh, A.H., 1973, Perturbation Methods, John Wiley & Sons, New York.

89. Nayfeh, A.H. and Mook, D.T., 1979, Nonlinear Oscillations, Wiley-Interscience.

90. Noah, S.T. and Hopkins, G.R., 1982, Generalized Hill's Method for the Stability Analysis of Parametrically Excited Dynamic Systems, ASME Journal of Applied Mechanics, 49(1): 217-223.

91. Ozguven, H.N. and Houser, D.R., 1988a, Dynamic Analysis of High-Speed Gears by Using Loaded Static Transmission Error, Journal of Sound and Vibration, 125(1): 71-83.

92. Ozguven, H.N. and Houser, D.R., 1988b, Mathematical-Models Used in Gear Dynamics - a Review, Journal of Sound and Vibration, 121(3): 383-411.

93. Parker, R.G., 2000, A Physical Explanation for the Effectiveness of Planet Phasing to Suppress Planetary Gear Vibration, Journal of Sound and Vibration, 236(4): 561-573.

94. Parker, R.G., Agashe, V. and Vijayakar, S.M., 2000a, Dynamic Response of a Planetary Gear System Using a Finite Element/Contact Mechanics Model, ASME Journal of Mechanical Design, 122(3): 305-311.

95. Parker, R.G., Vijayakar, S.M. and Imajo, T., 2000b, Nonlinear Dynamic Response of a Spur Gear Pair: Modeling and Experimental Comparisons, Journal of Sound and Vibration, 236(4):561-573.

96. Perkins, N.C. and Mote, C.D., Jr., 1986, Comments on Curve Veering in Eigenvalue Problems, Journal of Sound Vibration, 106: 451-463.

97. Pierre, C., 1988, Mode Localization and Eigenvalue Loci Veering Phenomena in Disordered Structures, Journal of Sound Vibration, 126(3): 485-502.

98. Pierre, C. and Murthy, D.V., 1992, Aeroelastic Modal Characteristics of Mistuned Blade Assemblies: Mode Localization and Loss of Eigenstructure, AIAA Journal, 30: 2483-2496.

99. Pintz, A. and Kasuba, R., 1985, Dynamic Load Factors in Internal Spur Gear Drives, Journal of Mechanisms, Transmissions, and Automation in Design, 107: 424-429.

100. Raclot, J. P. and Velex, P., 1999, Simulation of the Dynamic Behavior of Single and Multi-stage Geared Systems with Shape Deviations and Mounting Errors by Using a Spectral Method, Journal of Sound and Vibration, 220: 861-903.

101. Rakhit, A.K., 1997, Improved Epicyclic Gearbox for Reduced and Controllable Subsynchronous Vibrations in Gas Turbogenerator Applications, Journal of Engineering for Gas Turbines and Power, 119(3): 640-646.

102. Ramamurti, V. and Seshu, P., 1990, On the Principle of Cyclic Symmetry in Machine Dynamics, Communications in Applied Numerical Methods, 6(4): 259-268.

103. Rook, T.E. and Singh, R., 1995, Dynamic Analysis of a Reverse-Idler Gear Pair with Concurrent Clearances, Journal of Sound Vibration, 182(2): 303-322.

104. Saada, A. and Velex, P., 1995, An Extended Model for the Analysis of the Dynamics of Planetary Trains, ASME Journal of Mechanical Design, 117: 241-247.

105. Seager, D.L., 1975, Conditions for the Neutralization of Excitation by the Teeth in Epicyclic Gearing, Journal of Mechanical Engineering Science, 17: 293-298.

106. Sinha, S.C., Pandiyan, R. and Bibb, J.S., 1996, Liapunov-Floquet Transformation: Computation and Applications to Periodic Systems, Journal of Vibration and Acoustics, 118: 209-219.

107. Sinha, S.C. and Wu, D.-H., 1991, Efficient Computational Scheme for the Analysis of Periodic Systems, Journal of Sound and Vibration, 151(1): 91-117.

108. Smith, J.D., 1983, Gears and Their Vibration: A Basic Approach to Understanding Gear Noise, Macmillan Press, New York.

109. Smith, R.E., 1987, The Relationship of Measured Gear Noise to Measured Gear Transmission Errors, AGMA 87FTM6, Cincinnati.

110. Struble, R.A., 1962, Nonlinear Differential Equations, McGraw-Hill, New York.

111. Theodossiades, S. and Natsiavas, S., 2000, Non-Linear Dynamics of Gear-Pair Systems with Periodic Stiffness and Backlash, Journal of Sound and Vibration, 229(2): 287-310.

112. Toda, A. and Botman, M., 1979. Planet Indexing in Planetary Gears for Minimum Vibration, ASME Design Engineering Technical Conference, St. Louis.

113. Tordion, G.V. and Gauvin, R., 1977, Dynamic Stability of a Two-Stage Gear Train under the Influence of Variable Meshing Stiffnesses, Journal of Engineering for Industry, 99: 785-791.

114. Velex, P. and Flamand, L., 1996, Dynamic Response of Planetary Trains to Mesh Parametric Excitations, ASME Journal of Mechanical Design, 118: 7-14.

115. Vijayakar, S.M., 1991, A Combined Surface Integral and Finite Element Solution for a Three-Dimensional Contact Problem, International Journal for Numerical Methods in Engineering, 31: 524-546.

116. Vinayak, H., Singh, R. and Padmanabhan, C., 1995, Linear Dynamic Analysis of Multi-Mesh Transmissions Containing External, Rigid Gears, Journal of Sound and Vibration, 185(1): 1-32.

117. Wei, S.-T. and Pierre, C., 1988a, Localization Phenomena in Mistuned Assemblies with Cyclic Symmetry, Part I: Free Vibrations, Journal of Vibration, Acoustics, Stress and Reliability in Design, 110(4): 429-438.

118. Wei, S.-T. and Pierre, C., 1988b, Localization Phenomena in Mistuned Assemblies with Cyclic Symmetry, Part II: Forced Vibrations, Journal of Vibration, Acoustics, Stress and Reliability in Design, 110(4): 439-449.

REPORT DOCUMENTATION PAGE

Form Approved
OMB No. 0704-0188

Public reporting burden for this collection of information is estimated to average 1 hour per response, including the time for reviewing instructions, searching existing data sources, gathering and maintaining the data needed, and completing and reviewing the collection of information. Send comments regarding this burden estimate or any other aspect of this collection of information, including suggestions for reducing this burden, to Washington Headquarters Services, Directorate for Information Operations and Reports, 1215 Jefferson Davis Highway, Suite 1204, Arlington, VA 22202-4302, and to the Office of Management and Budget, Paperwork Reduction Project (0704-0188), Washington, DC 20503.

1. AGENCY USE ONLY (*Leave blank*)	2. REPORT DATE	3. REPORT TYPE AND DATES COVERED
	May 2001	Final Contractor Report

4. TITLE AND SUBTITLE

Modeling, Modal Properties, and Mesh Stiffness Variation Instabilities of Planetary Gears

5. FUNDING NUMBERS

WU–712–20–13–00
NAG3–1979
1L161102AH45

6. AUTHOR(S)

Robert G. Parker and Jian Lin

7. PERFORMING ORGANIZATION NAME(S) AND ADDRESS(ES)

Ohio State University
Department of Mechanical Engineering
206 West 18th Avenue
Columbus, Ohio 43210–1107

8. PERFORMING ORGANIZATION REPORT NUMBER

E–12792

9. SPONSORING/MONITORING AGENCY NAME(S) AND ADDRESS(ES)

National Aeronautics and Space Administration
Washington, DC 20546–0001
and
U.S. Army Research Laboratory
Adelphi, Maryland 20783–1145

10. SPONSORING/MONITORING AGENCY REPORT NUMBER

NASA CR—2001-210939
ARL–CR–462

11. SUPPLEMENTARY NOTES

Project Manager, Timothy L. Krantz, Structures and Acoustics Division, NASA Glenn Research Center, organization code 5950, 216–433–3580.

12a. DISTRIBUTION/AVAILABILITY STATEMENT

Unclassified - Unlimited
Subject Categories: 37 and 07 Distribution: Nonstandard

Available electronically at http://gltrs.grc.nasa.gov/GLTRS

This publication is available from the NASA Center for AeroSpace Information, 301–621–0390.

12b. DISTRIBUTION CODE

13. ABSTRACT ***(Maximum 200 words)***

Planetary gear noise and vibration are primary concerns in their applications in helicopters, automobiles, aircraft engines, heavy machinery and marine vehicles. Dynamic analysis is essential to the noise and vibration reduction. This work analytically investigates some critical issues and advances the understanding of planetary gear dynamics. A lumped-parameter model is built for the dynamic analysis of general planetary gears. The unique properties of the natural frequency spectra and vibration modes are rigorously characterized. These special structures apply for general planetary gears with cyclic symmetry and, in practically important case, systems with diametrically opposed planets. The special vibration properties are useful for subsequent research. Taking advantage of the derived modal properties, the natural frequency and vibration mode sensitivities to design parameters are investigated. The key parameters include mesh stiffnesses, support/bearing stiffnesses, component masses, moments of inertia, and operating speed. The eigensensitivities are expressed in simple, closed-form formulae associated with modal strain and kinetic energies. As disorders (e.g., mesh stiffness variation, manufacturing and assembling errors) disturb the cyclic symmetry of planetary gears, their effects on the free vibration properties are quantitatively examined. Well-defined veering rules are derived to identify dramatic changes of natural frequencies and vibration modes under parameter variations. The knowledge of free vibration properties, eigensensitivities, and veering rules provide important information to effectively tune the natural frequencies and optimize structural design to minimize noise and vibration. Parametric instabilities excited by mesh stiffness variations are analytically studied for multi-mesh gear systems. The discrepancies of previous studies on parametric instability of two-stage gear chains are clarified using perturbation and numerical methods. The operating conditions causing parametric instabilities are expressed in closed-form suitable for design guidance. Using the well-defined modal properties of planetary gears, the effects of mesh parameters on parametric instability are analytically identified. Simple formulae are obtained to suppress particular instabilities by adjusting contact ratios and mesh phasing.

14. SUBJECT TERMS	15. NUMBER OF PAGES
Gear; Transmissions; Dynamic stability; Eigenvalues	123
	16. PRICE CODE

17. SECURITY CLASSIFICATION OF REPORT	18. SECURITY CLASSIFICATION OF THIS PAGE	19. SECURITY CLASSIFICATION OF ABSTRACT	20. LIMITATION OF ABSTRACT
Unclassified	Unclassified	Unclassified	